

A COMPARISON OF A HIGH-RESOLUTION SURVEY
AND A THREE-DIMENSIONAL SEISMIC SURVEY
IN A FEATURE-RICH REGION OF THE
GREEN CANYON AREA, GULF OF MEXICO

A Thesis

Submitted to the Graduate Faculty of the
Louisiana State University and
Agricultural and Mechanical College
in partial fulfillment of the
requirements for the degree of
Master of Science

in

The Department of Geology and Geophysics

by
Bruce M. Samuel
B.S., Louisiana State University, 1998
August 2004

ACKNOWLEDGMENTS

I have found the writing and organization of this thesis to be daunting, challenging, and rewarding. It certainly would not been accomplished without the help and support of my professors, associates, and family. I would like to thank Dr. Arnold Bouma for inspiring me and never giving up on me even though the chips were often down, Dr. Harry Roberts for his singular ability to portray his understanding of the Gulf of Mexico and educate, and Dr. John Wrenn for all his understanding, wisdom, and advice over the years. I am also indebted to David Moles and Judy Mooney of ENI Petroleum of Houston for providing the AUV and 3D seismic survey data and Western Geco for their permission to utilize the data. Special notice should also be given to my colleges at C & C Technologies: my supervisor Tony George for listening to my crazy ideas and reviewing my thesis, Doug Pierrottie for his keen eye and assistance with the cartography, Donny Fontenot, Heather Langill, and Brian West for their assistance with data and images, and Thomas Chance for his encouragement and vision. Last but not least I would like to thank my family: my wife Lynn for her inspiration, unerring support and good nature in allowing me the time to compose this thesis, and my son Joshua who reinvigorates my desire for the pursuit of excellence.

TABLE OF CONTENTS

ACKNOWLEDGMENTS	ii
ABSTRACT.....	v
CHAPTER 1. INTRODUCTION	1
1.1 Thesis Objective	3
CHAPTER 2. REVIEW OF LITERATURE	4
2.1 Geologic Setting.....	4
2.2 Seafloor Features Review	7
CHAPTER 3. INSTRUMENTATION AND METHODOLOGY	22
3.1 High-Resolution AUV Survey.....	22
3.2 HUGIN 3000 Autonomous Underwater Vehicle (AUV)	23
3.3 Positioning	26
3.4 Interpretation.....	27
3.5 Cartography and Data Reproduction Images	27
3.6 3D Seismic Survey Maps	28
3.7 3D Survey Specifics.....	29
3.8 Water Bottom Amplitude Extraction and Dip Maps	29
3.9 3D Seismic Profiles.....	29
CHAPTER 4. DESCRIPTION AND INTERPRETATION OF HIGH-RESOLUTION DATA SET	31
4.1 Overview Description of Seafloor Features.....	31
4.2 Overview Description and Interpretation of Subbottom Features	33
4.3 Faulting	35
4.4 Mud Volcano	38
4.5 Mud Vents.....	41
4.6 Hardground Features.....	43
4.7 Mudflows	47
4.8 Slope Instability Features.....	49
4.9 Erosional Gullies.....	50
CHAPTER 5. DESCRIPTION AND INTERPRETATION OF 3D SEISMIC DATA SET.....	54
5.1 Map Discussion.....	54
5.2 Mud Volcano	57
5.3 Mud Vents.....	59
5.4 Hardground Features.....	61
5.5 Mudflows	64
5.6 Slope Instability Features.....	65
5.7 Gullies	67

CHAPTER 6. GROUND-TRUTHING	73
6.1 Cores	73
6.1 ROV Investigation	74
CHAPTER 7. CONCLUSIONS	77
7.1 Overview Summary of Resolution.....	77
7.2 Advantages and Disadvantages.....	78
7.3 Conclusive Remarks	79
REFERENCES	81
APPENDIX A. HIGH-RESOLUTION MAPS.....	84
Sheet 1. Overview Shaded Bathymetry Map.....	85
Sheet 2. Overview Gradient Map.....	86
Sheet 3. Overview Interpretation Map.....	87
Sheet 4. Overview Side-Scan Mosaic Map.....	88
APPENDIX B. 3D SEISMIC DATA MAPS	89
Sheet 1. Water Bottom Amplitude Extraction Map.....	90
Sheet 2. Water Bottom Dip Map.....	91
APPENDIX C. GROUND-TRUTHING DATA.....	92
APPENDIX D. 3D SEISMIC SURVEY SPECIFICS.....	99
VITA	102

ABSTRACT

Recent advances in Autonomous Underwater Vehicle (AUV) technology have revolutionized the positioning and accuracy of high-resolution deep sea mapping tools. Geologic hazard and engineering surveys by AUV's are producing high-resolution data sets of a quality that has never before been seen. Three-dimensional (3D) seismic data, though traditionally used for only deep subsurface mapping of large areas, is now being reprocessed at a higher resolution and utilized in well site investigations and geologic hazard assessments. This study makes a comparison between a 3D seismic survey and an AUV high-resolution survey in order to determine the strengths and weaknesses of both of these data. The study area, located in the central eastern portion of the Green Canyon Area, Gulf of Mexico, hosts several geologic features that should be easily mapped with both media such as: major and minor faulting, a mud volcano, mud vents, mudflows, hardgrounds, slumps, and gullies. The comparison of the 3D seismic survey and the high-resolution survey will more clearly point out the strengths and weaknesses of these two types of seafloor data, which are used for geohazards assessments.

CHAPTER 1. INTRODUCTION

In today's world the ever-rising need for more and cheaper energy drives both scientific advance and a large part of the planet's economy. In the Gulf of Mexico, the need for energy has forced industry into progressively deeper water, pushing scientific advances, engineering principles, and technology to its limits. New ventures in the Gulf of Mexico are now discovering reserves 6,000 m to 9,000 m below the seafloor in water depths of 1,000 to 3,000 m below sea level. Due to the extreme depth and costs involved, remote-sensing methods have become the eyes of scientists and engineers in the search for energy.

Remote sensing, as defined by the Glossary of Geology, is "the science of collecting, processing, and interpreting images about an object or phenomenon by a recording device that is not in physical contact with the subject being studied" (Jackson, 1997). While several different remote-sensing methods are utilized in the Gulf of Mexico (i.e. gravimetrics, satellite imagery, LIDAR), two primary methods, three-dimensional (3D) seismic data and high-resolution data, are presently utilized to provide an assessment of the seafloor and the near seafloor bottom environment.

The use of 3D seismic is not new as a remote-sensing technology. The concept has been in operation since 1970, when Walton (1972) first presented the idea of a 3D survey. The first contractual utilization of a 3D survey took place in 1975 and the following year the results were presented to the world (Bone et al., 1976). The acquisition and processing of 3D seismic creates a three-dimensional, closely spaced data volume that allows for a more detailed understanding of the subsurface (Brown, 1999). Traditionally, 3D seismic has been used for subsurface mapping of reservoirs deep below the seafloor, however, as exploration moved into ultra-deep water in the

early to mid-1990's, industry began to reprocess 3D seismic data for greater resolution for use in well site investigation and geologic hazard (geohazard) assessments (Hill, 1996).

The utilization of high-resolution data grew out of a need in the 1960's (Hill, 1996) for accurate placement of pipelines, rigs, and other man-made structures on the continental shelf and avoidance of geohazards. High-resolution acoustic data, unlike 3D seismic data, is provided by the amalgamation of data from several tools rather than just one. Typical tools utilized in the acquisition of high-resolution geohazard assessment data on the continental shelf are side-scan sonar's, subbottom profilers, echo sounders, multibeam bathymetric mapping systems, airguns, and magnetometers (Trabant, 1998). As exploration moved off the shelf into deeper water, a new series of complex geohazards confronted engineers and geoscientists performing well site investigations and structure placement on the seafloor: steep slopes, unstable slopes, variable seabed sediments, bedforms, faulting, seepage, gas hydrates, and environmentally sensitive areas. In answer to industry's need for a tool capable of recording and assessing deep-sea features, the deep-tow system was born.

Deep-tow systems are composed of a large sonar fish that carries a payload of a multibeam mapping system, side-scan sonar, and a subbottom profiler. Deep-tow systems dominated the deep-water market for 15 years between the mid 1980's and the year 2000, but they have several serious flaws. Deep-tow data collection is laborious requiring extremely slow line acquisition rates (2.0 to 2.5 knots) and large line turns due to the kilometers of towing cable that are paid-out from the boat. It also requires an additional boat to provide positioning of the deep-tow below the ocean surface. All these factors made the deep-tow data acquisition a slow, inefficient, and expensive methodology (Northcutt, 2000).

In 1999 several energy companies (BP, Amoco, Shell) jointly published a paper outlining industry's requirement for a deep to ultra-deep water Autonomous Underwater Vehicle (AUV) to replace the costly and inefficient deep-tow system (Kleiner and Northcutt, 2004). In answer to industry's request, the first operational deep-water survey AUV completed sea trials and began contractual work in December of 2000. The AUV is an unmanned submersible that conducts surveys deep below sea level (presently up to 10,000 feet), running a mission plan of autonomous survey lines at a programmed depth above the seafloor for as long as 48 hours per dive. Deep-water survey AUV's carry the same payload as deep-tows (multibeam bathymetric mapping system, side-scan sonar, and subbottom profiler), however there is a notable advantage in survey time, positioning accuracy, data clarity, and cost over deep-towed systems. Today, there are three such vehicles performing deep-water high-resolution surveys around the world.

1.1 Thesis Objective

This thesis will compare two remote-sensing media: a high-resolution AUV survey and a 3D seismic survey. Each survey was conducted over the same feature-rich region of seafloor in the Green Canyon Area, Gulf of Mexico. The objective of this comparison is to evaluate the strengths and weaknesses of each system's capability to categorize features both on the seafloor and in or near the seafloor sediments. The speculative interpretations of each data set are ground-truthed in localized areas where results of both a Remote Operated Vehicle (ROV) survey and coring are available.

CHAPTER 2. REVIEW OF LITERATURE

2.1 Geologic Setting

The survey area is located in the northern Gulf of Mexico, designated as Green Canyon Area by the Minerals Management Service (MMS) (Fig. 2.1). The topography of the study area, which lies on the lower continental slope off Louisiana, is characterized by diapiric highs and basin-like topography. A bathymetric rendering (Fig. 2.2) shows the seafloor topography in the region. The hummocky nature of the study area is the result of halokinesis (salt tectonics) according to Bouma and Bryant (1994). In the Gulf of Mexico it is described as a buoyant, plastic movement of Jurassic sub-stratigraphic salt (Fig. 2.3) due to extensive late Cretaceous-Pleistocene sediment loading in depocenters on the continental shelf and continental slope (Woodbury et al., 1973).

Salt diapirs, ridges, domes, and anticlines of Mid-Jurassic age (Mann, 1987) underlie the entire Texas-Louisiana slope. Salt intrusions have dramatically influenced the regional geology of the outer shelf and slope Gulf Coast areas. Many of these mobile salt bodies nearly pierce the thick Pleistocene clastic deposits and can be found very near the seafloor. These salt bodies have uplifted, deformed, and faulted the overlying deposits and have created bathymetric highs. The uplift by halokinetic forces has also created bathymetric lows which function as mini-basins (interslope basins). Sediments displaced by uplift can cascade down the steeper slopes of the bathymetric highs in the form of slides, slumps, debris flows, and turbidity currents depositing their load in these mini-basins.

The forces resulting from gravity and overburden of Pleistocene and older deposits on the shelf and slope have caused diapiric salt of the upper slope to migrate southward. These salt bodies pond downslope, evolving into longitudinal bathymetric features called ridges, massifs, lobes, tongues and canyons of the lower slope (Lee et al., 1989). The Sigsbee Escarpment,

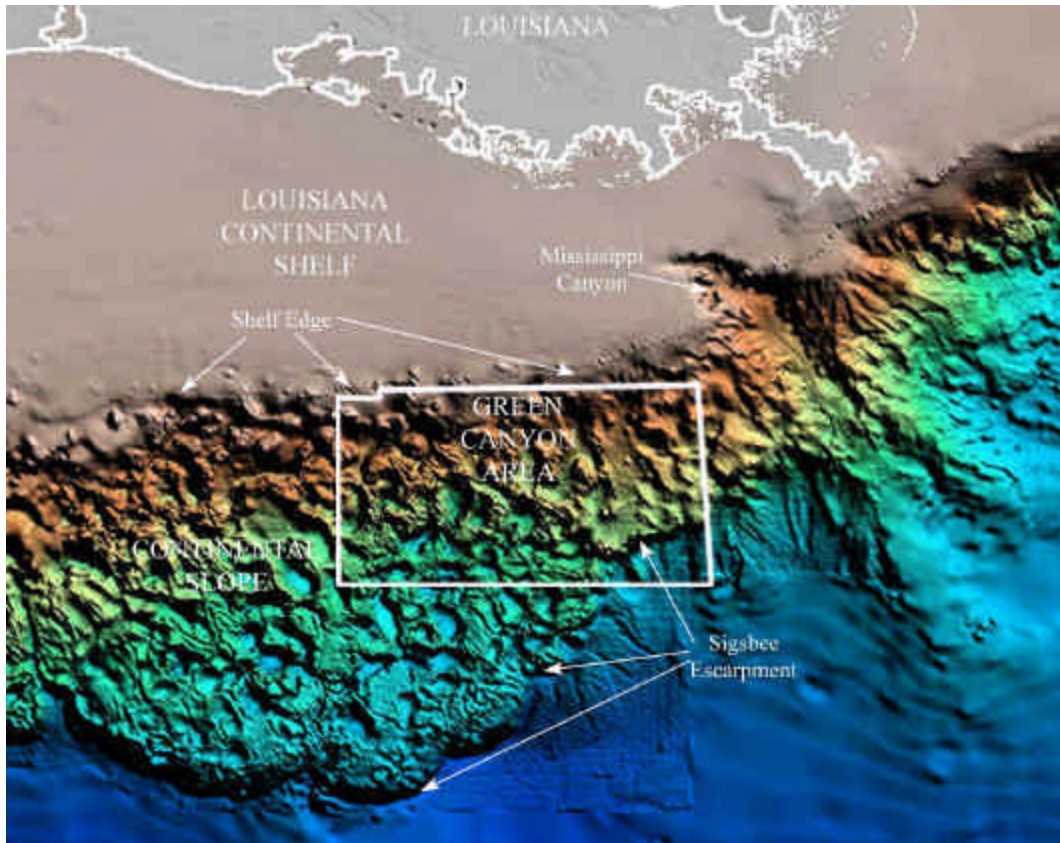


Figure 2.2. A bathymetric rendering showing the hummocky nature of the halokinetically deformed continental slope. The Green Canyon Area is identified. Bathymetric map is modified from one provided by the Texas A&M University Oceanography, deep tow research group website.

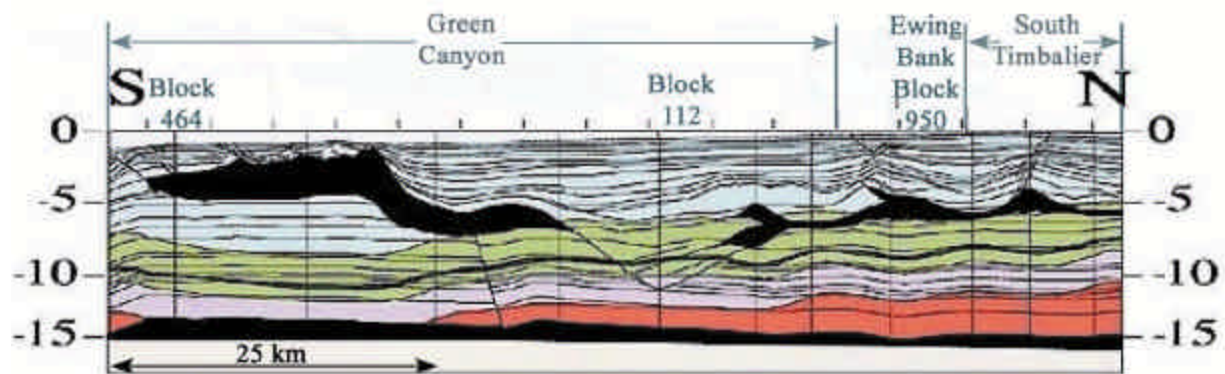


Figure 2.3. Generalized north-south cross section, through South Timbalier, Ewing Bank, and Green Canyon Areas on the continental slope offshore of Louisiana, illustrating the vertical, buoyant, plastic movement of sub-stratigraphic salt. The salt is in black and the depths are in kilometers. Modified from McBride et al., 1998.

marks the southerly lobate edge of the northern gulf halokenitic province (Coleman et al., 1991), marks the extremity of these southward mobile salt bodies in the southeastern quadrant of the Green Canyon Area (Fig. 2.2).

2.2 Seafloor Features Review

Faults of different scales, orientations, and morphologies, are the primary seafloor features that occur on the continental slope. The faults occurring on the continental slope are primarily associated with halokenitically driven uplift. Figure 2.4 shows salt diapirs that form topographic highs and their associated faults off-setting the surrounding seafloor. Uplift and faulting are responsible for a variety of seafloor features that occur on the continental slope including various forms of slope instability failures, seafloor erosion, mud vents, mud volcanoes, mudflows, mound-like structures, and hydrocarbon seepage (Coleman et al., 1991).

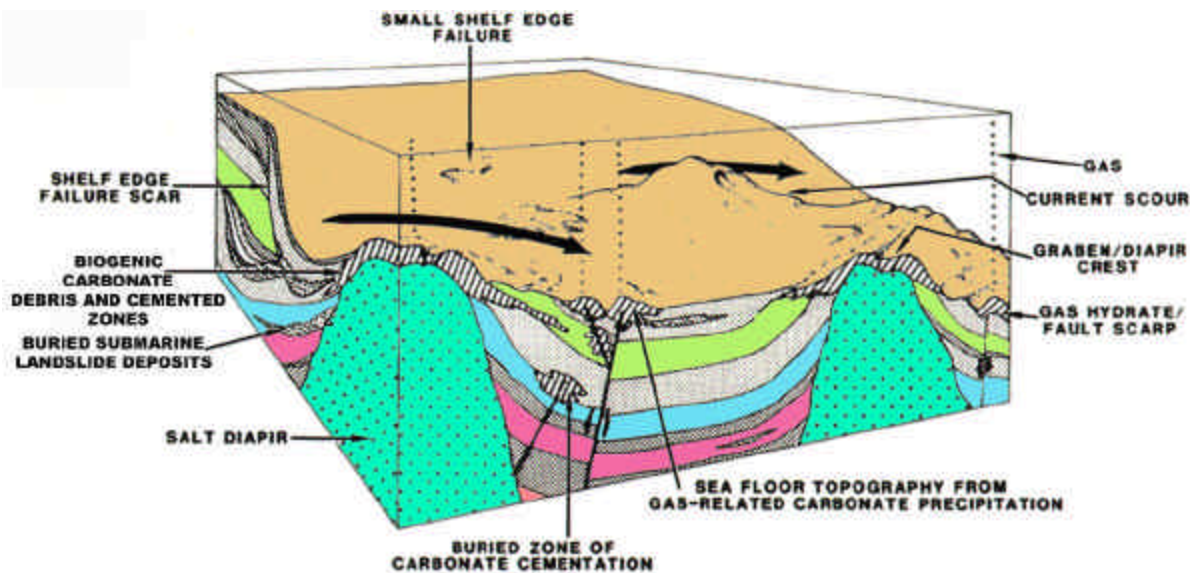


Figure 2.4. Schematic diagram illustrating the seafloor features associated with salt diapir uplift. Modified from Coleman et al., 1991.

Mass movement of sediment occurs on various scales on the continental slope. Oversteepening due to diapirism (uplift) and faulting lead to instability and the eventual failure of sediments (Fig. 2.5). Slope failure features range from small-scale (local) slides, slumps and landslides to large-scale (regional) debris flows and/or turbidites (Coleman et al., 1983).

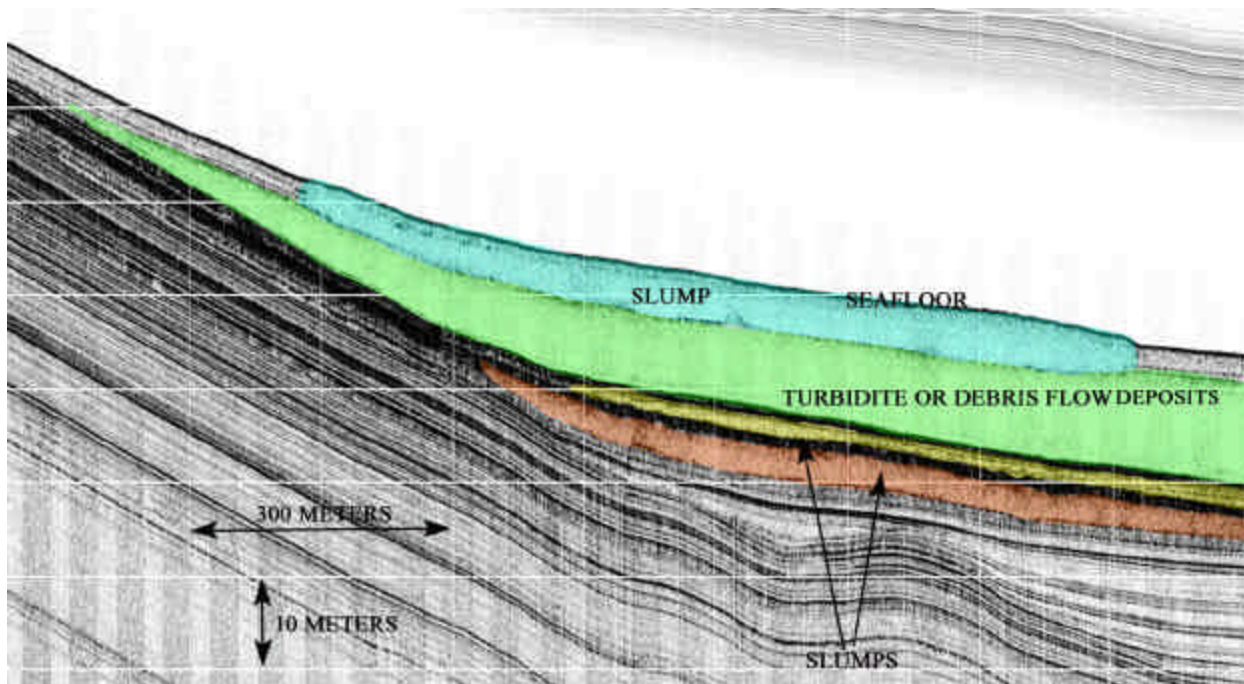


Figure 2.5. Subbottom profiler record exhibiting slope instability features in Green Canyon Area (Block 606). Two minor slumps (red and brown) are overlain by a turbidite system or debris flow deposit (green), which in turn is overlain by another slump (blue).

Seafloor erosion occurs predominantly on the uplifted crests (topographic highs) of regional diapiric or faulted features. The Loop Current and its associated westward-moving eddies are believed to be capable of moving sand-sized sediments (Hamilton, 1990). The Loop Current is a water circulation phenomenon that enters the Gulf of Mexico from the southeast, through the Yucatan Strait, loops clockwise into the central Gulf and then exits through the

Florida Strait (Fig. 2.6). Erosion due to the Loop Current and its eddies are responsible for the thinning of hemipelagic drape sediments (Fig. 2.7) or complete unconformities, seen on the crests of uplifted, faulted features in the Gulf of Mexico (Roberts, 2001).

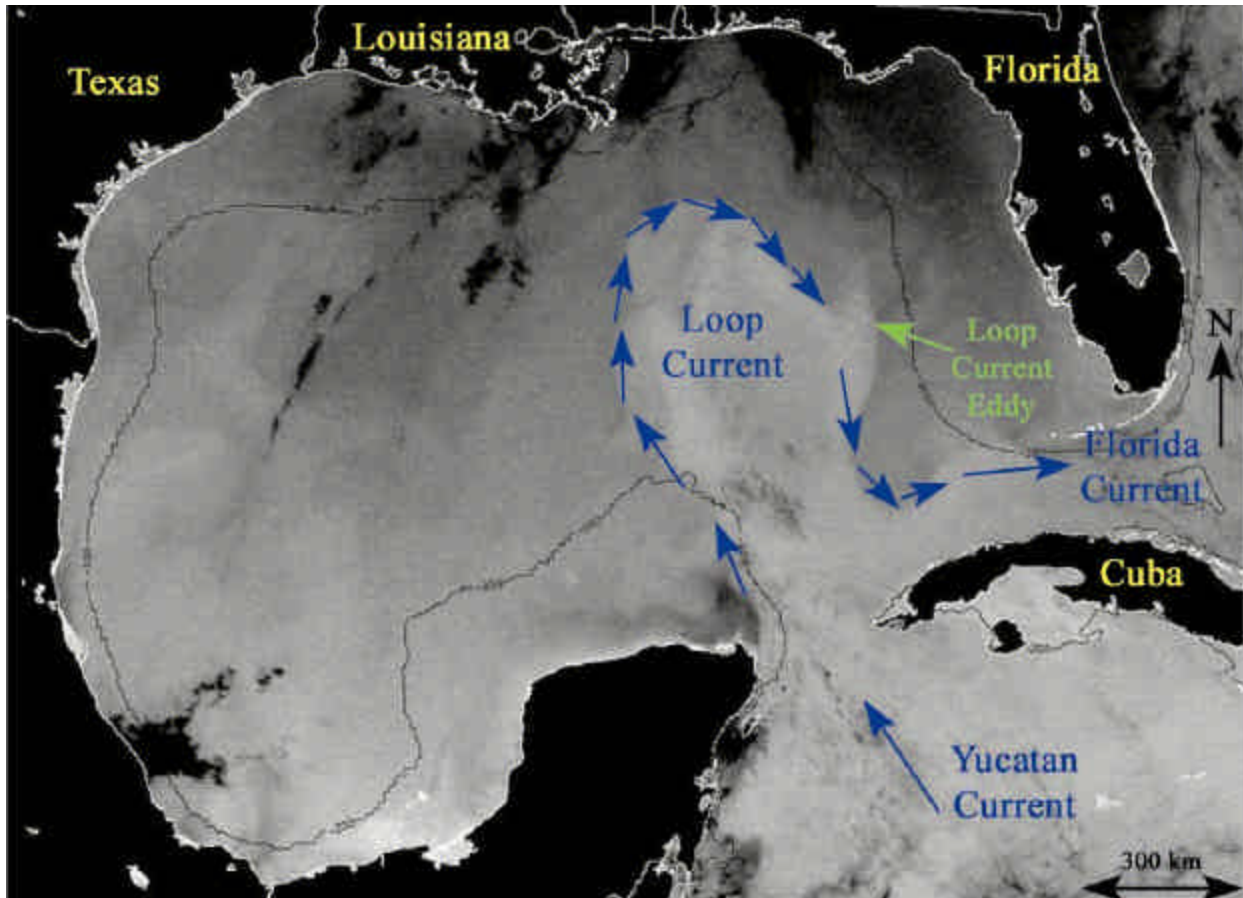


Figure 2.6. GOES-8 satellite image of the Gulf of Mexico illustrating the passage of the Loop Current. Modified from Earth Scan Lab, Louisiana State University Website (<http://antares.csi.lsu.edu/demos/goes/comploop3.gif>).

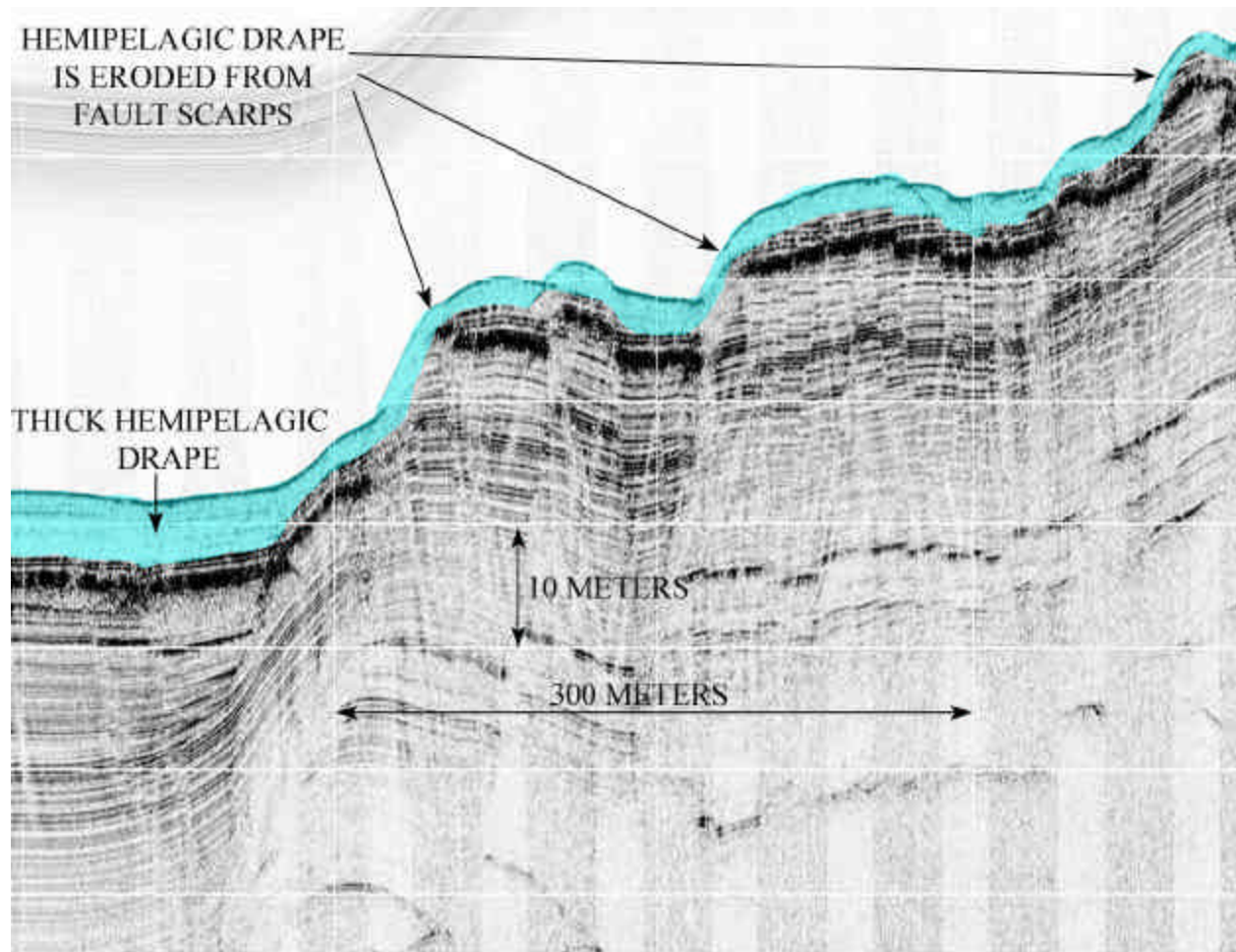


Figure 2.7. An east-west oriented subbottom profiler record exhibiting the erosion of hemipelagic drape sediments partly eroded from fault scarps in Green Canyon Area (Block 605).

Faulting, resulting from diapiric uplift, is also responsible for several types of extrusive features imaged on the seafloor. Faults create a conduit for the vertical flux and extrusion of geo-pressured fluid, fine-grained sediment, and gases to the seafloor (Fig. 2.8). Studies by Ranganathan and Hanor (1989) and Roberts and Nunn (1995) indicate that extrusion occurs as a short-lived event of perhaps 100 years duration, creating localized transient anomalies in the surficial seafloor sediments. The rate, at which extrusion occurs during this episodic event, is believed to create a variety of seafloor features (Roberts, 1998). Rapid venting (extrusion) creates mud-prone features, while slow seepage creates mineral-prone features.

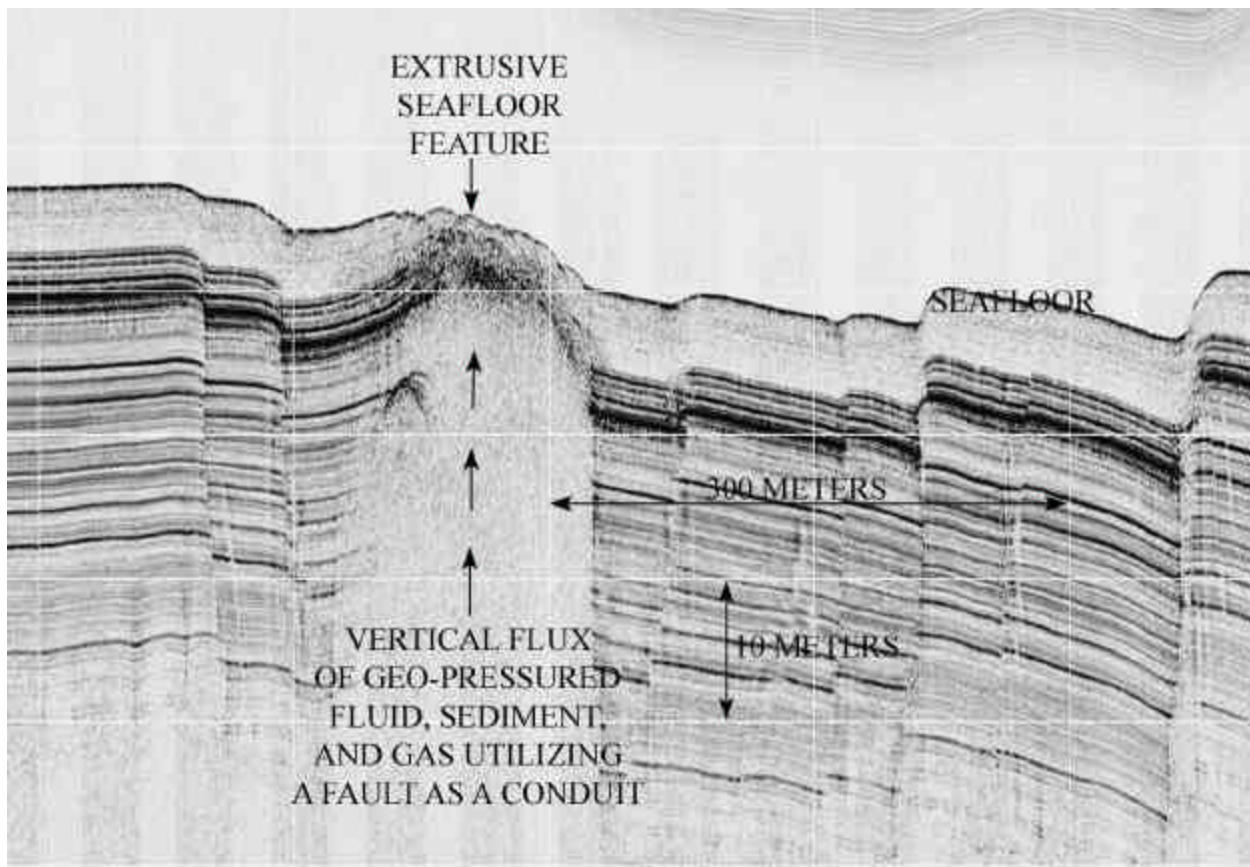


Figure 2.8. A southwest to northeast oriented subbottom profiler record showing an extrusive seafloor feature (GC 512) and the vertical flux of geo-pressured fluid, sediment, and gas utilizing a fault as a conduit, which is obscured by acoustic turbidity. Several other faults are in evidence, arrayed in a graben pattern.

A study performed for the Minerals Management Service (Roberts, 2001) seeks to coalesce these data providing a better understanding of the relationships between flux rates of hydrocarbon venting-seepage and the geological/biological variability of features recorded at extrusive sites. Figure 2.9 illustrates the relationships between mud-prone (rapid venting) and slow mineral-prone (slow seepage) extrusive environments. This study treats rapid venting and slow seepage environments as end-members and adding a moderate (transitional) flux rate in the middle. Figure 2.9 also exhibits the dominant seafloor features (geology), chemosynthetic organisms (biology), and hydrocarbon degradation (organic geochemistry) found in each of the flux rate environments.

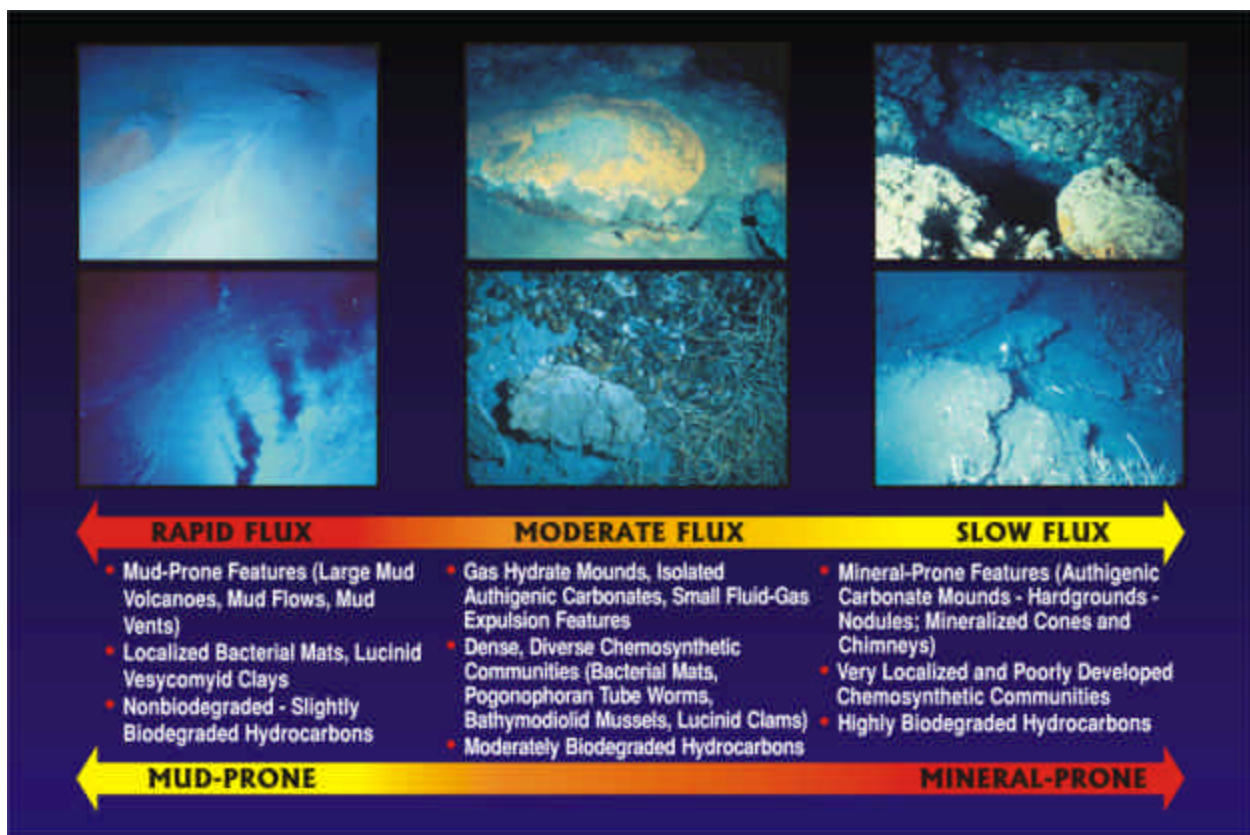


Figure 2.9. General relationships between delivery rate of fluids and gases to the seafloor and response in seafloor geology, biology, and hydrocarbon degradation. Provided by Harry H. Roberts, personal communication, 2004.

Three types of mud-prone features are associated with rapid venting: mud volcanoes, mud vents, and mudflows. These features are believed to be created by the vertical migration of gas and fluids through unconsolidated-to-semiconsolidated sediments. Migrating fluids and gas entrains sediment that results in a slurry-like mix of fine-grained sediment, gas, and water, which is then extruded to the seafloor (Hedberg, 1974). The texture of the seafloor at these sites, as seen on side-scan sonar, tends to be smooth and void of any rough topography due to the expulsion and deposition of water-rich fine-grained sediments.

Mud volcanoes are the largest of the fault-related venting features in the Gulf of Mexico, expressing 30 m or more of in height with a base of 1 km in width (Fig. 2.10). Mud vents are smaller than mud volcanoes being between 1 m and 15 m high and 2 to 50 m in width. Active mud volcanoes have a crater or caldera-like depression at their peak, which contains fluid mud and bubbling gas. Frequently, the gas-charged mud contains globules of crude oil (Neurauter and Roberts, 1992, 1994). These features grow by accretion; fluidized mud flows over the crater and down the flanks of the feature, adding a new layer of sediment to the flanks and widening the base. Inactive mud volcanoes and mud vents are easily identified because the vent orifice is draped and often completely infilled by hemipelagic sediments.

Mudflows are the extrusion of fluidized mud without the formation of a cone-shaped vent (Fig. 2.11). Mudflows are most often identified as small-scale thin-bedded sheets of muddy sediments extruded from surrounding mound-like structures (mound-like structures are discussed later in this chapter). In some cases, mudflows have been identified as thick sheets, which cascade down slopes from the point of extrusion, sometimes for kilometers (Roberts, 2001).

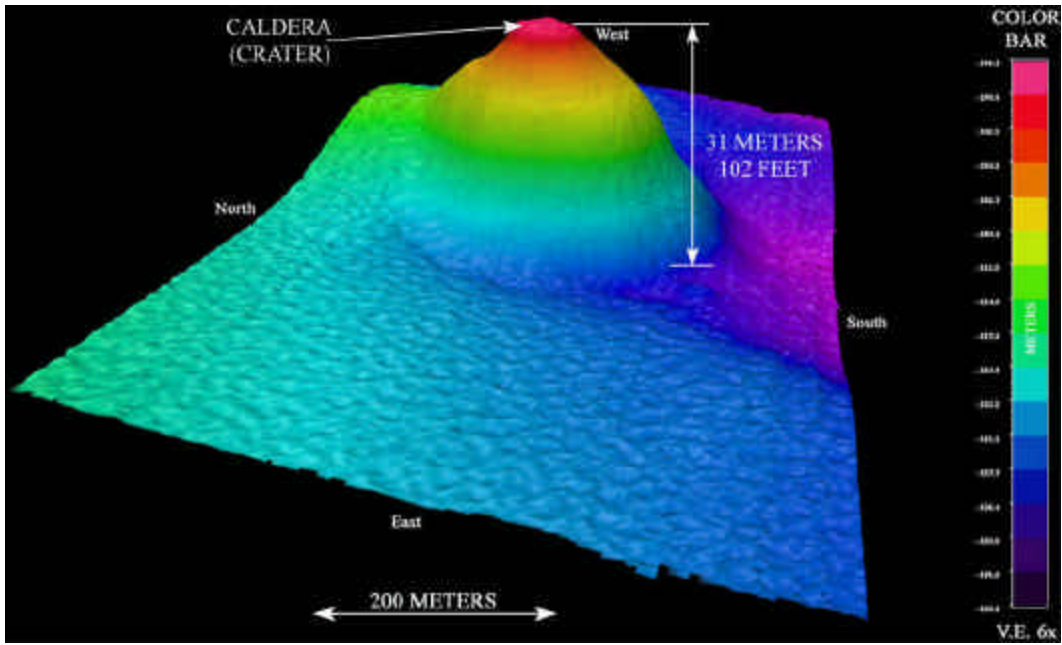


Figure 2.10. Digital terrain map of multibeam bathymetry illustrating a moderately sized active mud volcano in Block 143 Green Canyon Area. A flat circular crater appears at the crest of the feature.

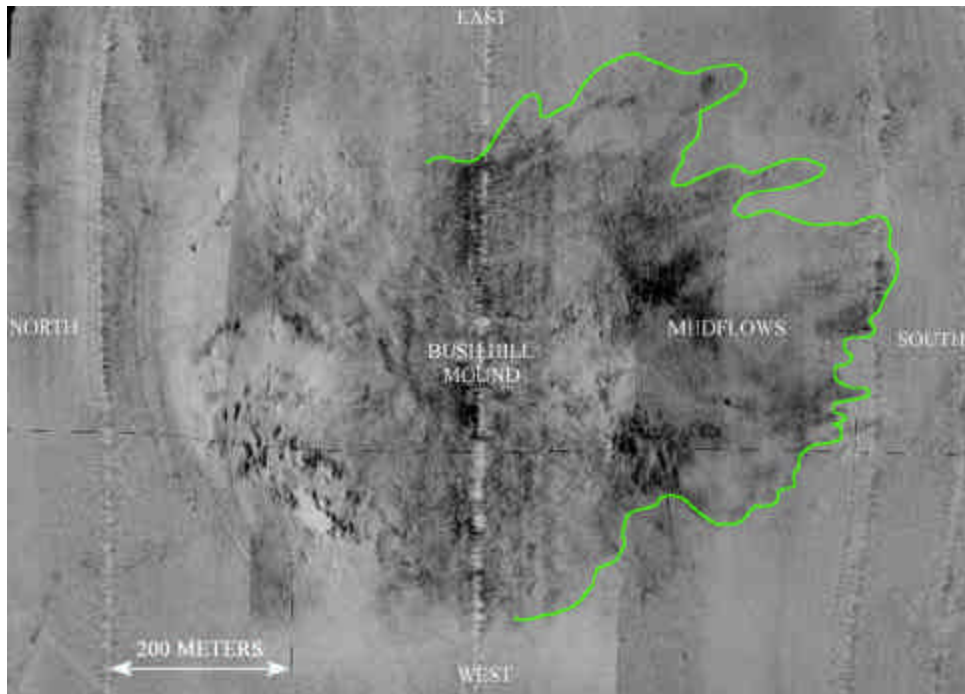


Figure 2.11. Plan view digital terrain map of mosaic side-scan sonar records over the Bush Hill mound, Green Canyon Area (Block 184), showing mudflows outlined in green on the southern mound flank.

Extrusive sites in which rapid venting of fine-grained sediment is occurring are generally free of large amounts of chemosynthetic fauna. A reduced community or lack of chemosynthetic fauna is believed to occur when vented sediments blanket the local area, thereby covering bacterial mats and stifling the respiratory organs of macroscopic chemosynthetic fauna. Four types of chemosynthetic organisms (bacterial mats, lucinid/vesycomiid clams, and pogonophoran tube worms) have been cataloged in localized scattered habitats, generally on the periphery of mud-prone extrusives (Roberts, 2001). A study by Sassen et al. (1994) indicates that the hydrocarbons of rapidly vented sediments are non-biodegraded (by methanotrophic bacteria) as in other mineral-prone areas. The lack of fauna, identified by submersible and geophysical studies at mud-prone sites, suggest that these sites are unfavorable habitats for potential chemosynthetic organisms (MacDonald et al., 1990).

Transitional extrusive sites are believed to experience episodic or moderate flux of fluid and gas hydrocarbon expulsion. Side-scan sonar records exhibit scattered small-scale gas or fluid expulsion features and isolated authigenic carbonate deposits, which are often separated by the seafloor exhibiting a mottled or variable backscatter response (Fig. 2.12). Transitional cases are sometimes associated with exposed gas hydrates. Gas hydrates or clathrates are frozen (crystalline) ice composed of water and gas (Fig. 2.13). The gas in hydrates is most commonly methane, but other gases like H_2S and HS can be involved (Roberts, 2001). Gas hydrates are thought to typically occur below authigenic carbonates and the sediment-water interface, but are sometimes found exposed at the seafloor. MacDonald et al. (1994) believe that these hydrates act as a pressure relief system for seeps, alternately trapping and releasing hydrocarbons with the fluctuation of temperature due to hydrostatic pressure changes.

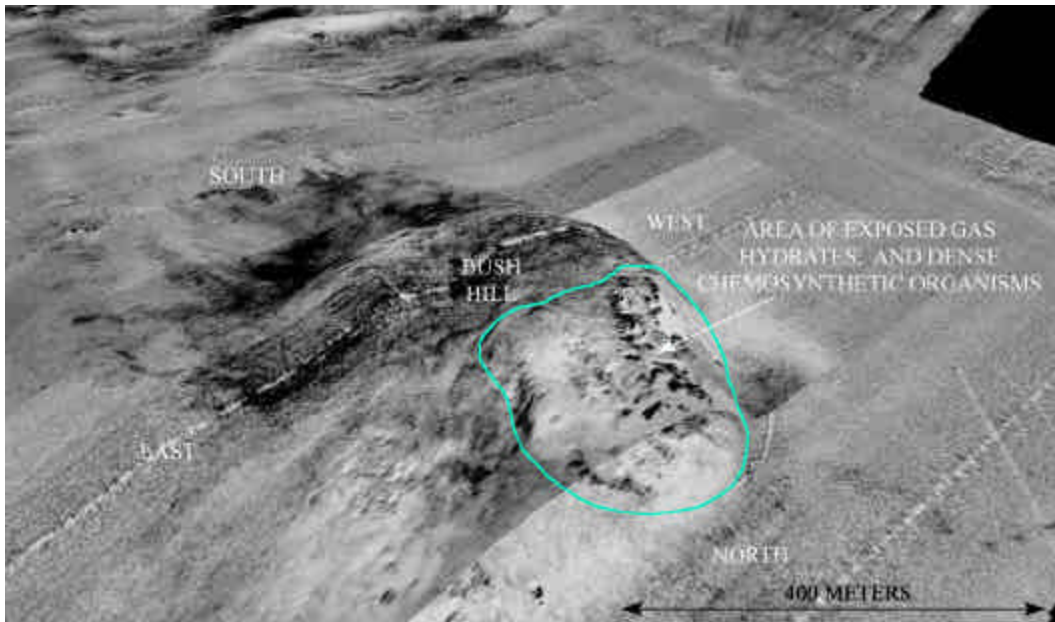


Figure 2.12. Digital terrain map of mosaic side-scan sonar records over the Bush Hill mound, Green Canyon Area (Block 184), showing known locations of exposed gas hydrates in the area outlined in blue.

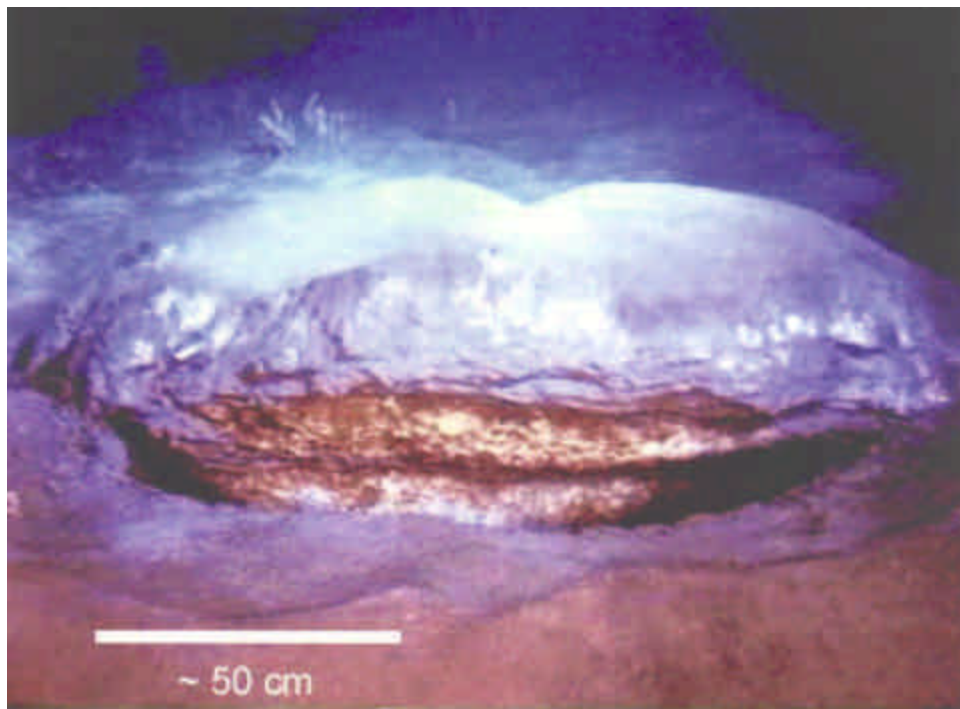


Figure 2.13. Exposed gas hydrate mound, Green Canyon Area (Block 234). From Sassen et al., 1999.

Transitional sites, where seepage of hydrocarbons and gas occur, appear to be oases for chemosynthetic organisms (Carney, 1994). Studies conducted by submersibles have cataloged dense and diverse chemosynthetic communities that live in or surrounding transitional extrusive sites. Dense colonies of vesitmentiferan and pogonophoran tube worms (Fig. 2.14; *Lamellibrachia* sp. and *Escarpia* sp.) and bathymodiolid seep mussels (Fig. 2.15; *Bathymodiolus* n. sp.) tend to be found within the seep area attached to large terraces of authigenic carbonates that are exposed or thinly covered by sediment. Lucinid/vesicomylid clams (Fig. 2.16); *Lucimoma* n. sp. and *Vesicomya* sp.) are often found buried within the mudflow sediments that typically surround these seep features (MacDonald et al., 1990). *Beggiatoa*, a bacterium that commonly forms mats that float at the sediment-water interface over hydrocarbon seepage, has been cataloged in both mud-prone and mineral-prone sites (Fig. 2.17). While the exact processes are poorly understood, these chemosynthetic organisms are believed to derive energy from reduced carbon, predominantly methane, and bacterial H₂S (Sassen et al., 1999).

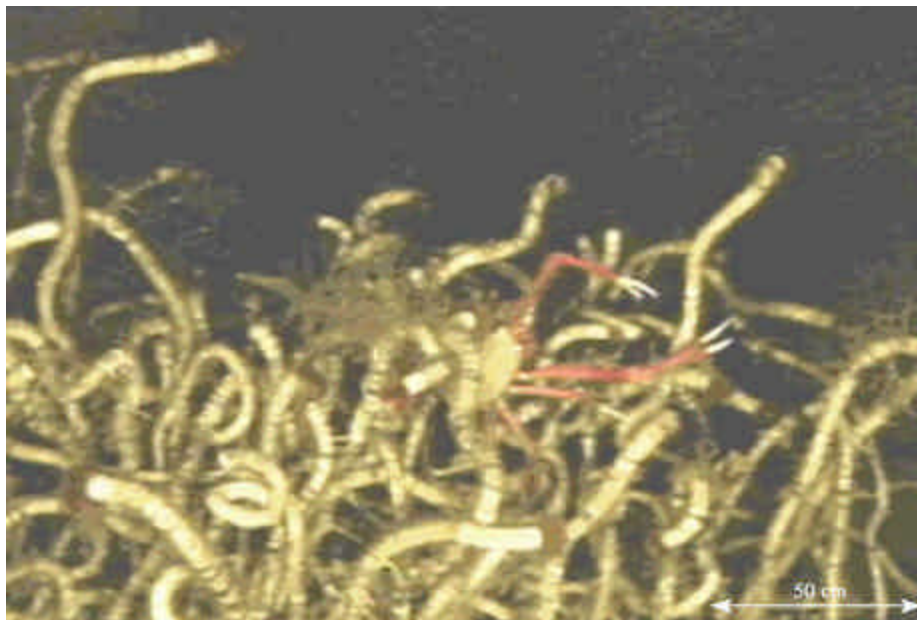


Figure 2.14. Vesitmentiferan tube worms (*Lamellibrachia* sp.) at an active seep in the Green Canyon Area (Block 66). From Barataria High School website (<http://bhs.ltd.edu/tubeworms.jpg>).

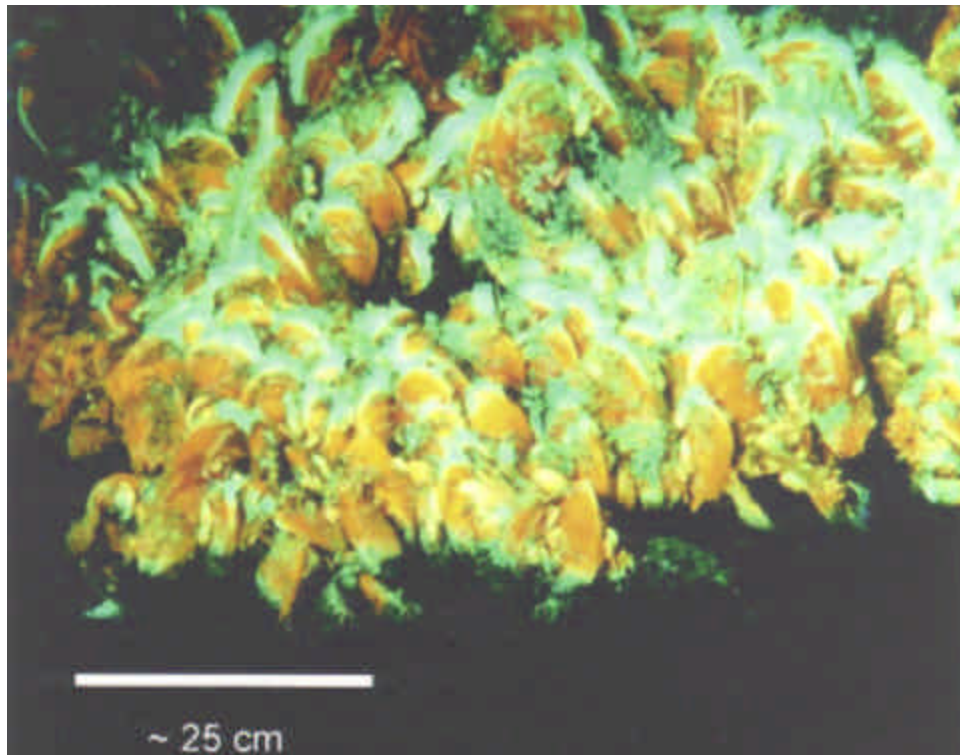


Figure 2.15. Methanotrophic mussel bed (*Bathymodiolus* n. sp.) from an active seep in the Green Canyon Area (Block 233). From Sassen et al., 1999.



Figure 2.16. Epibenthic aggregation of vesicomyid clams (*Calyptogena ponderosa*) from an active seep in the Atwater Valley Area (27°45'30"N, 89°58'18"W). From MacDonald et al., 1990.

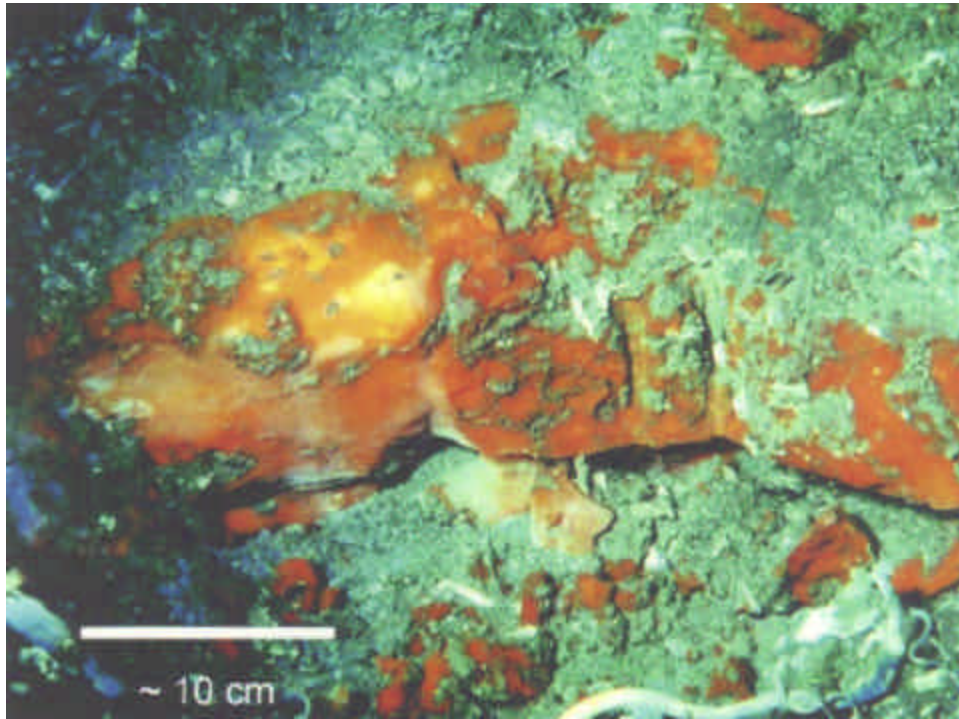


Figure 2.17. Orange and white beeggiatoa bacterial mats encrusting a gas hydrate mound in the Green Canyon Area (Block 184). From Sassen et al., 1999.

When geo-pressure is greatly reduced, as in mineral-prone sites, the fluids and gases rising to the seafloor no longer retain the capability to entrain larger amounts of muddy sediments. Venting is reduced to seepage of mineral-rich fluids and gases. Microbial utilization of these products causes the precipitation of mostly carbonates and mineral-prone features (mound-like structures) begin to form (Fig. 2.18). These mound-like structures are typically the sites of slow seepage of both hydrocarbon gases and crude oil. Subbottom profile records exhibit acoustic wipe-out zones below the mounds due to signal attenuation from the presence of bubble phase gas (Roberts, 2001). Microbial oxidation of seeping hydrocarbons catalyzes the production of both magnesium and calcium-rich carbonates (Ritger et al., 1987; Roberts et al., 1990; and Paull et al., 1992). Most of the samples acquired from seep sites in the Gulf of Mexico are comprised of magnesium rich-carbonates (Roberts and Aharon, 1994), although at

some sites dolomite comprises up to 40% of samples (Roberts et al., 1992b). Authigenically-derived carbonates create mound-like structures that range from < 1 m to 20 m relief or more. The relief exhibited by mounds represents the slow vertical growth of precipitated carbonate as mediated by methanotrophic bacteria.

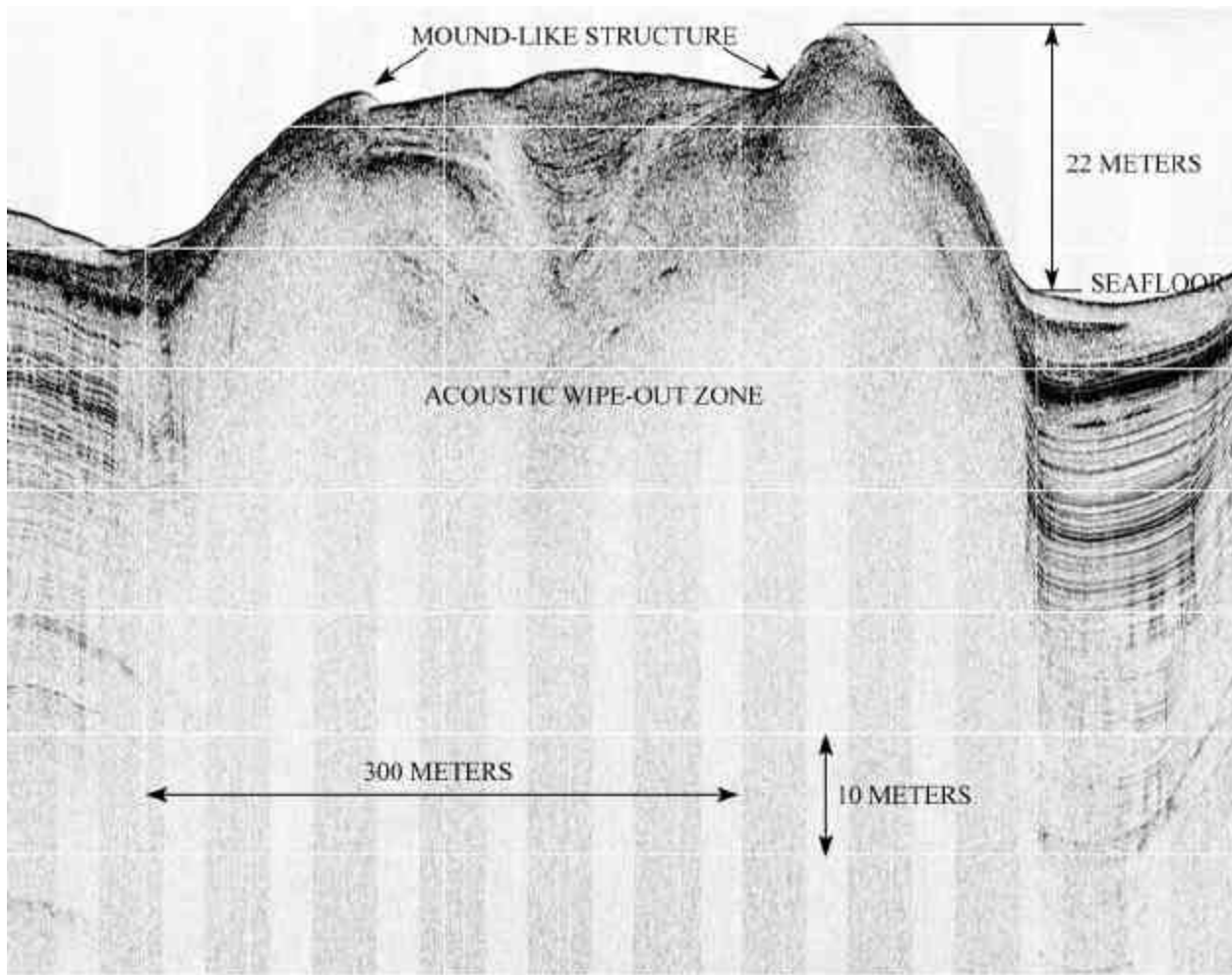


Figure 2.18. An east-west subbottom profile image of a large mound-like structure in the Green Canyon Area (Block 606). The acoustic wipe-out zone below the mound is due to attenuation of the signal by bubble-phase gas.

While mineral-prone sites tend to experience the most prolific authigenic carbonate accretion, they tend to accommodate fewer chemosynthetic organisms. This relationship may be because seepage is too slow to provide the trophic resources necessary to sustain the dense

chemosynthetic communities associated with transitional cases where these resources are stored in near-surface or surface exposures of gas hydrate (Roberts et al., 1990). Very localized patches of chemosynthetic organisms, including bathymodiolid mussels, vestimentiferan tube worms, lucinid/vesycomiid clams, and bacterial mats, occur around sites of slow seepage.

CHAPTER 3. INSTRUMENTATION AND METHODOLOGY

3.1 High-Resolution AUV Survey

The survey vessel M/V *Rig Supporter* operated by C & C Technologies carried the Autonomous Underwater Vehicle (AUV), and was used for field operations from September 9th through September 18th, 2003. Sea conditions varied during the data acquisition with wave heights ranging between 1 and 4 feet. A HUGIN 3000 AUV (Fig. 3.1) owned by C & C Technologies, Inc.'s, was used to collect all deepwater multi-sensor data for this survey. The AUV remote-sensing instruments included the Simrad EM2000 Swath Bathymetric Mapping System, the EdgeTech High-Resolution Sonar (120 kHz), and a Subbottom Profiler System (2-8 kHz).



Figure 3.1. The HUGIN 3000 Autonomous Underwater Vehicle (AUV) owned and operated by C & C Technologies, Lafayette, Louisiana.

3.2 HUGIN 3000 Autonomous Underwater Vehicle (AUV)

The HUGIN 3000 (High Precision Untethered Geosurvey and Inspection System) AUV is designed to collect deep-water, high-resolution geophysical data for site and route surveys in water depths up to 3,000 m (Fig. 3.2).

Primary survey sensors found in the system payload include a Simrad EM 2000 Swath Bathymetric System, EdgeTech Chirp Side-scan Sonar, and an EdgeTech Chirp Subbottom Profiler. An inertial guidance system is used for primary positioning of the underwater vehicle. Ancillary sensors include a precision depth sensor, altimeter, acoustic doppler log, and a salinity/temperature probe for calculating water column sound velocity. Transponders on the system for transmission of data include A HiPAP (High Precision Acoustic Positioning), ACL (Acoustic Command Link), and ADL (Acoustic Data Link). An aluminum/oxygen fuel cell powers the AUV for a period of up to 40 hours. Emergency ascent systems include a drop weight and air bag. A pinger, radio beacon, flashing light, and GPS/RF link output visual and remote sensing aids will be used in locating the AUV should an event occur where communication is lost with the survey ship.

Three industrial strength computers control all the system functions within the HUGIN. These computers are referred to as the Control Processor, Payload Processor, and Navigation Processor. The processors use artificial intelligence algorithms based on feedback returned from the more than 75 sensors to make real-time decisions regarding the system performance. Two titanium spheres house the payload and control, consisting of computers and dual 50-gigabyte data storage drives.

Three ship-borne computers communicate continuously with the vehicle while it is in operation. The HUGIN Operator Station is responsible for monitoring all the sensors carried by the vehicle and generates warnings to the operator when the values stray out of the optimal range. The

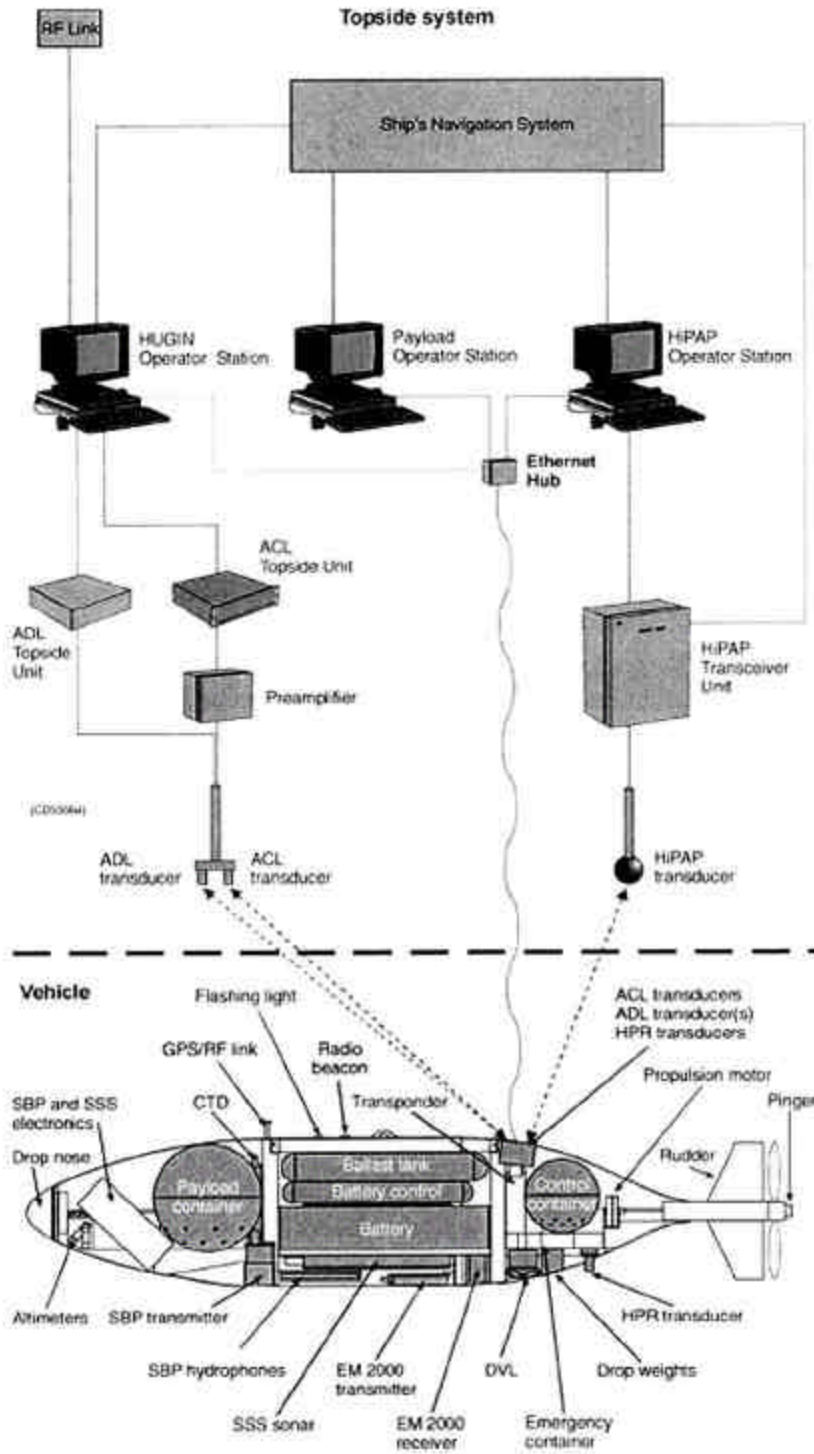


Figure 3.2. Command and control computer flow chart and HUGIN 3000 AUV schematic diagram.

Payload Operator Station computer provides the user with graphical views of 10 to 15 percent of the subbottom, bathymetry and side-scan sonar data being recorded. It also allows the user to turn the systems on or off, adjust instrument settings as needed, and verify data quality. The third topside computer is the HiPAP Operator Station. This computer provides a real-time graphic display of the HUGIN vehicle's subsurface position and the surface position of the mother ship, which travels directly above the AUV while the collecting data. Differential GPS data provide the mother ship positions while the AUV vehicle positions are calculated using ultra short baseline acoustics (USBL), inertial navigation and Doppler velocity speed log.

Primary positioning of the HUGIN is controlled by the inertial navigation system. This system uses precision gyros and accelerometers to maintain the AUV track of the mission plan (trackline running sequence). The mission plan is downloaded to the HUGIN system computers before deployment. The HiPAP system and Doppler velocity speed log provide input into the inertial navigation system for guidance system checks. These inputs are weighted and applied to the positioning solution using a Kalman digital filter. Post processing routines can be implemented to further refine the subsea positions.

Simrad's EM 2000 Swath Bathymetry System (Multibeam) collects soundings in approximately a 200-meter swath underneath the HUGIN vehicle. An onboard velocimeter provides real-time data at the transducer for proper beam forming of the acoustic transmissions. The system is capable of collecting 111 beams or soundings across the swath. A high-precision depth sensor provides the depth of the HUGIN vehicle. The data are processed utilizing C & C's HydroMap software. Multibeam data were collected to create XYZ files for profile view and contour generation on the survey maps. The multibeam soundings were collected in about a 220-meter swath beneath the AUV. Multibeam data were processed at a 3-meter bin size utilizing a

median filter. A gridded dataset was then generated from the output median points by applying a weighted-neighbor filtering algorithm. A precision depth sensor recorded the AUV depth. Salinity and temperature measurements needed for correct beam forming for the multibeam system on the AUV were continuously logged with a velocimeter.

The HUGIN is equipped with a dual frequency chirp EdgeTech Side-Scan Sonar that uses a calibrated wide band digital frequency modulated (FM) signal to provide high-resolution, low-noise images. This sonar simultaneously transmits linearly swept FM pulses centered at two discrete frequencies: 120 kHz and 410 kHz. The raw data files are post-processed and converted to XTF (eXtended Triton Format) for digital interpretation and hardcopy generation.

Seismic profiles are collected with an EdgeTech Chirp Subbottom Profiler. The transmit pulses are generated in the frequency band between 2 and 8 kHz. The system takes advantage of built-in deconvolution of the system response of the output pulse. The sonar's measured system impulse response is used to design a unique output pulse that will prevent the source from ringing. The raw seismic data can be post processed to create both SEG-Y and XTF datasets.

All the raw digital data were logged utilizing software developed by C & C Technologies, Inc. The multibeam system delivered a 3 m gridded dataset with vertical accuracies within 20 cm. Triton-Elics software was used to review the side-scan sonar and subbottom data and to produce hardcopy data. Objects of the order of about ½ meter can be detected with the side-scan sonar system. The vertical resolution with the subbottom profiling system is estimated at 10 cm with at least 75 m of subbottom strata being resolved in most areas.

3.3 Positioning

Positioning of the mother vessel is accomplished using differential GPS with the C-Nav Navigation System used for relaying the corrections. C-Nav is a globally corrected differential GPS

system owned and operated by C&C Technologies, Inc. Differentially corrected GPS positions are generally accurate to within 1 m. AUV vehicle positions were calculated using a Kalman filter algorithm, which uses input data from a Simrad HiPAP System (High Precision Acoustic Positioning), inertial navigation and a Doppler velocity speed log to provide a position solution. AUV navigation fix positions were recorded and annotated in the digital data and on the hard copy data at 150 m intervals.

3.4 Interpretation

The interpretation of side-scan sonar and subbottom profiler data is accomplished by using Triton-Elics viewing software, called ISIS. The software presents the data in a horizontal or vertical waterfall, enabling the interpreter on-screen continuous viewing of each line file. A digitizing tool within the software allows the interpreter to measure, digitize, and export interpretative data directly from the screen. The digitized interpreted data is exported in a DXF (ASCII) format, which can be imported directly into AutoCAD 2000 for cartography.

3.5 Cartography and Data Reproduction Images

Four different types of maps were generated with the data from this survey (Appendix A). The first and second Color Shaded Bathymetry Map (Appendix A, Sheet 1) and Gradient Map (Appendix A, Sheet 2), consist of multibeam 3-meter bin geo-spatially oriented TIF images generated in Hydromap, a software developed by C & C Technologies, Inc. The TIF images are exported to AutoCAD 2000 for cartographic display. Bathymetric contours are generated in AutoCAD 2000 from an ASCII XYZ coordinate file that is also output from Hydromap. The third map, a Side-Scan Sonar Mosaic (Sheet 3), is a mosaic compilation of the side-scan sonar lines accomplished in a program called OICSwath. OICSwath also generates a geo-spatially oriented TIF image that is imported into AutoCAD 2000 for cartographic display. The final map, a Geologic

Interpretation Map, is generated in AutoCAD 2000 from interpreted side-scan sonar, subbottom profile, and multibeam data.

The geodetic datum used for the set of study maps (Appendix A) produced for this survey is the NAD 27 and the ellipsoid used is the Clarke 1866. The datum is projected using the Universal Transverse Mercator (UTM), Zone 15 North (15N). All grid units, as well as scales and measurements are in US Survey feet.

Several data reproduction images are used in this study to exhibit seafloor and subbottom features. Basic side-scan sonar and subbottom profiler data reproductions were exported directly from the ISIS (Triton-Elics) viewing software in a TIF format and then annotated using Adobe Photoshop software. Digital Terrain Map (DTM) images are created in a program called Fledermaus created by Interactive Visualization Systems. The XYZ (ASCII) bathymetry file generated by Hydromap is imported into Fledermaus, which generates a three-dimensional DTM of the bathymetry. The side-scan mosaic, created earlier, IS then draped across this DTM in Fledermaus. Three-dimensional screen-shots of the data are then exported, in TIF format, to Adobe Photoshop for annotation.

3.6 3D Seismic Survey Maps

ENI Petroleum of Houston, Texas, provided a water bottom amplitude extraction map (Appendix B, Sheet 1), a water bottom dip map (Appendix B, Sheet 2), and several 3D seismic profile images (See Chapter 5) to facilitate the 3D seismic interpretation portion of this thesis. The maps were generated from a merge of the Phase 11 and the Phase 13 3D Ultra surveys conducted by Western Geco in the Green Canyon Area (Appendix D). A rather strong acquisition footprint and some amplitude balancing issues are evident on the maps at the merge of the Phase 11 and Phase 13 surveys. However, these seismic merging problems do not affect the interpretation given here as

they occur on the southeastern portion of the survey area away from the feature-rich area. Generally a 3D survey would be reprocessed for higher resolution if it were intended to replace a shallow hazard survey. The time data from this survey has not had any additional processing for higher frequency and resolution.

3.7 3D Survey Specifics

The Western Ultra survey is a post stack time migration. The natural bin size has an inline spacing of 20 m (65.62 ft) and common depth point spacing of 12 m (41.01 ft). The sample rate is 4 ms Two-Way Travel (TWT) time and the dominant frequency at the water bottom is between 25-30 Hz. This gives a resolution thickness of 14 m to 17 m (45 ft to 55 ft).

3.8 Water Bottom Amplitude Extraction and Dip Maps

The water bottom extraction map and dip map (Appendix B, Sheets 1 and 2), provided by ENI Petroleum, have only positive values that are scaled to the interpreted seafloor horizon. This is because the amplitudes that were mapped are snapped to the first largest positive amplitude or peak amplitude. This peak positive amplitude was interpreted as the seafloor horizon and used to generate the water bottom extraction map. The TWT time in seconds per foot from the interpreted seafloor horizon was then used to generate the dip map. The dip map provided shows the dips in gray scale. Faulting and extrusive features with increased slope appear darker on the map.

3.9 3D Seismic Profiles

The 3D seismic profile images appear in Chapter 5 of this thesis. The vertical scale is set at 10 in/sec and shows depth as a factor of TWT time. The horizontal distance between traces is 12 meters. The seismic profile and color bar have both the negative amplitude, which is red and

a trough and positive amplitude as black, and a peak with the range determined by the full seismic volume.

CHAPTER 4. DESCRIPTION AND INTERPRETATION OF HIGH RESOLUTION DATA SET

4.1 Overview Description of Seafloor Features

The study area is approximately 14.4 km (9 miles) by 7.2 km (4.6 miles) in size, trends northwest to southeast, and occurs in the central eastern Green Canyon Area, Gulf of Mexico (Fig. 2.1). In the northeastern portion of the study area, halokinesis (salt tectonics) has uplifted a large wedge-shaped fault block causing massive faulting (Fig. 4.1 and Appendix A, Sheet 1). The highest point or dome of the wedge shaped fault block has been uplifted approximately 128 m (420 ft) above the surrounding seafloor from a depth of 1009 m to a depth of 1,137 m (3,730 ft) below sea level. The surrounding seafloor dips away from the dome highpoint, to the southwest and the east. A massive fault system, trending northwest to southeast across the bulk of the study area, marks the eastern margin of the uplifted wedge. Major faulting, trending northeast to southwest, mark the northern margin of the uplifted wedge. Several extrusive features, a mud volcano, two mud vents and multiple mound-like structures, occur on the downthrown block to the east of the massive fault system (Fig. 4.2).

At the southern end of the survey area, the seafloor bathymetry radically changes its dip directions to the east and the south, as it opens into a horseshoe shaped bowl depression (Fig. 4.1). A hummocky seafloor, from a long buried mass-movement event (as interpreted from seismic data), occurs on the northern slope and into the basin of the horseshoe shaped bowl depression. Multiple erosional gully features can be seen emptying into the bowl feature from the northwest and west. The deepest portion of the survey, 1,344 m (4,410 ft) below sea level, occurs in the southeastern corner of the study area within the horseshoe shaped depression. Additional erosional gullies occur on the western and the eastern side of the uplifted fault wedge, trending north to south and west to east, respectively.

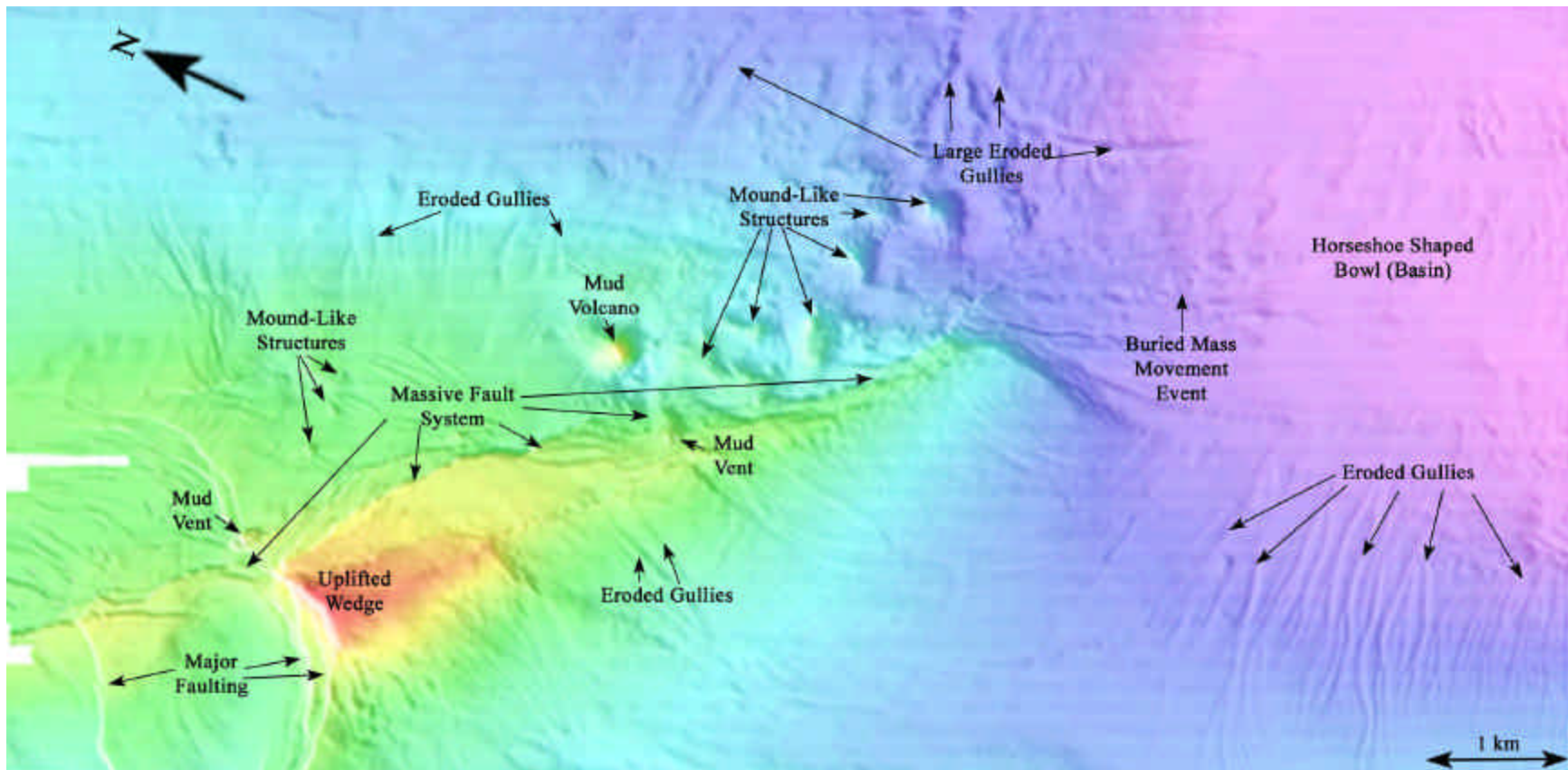


Figure 4.1 Multibeam bathymetry DTM image of the study area in central eastern Green Canyon Area, Gulf of Mexico. This Figure illustrates the locations of the pertinent seafloor features in the study area.

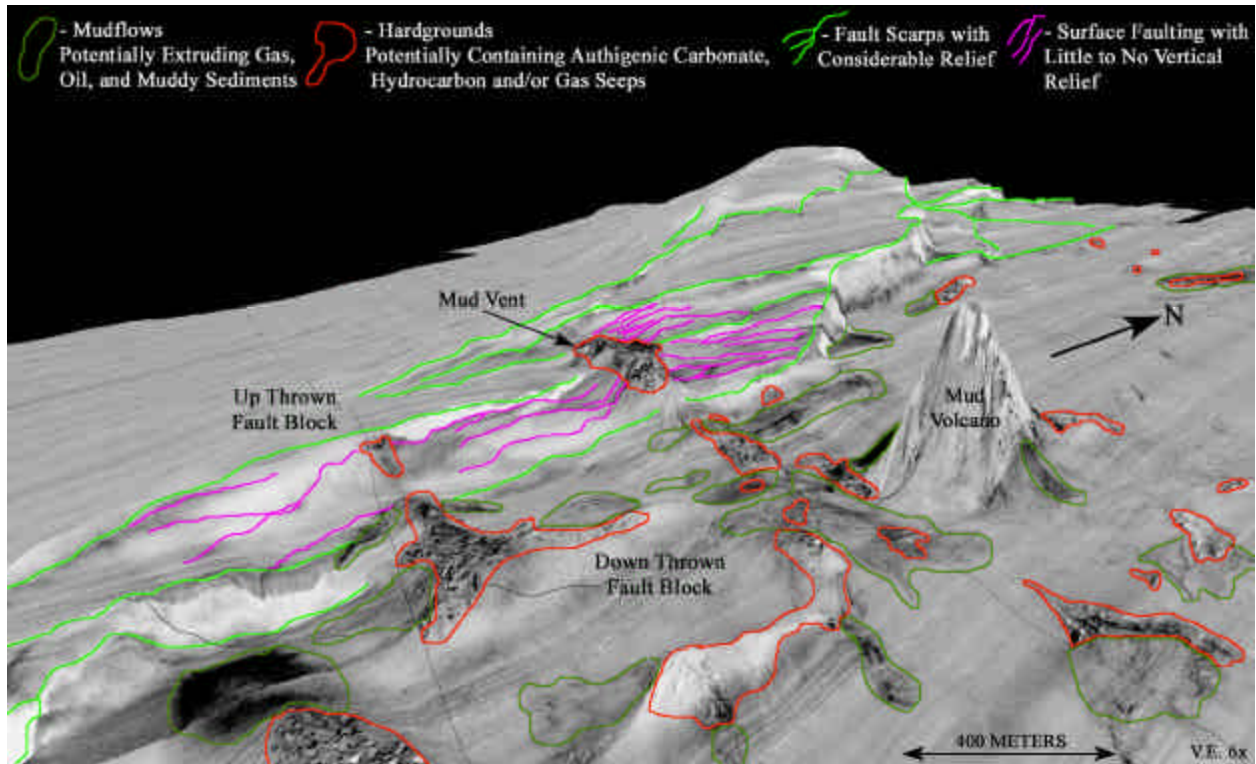


Figure 4.2 DTM of a draped side-scan sonar mosaic illustrating the faulting, mud volcano, mud vents, mudflows, and mound-like structures (hardgrounds) interpreted on the down thrown block of the massive fault system in the study area.

4.2 Overview Description and Interpretation of Subbottom Features

Subbottom profiles show 50 to 60 m (164 to 196 ft) of penetration within the study area (Fig. 4.3 and 4.4). The key features detected by the subbottom profiler are hemipelagic drape, buried slumps, faulting, and acoustic wipe-out zones (Appendix A, Sheet 3).

The bulk of the survey area, except for those areas with active extrusion taking place (mound-like structures, mud volcanoes, mud vents, and mudflows (Fig. 4.4), is covered with a 2 to 9 m (6 ft to 28 ft) thick hemipelagic drape. Hemipelagic drapes are generally comprised of fine-grained clays and foraminiferal tests (Roberts, 2001). During high sea level (highstand) quiescent conditions fine-grained clays and foraminiferal tests (microscopically sized shells) fall down through the water column like rain slowly accumulating a layer called a hemipelagic

drape. The fact that the hemipelagic drape deposits cover the survey area and blanket the faulted regions (Fig. 4.3) suggests that the area has not undergone any recent uplift and faulting or sediment failure.

A unit of parallel to semi-parallel “laminated” reflectors with medium to high amplitudes is evident below the hemipelagic layer (Fig. 4.3). The unit ranges 17 to 24 m (56 to 78 ft) in thickness and marks the base of the interpretable subbottom data below the seafloor. Parallel laminated reflectors are associated with the cyclic deposition, which occurs during high sea level conditions. A chaotic mass movement event, with the occasional non-continuous medium reflectors, is evident below the unit of parallel laminated reflectors.

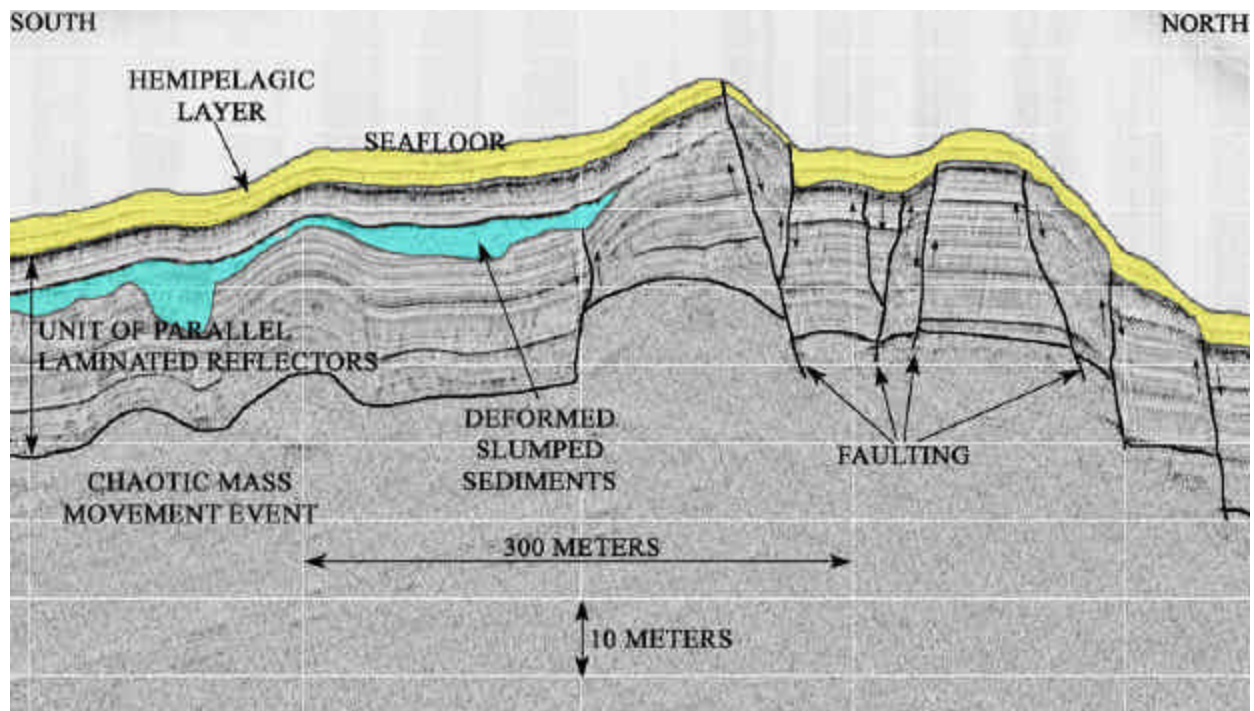


Figure 4.3 This image illustrates the stratigraphy recorded by the subbottom profiler: hemipelagic layer (at the seafloor), unit of parallel laminated reflectors (below hemipelagic sediments), and chaotic mass movement event (below parallel laminated reflectors). It also exhibits the uplift and resultant slumping and faulting that has taken place in the study area.

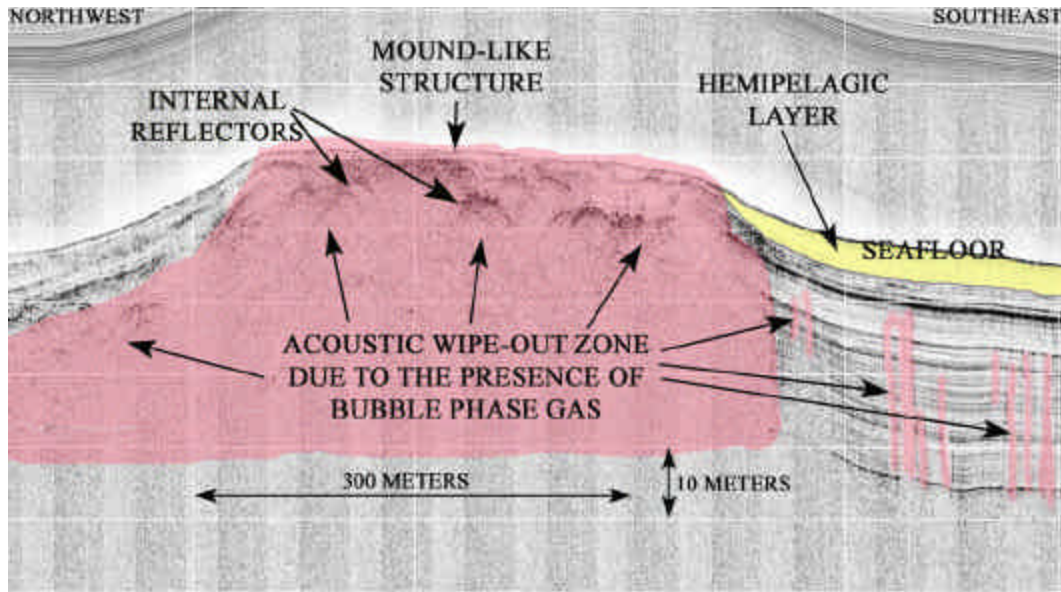


Figure 4.4 Subbottom profile record, from the study area, showing acoustic wipe-out zones and the missing hemipelagic layer across the mound-like extrusive feature.

Acoustic wipe-out zones were imaged on subbottom profiles on the downthrown side of the massive fault system within the survey area (Appendix A, Sheet 3). Acoustic wipe-out zones are defined as areas with a lack of distinct acoustic reflection (Fig. 4.4). This lack of acoustic response is most commonly associated with attenuation of the sonic signal due to bubble-phase gas in the surface and shallow subsurface sediments (Hovland and Judd, 1988; Roberts, 2001).

4.3 Faulting

A massive fault scarp or fault system (Fig. 4.5) occurs on the eastern side of the uplifted wedge, which exhibits the greatest relief 29 m (95 ft) and largest gradients (between 20° and 63°) in the survey area (Appendix A, Sheets 1, 2, and 3). This major fault trends northwest to southeast across the upper two thirds of the study area and is the central feature to which all the remaining lesser surficial faults are tied. The ridge like topography of the massive fault system suggests an elongate tongue of salt may be responsible for the seafloor morphology (Lee et al., 1989).

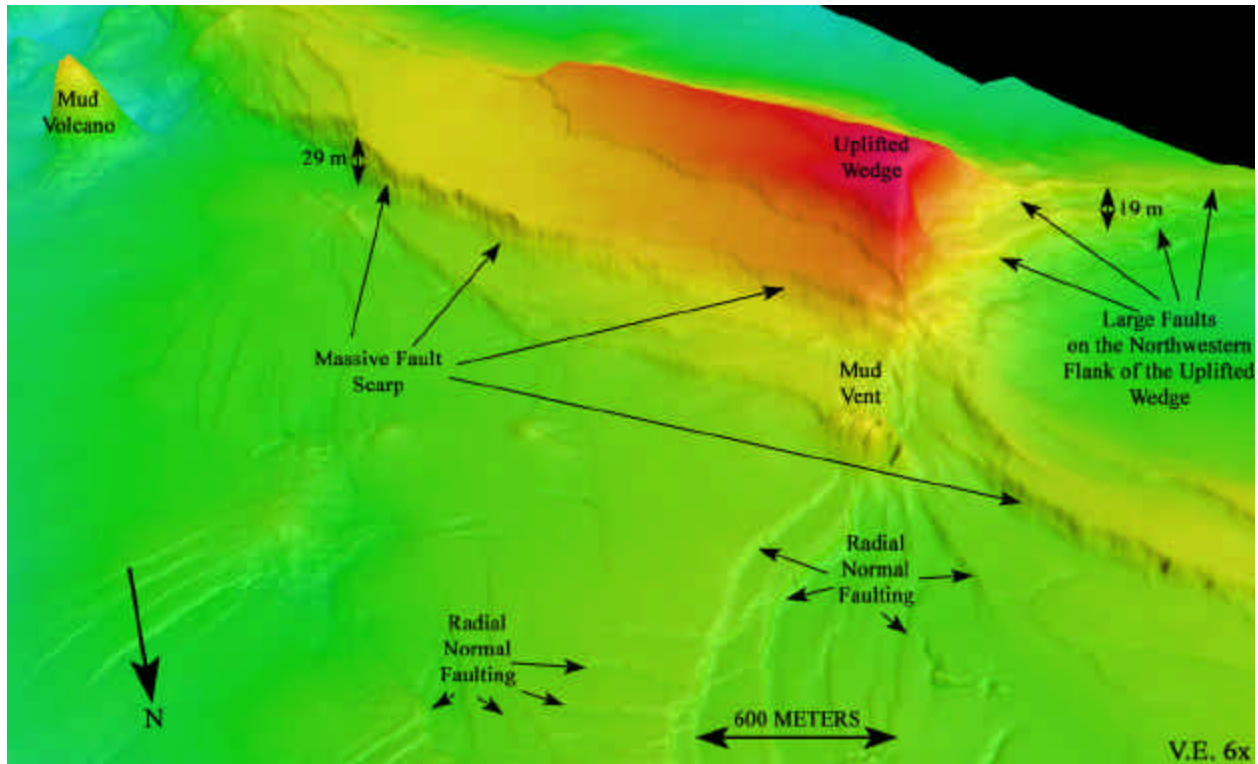


Figure 4.5 A DTM of the multibeam data illustrating the massive northwest to southeast trending fault scarp (system) and the ancillary lesser related faulting in the northwest quadrant of the study area.

Several large faults, trending southwest to northeast, occur on the northern flank of the uplifted wedge. These large faults appear to intersect and terminate at the massive fault scarp. These faults scarps exhibit relief of 2.4 to 19.2 m (8 to 63 ft) and local gradients between 6.5° and 30° . The bulk of the remainder of the faulting radiates outward to the northeast from the massive fault system. These lesser faults exhibit local gradients between 2.5° and 17° and scarp heights between 0.6 and 5.2 m (2 and 17 ft).

The lesser faults are generally smaller and often occur as radial normal faults and may be related to over-pressured extrusion of subsurface sediment. A recent paper by Vendeville et al. (2003), on the radial faulting above salt diapirs, provides a process model (Fig. 4.6). Though

that paper is written for salt extrusion the process can be equally applied to the formation of the radial faulting seen in the study area.

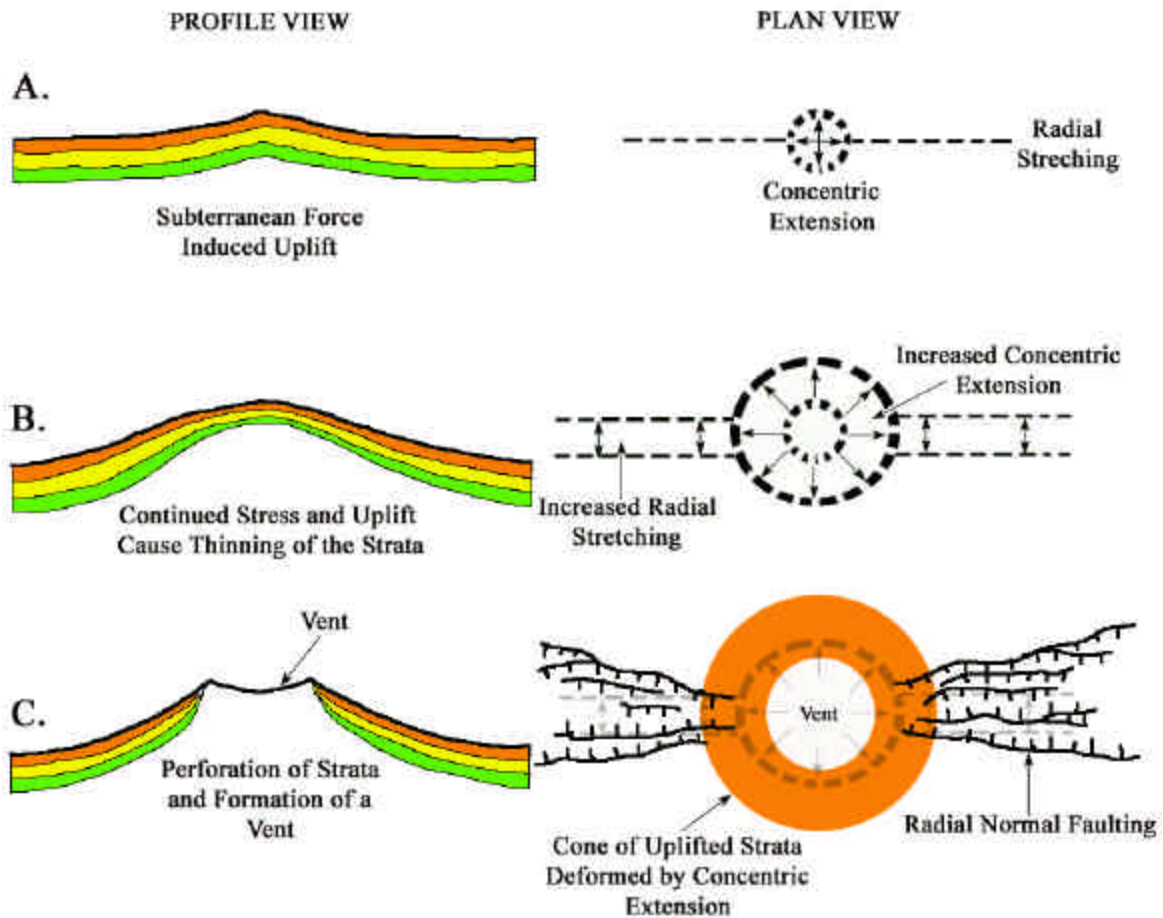


Figure 4.6 Schematic diagram illustrating a process model for the formation of radial normal faulting and extrusion at the site of geo-pressured uplift by subterranean forces. Modified from Vendeville et al., 2003.

First, subterranean forces below thin strata induce uplift causing concentric extension at the crest of the uplift and radial stretching (Fig. 4.6 A). Continued stress below this crest results in further uplift and thinning of the strata above the central point of the pressure inducing more concentric extension. Increased radial stretching and the formation of radial normal faults accommodate this concentric extension (Fig 4.6 B). Because concentric extension rapidly decreases laterally, the radial faulting dies out along strike. If concentric extension continues, the strata are no

longer able to withstand the pressure and a vent opens at the central point of pressure (Fig. 4.6 C). This process may be responsible for the mud prone (mud volcanoes and mud vents) features that occur on the seafloor in areas of salt-derived deformation.

4.4 Mud Volcano

A mud volcano, 76 m (250 ft) tall and 518 m (1,700 ft) wide at the base, (Figs. 4.7 and 4.8) is evident in central portion of the study area. A review of literature indicates this feature may be the tallest yet reported in the Gulf of Mexico. Mud volcanoes are believed to occur when gas-filled formation fluids rapidly force fine-grained sediment up faults. This mud volcano is interpreted to be active because a crater is apparent on DTM draped mosaic images (Fig. 4.7) and no evidence of hemipelagic drape occurs across the subbottom image in Figure 4.8. If the volcano were dormant, a hemipelagic drape would blanket the volcano and fill in the crater (Neurauter and Roberts, 1992).

This feature surprisingly does not stand directly upright, but leans a few degrees to the south (Figs. 4.5 and 4.7). A noticeable displacement in the distribution of the sediments is apparent in Figure 4.8. The crest of the feature does not occur directly above the center of the mass, but is shifted approximately 49 meters laterally to the south. A 12 m (40 ft) deep, 225 m (740 ft) wide depression is located at the southern foot of the feature, which may explain the southward incline of the mud volcano (Fig. 4.8). An examination of the bathymetry of another active mud volcano in Green Canyon Block 143 (Fig. 2.10) indicates that a similar depression also occurs at the southern base of this analog. Interpretation of subbottom profile data at the Block 143 mud volcano indicates that buried radial graben faulting occurs to the south and the north of the mud volcano and this may be responsible for the depression (Unpublished data from a 2003 AUV survey). The same may be true of the mud volcano in this study area but the

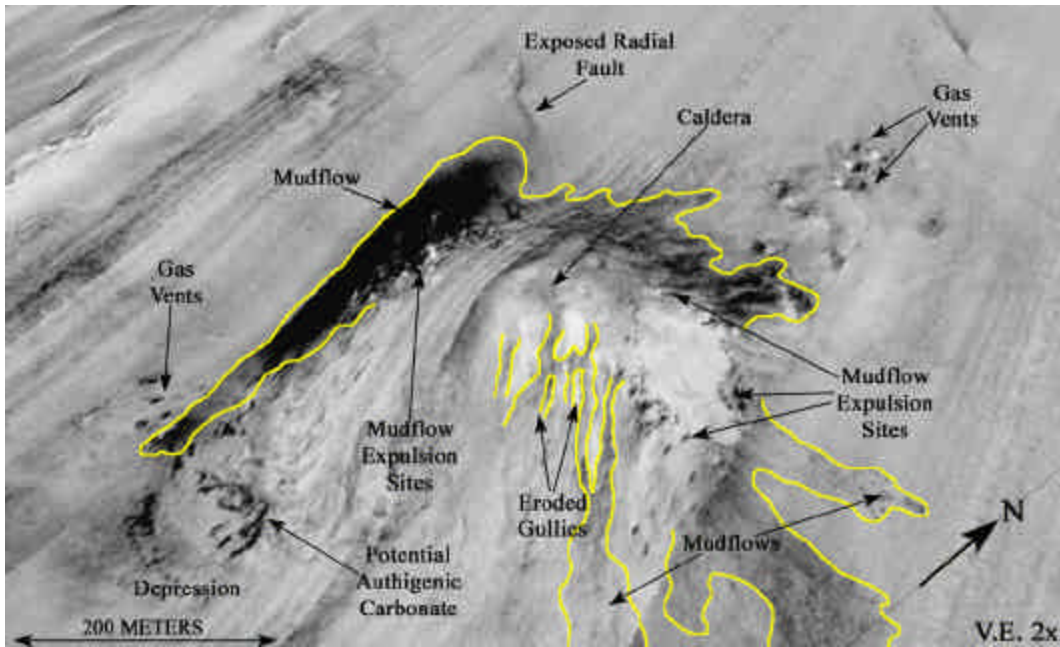


Figure 4.7 DTM of a draped side-scan sonar mosaic illustrating the crater, vents, potential authigenic carbonates, mudflows, radial faulting and eroded gully features associated with the mud volcano in the study area.

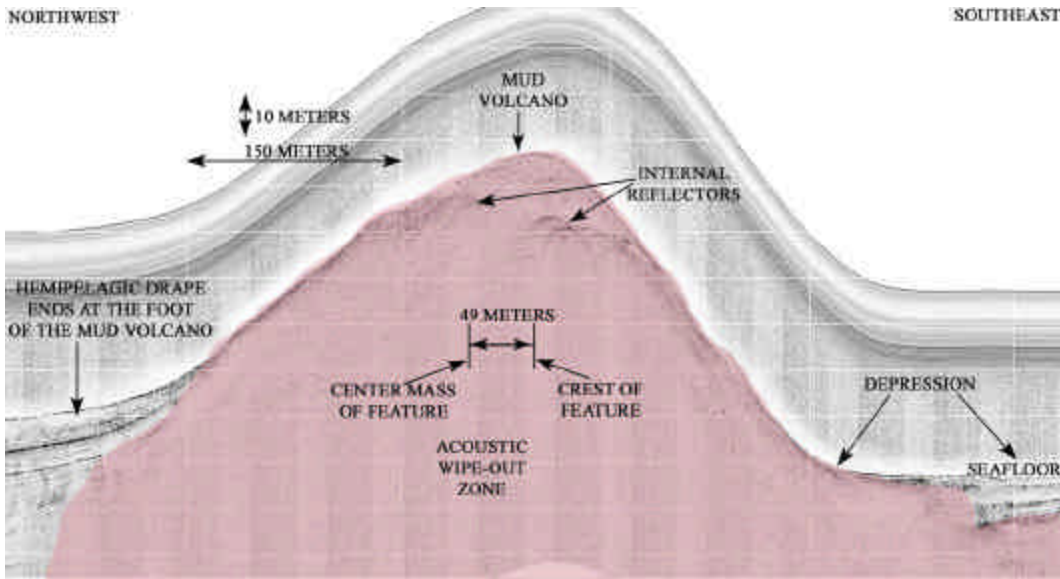


Figure 4.8 Subbottom profiler image across the flank of the mud volcano in the study area. Of note are acoustic wipe-out of the entire feature, internal reflectors within the feature, the hemipelagic drape is missing across the top of the feature, a depression on the southern side of the feature, and the preferential deposition of sediments approximately 49 meters south of the center mass.

northwest to southeast trend of the 2D tracklines and substantial acoustic turbidity of the near seafloor sediments may mask this faulting (Appendix A, Sheet 3). During the formation of the mud volcano, the displacement of extruded sediments from below the area around the feature may have reinvigorated the collapse response of the graben causing the formation of the depression. The result of the reinvigorated collapse of the graben probably caused the southern flank of the mud volcano to sink, causing its southward inclination and southward preferential deposition of sediment over that of center mass. A full discussion of the forces, believed to lead to the formation of radial normal faulting around mud prone features, is included in section 4.3 (Faulting) above.

Several seafloor features occur on both the flanks and periphery of the mud volcano (Fig. 4.7). On side-scan sonar records, the darkness or amplitude of the return is a reflection of the density of the sediment (Trabant, 1984). Therefore, the relative density exhibited by the features in Figure 4.7 is discernable by the darkness it exhibits. Gullies have formed just below the crater on the southeastern flank. These features were eroded by sediments that breached the lip of the crater and cascade down the flanks of the mud volcano with erosive force. Expulsion sites, appearing as scattered dark spots, occur approximately halfway down the flanks of the mud volcano, some distance away from the crater. These sites are believed to be the location of slow seepage of gas and hydrocarbon-laden muds, which, when extruded, form mudflows. The dark spots seen here are believed to be authigenic carbonate, mineralized as a by-product of microbial activity at the extrusion site. Mudflows, originating from these extrusive sites and the crater, occur around the base of the mud volcano. A large dark high backscatter mudflow is recorded at the base of the western flank of the mud volcano. This dark character exhibited by the mudflow suggests the mudflow is relatively old with a rough shell covered and partially cemented surface.

Several large vents, on the northern and southwestern periphery of the mud volcano, are believed to extrude only gas. This interpretation is given because these features do not appear to exhibit vertical growth or possess mudflow extrusives.

The seafloor features exhibited on side-scan sonar records may be indicative of the current flux of sediment extrusion experienced by the mud volcano. The position of the eroded gullies on only the southern face of the volcano suggests that this is the prevalent path of extruded sediments. The fact that extrusive sites appear only halfway down the mud volcano's flanks suggests eruptive or copious venting of muddy sediments may only be enough to blanket the top half of the cone. These criteria suggest a moderate flux rate or episodic expulsion for the mud volcano and its periphery (Roberts, 2001).

4.5 Mud Vents

Two features, interpreted as mud vents, occur in the study area. The first is situated southeast of the massive fault system in the northwest quadrant of the study area (Fig. 4.1, 4.5, and 4.9). This feature is rather large expressing 21 m (70 ft) of relief, a cone width of 169 m (555 ft), several small vent openings 1.5 to 3 m (5 to 10 ft) deep, and a cumulative vent width of 97 m (320 ft). The second mud vent is centrally located directly on the massive fault system within in the study area (Fig. 4.1, 4.2, and 4.10). It exhibits only 5 m (17 ft) of relief, a total cone width of 131 m (430 ft), a single vent 12 m (29 ft) deep, and a vent a width of 73 m (240 ft). Mud vents are thought of as smaller versions of mud volcanoes, which theoretically possess less transport of fluids, gases, and fine-grained sediment (Roberts, 2001). These features, despite their size difference, are surprisingly similar. Each possesses vents surrounded by a cone expressing vertical relief and radiating normal faults that generally occur along the direction of strike of other major faulting in the area (Fig. 4.11).

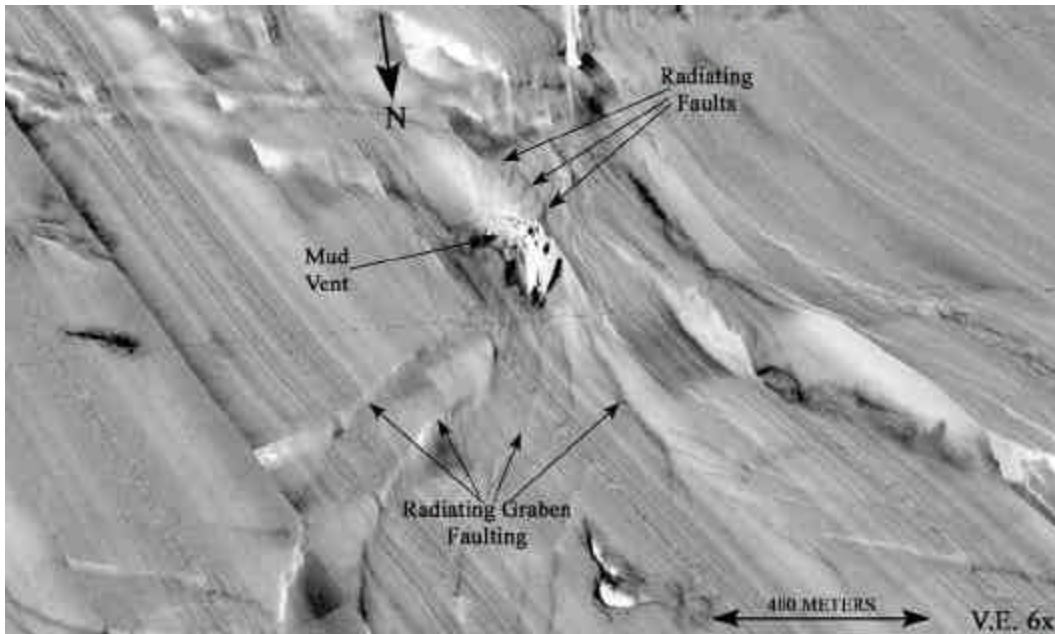


Figure 4.9 DTM of a draped side-scan sonar mosaic illustrating the mud vent southeast of the massive fault in the northwest quadrant of the study area and its radiating normal faulting.

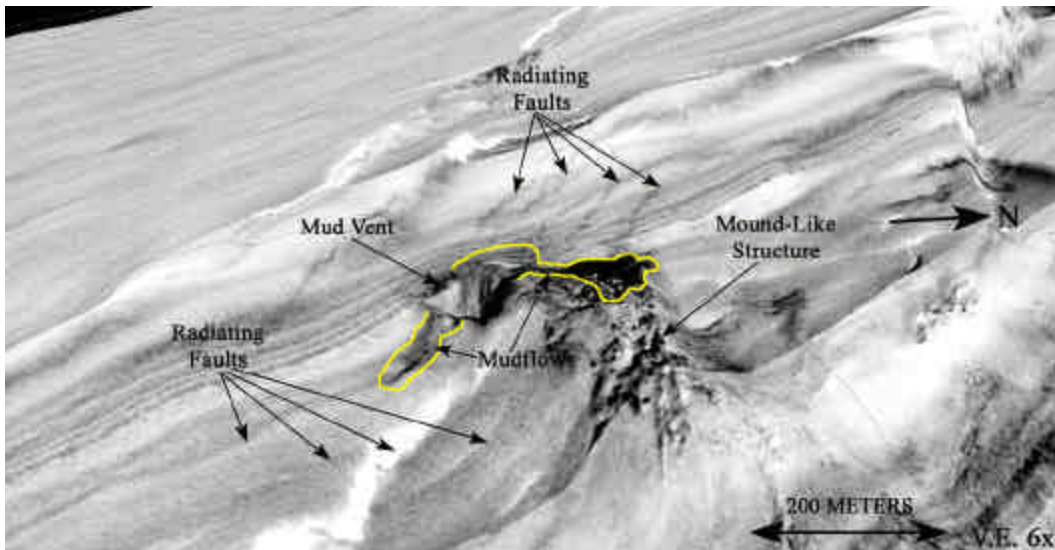


Figure 4.10 DTM of a draped side-scan sonar mosaic illustrating the mud vent that is centrally located directly on the massive fault system within in the study area. Radiating normal faulting, a mound-like structure, and mudflows are some of the features in close periphery to the mud vent.

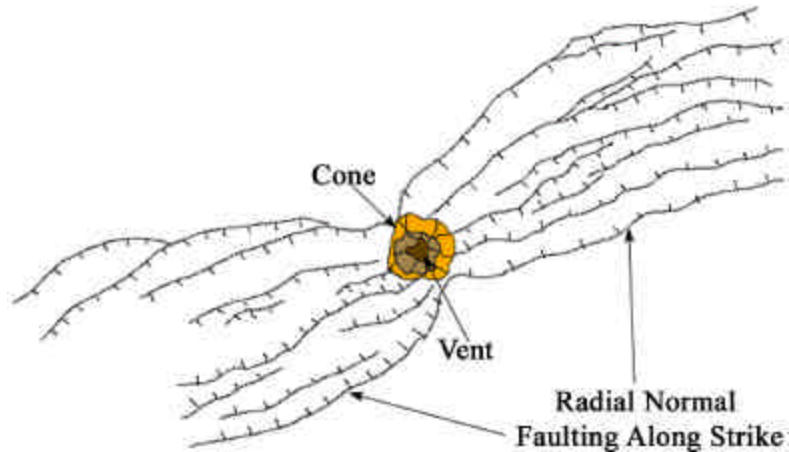


Figure 4.11 Schematic diagram illustrating a plan view of the anatomy of a mud vent.

The mud vent exhibited in Figure 4.9 has no related seafloor features on its periphery, while the mud vent exhibited in Figure 4.10 has a mound-like structure and some recent mudflows around its cone. The seafloor features that are absent from the first mud vent (Fig. 4.9) may indicate that the feature is dormant or potentially venting only gas. The small mudflows and the mound-like structure in close vicinity of the second mud vent (Fig. 4.10) suggest slow seepage of gas and hydrocarbon-laden muds. Moderate to high flux of discharge muddy sediments would have blanketed and stifled the mound-like structure and the relative size of the mudflows suggests only episodic seepage from the vent.

4.6 Hardground Features

Faulting creates a conduit for hydrocarbons and gas to escape lower strata causing the formation of hardgrounds on the down-thrown fault block of the study area (Roberts, 2001). On side scan sonar mosaics, hardgrounds appear as areas of darker returns characterized by a moderate to high degree of roughness. Two different types of hardgrounds were imaged on the seafloor in the study area: mound-like structures (Fig. 4.12) and mineralization above faults (Fig. 4.13). Twenty-seven mound-like structures and twenty areas of mineralization above faults

were recorded on the down-thrown block of the study area (Appendix A, Sheet 3). The mound-like structures tend to occur on or close to the massive fault system, while the mineralization above faults occurs further east on the periphery of the mound-like structures. The hardground features imaged in Figures 4.12 and 4.13 are probably the result of moderate to slow seepage of both hydrocarbon gases and crude oil. Microbial degradation of hydrocarbons is believed to catalyze the synthesis of both calcium and magnesium rich authigenic carbonates (Roberts et al., 1992b).

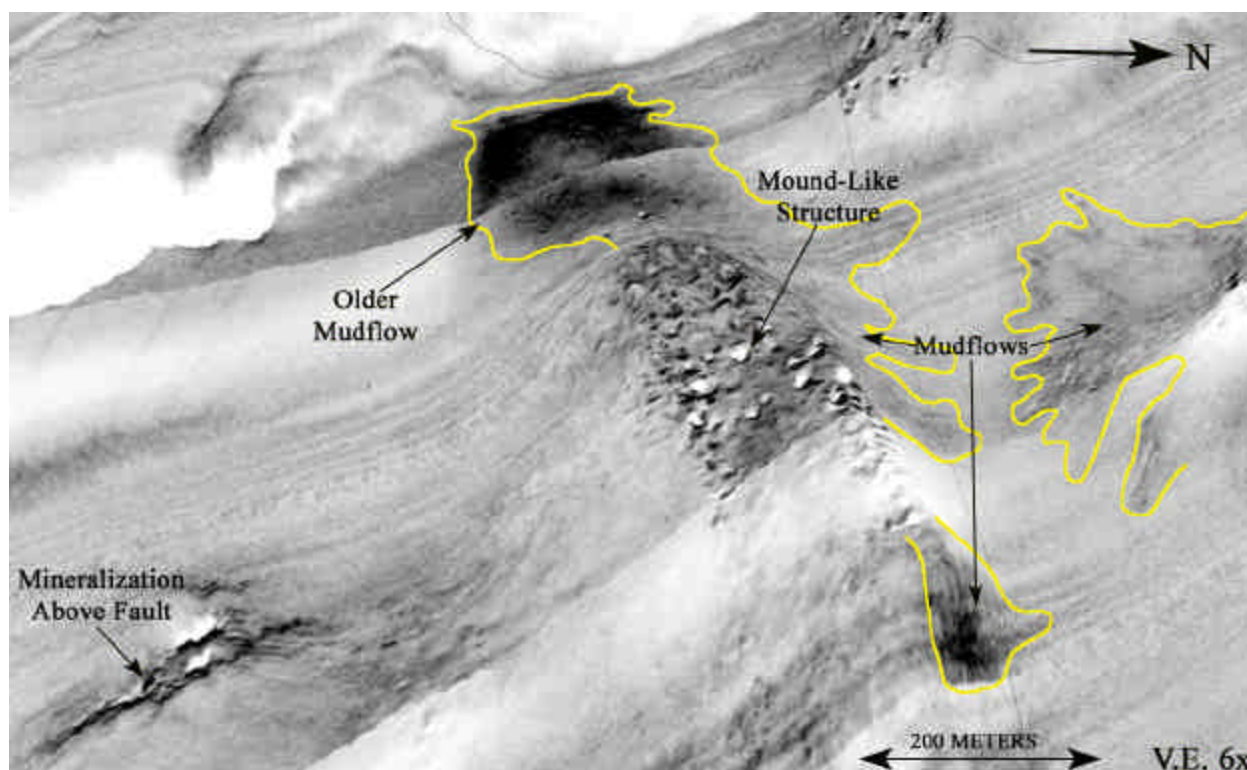


Figure 4.12 Digital terrain map of a draped side-scan sonar mosaic illustrating a large mound-like structure, mineralization above a fault and several extruded mudflows from the study area. Note the flat plateau-like top of the mound with rugose carbonate filled vents.

The mound-like structures in the study area are large features showing no preferable orientation and measuring between 4.5 m to 25 m (15 ft and 81 ft) in relief, with lengths between 168 m to 640 m (550 ft and 2,100 ft). Each of these features exhibit a topographically flat

plateau-like top (Fig. 4.12) with an array of rugose pockmark-like vents containing precipitated hardground material (authigenic carbonates). The flanks and near periphery of mound-like structures are surrounded by mudflows indicating a discharge of muddy sediments is occurring. Subbottom profiles (Fig. 4.4) show internal hard reflectors within the acoustic wipe-out zones suggesting relict authigenic carbonate occurs within the mound. This and the discharge of the mudflows suggest vertical growth by slow accretion of muddy sediments and authigenic carbonate.

Mineralized hardgrounds above faults occur in areas where faults rise to the seafloor and hardgrounds (authigenic carbonates) are precipitated within the linear depression created by faulting (Fig. 4.13). In the study area, these features show no preferable orientation, vary

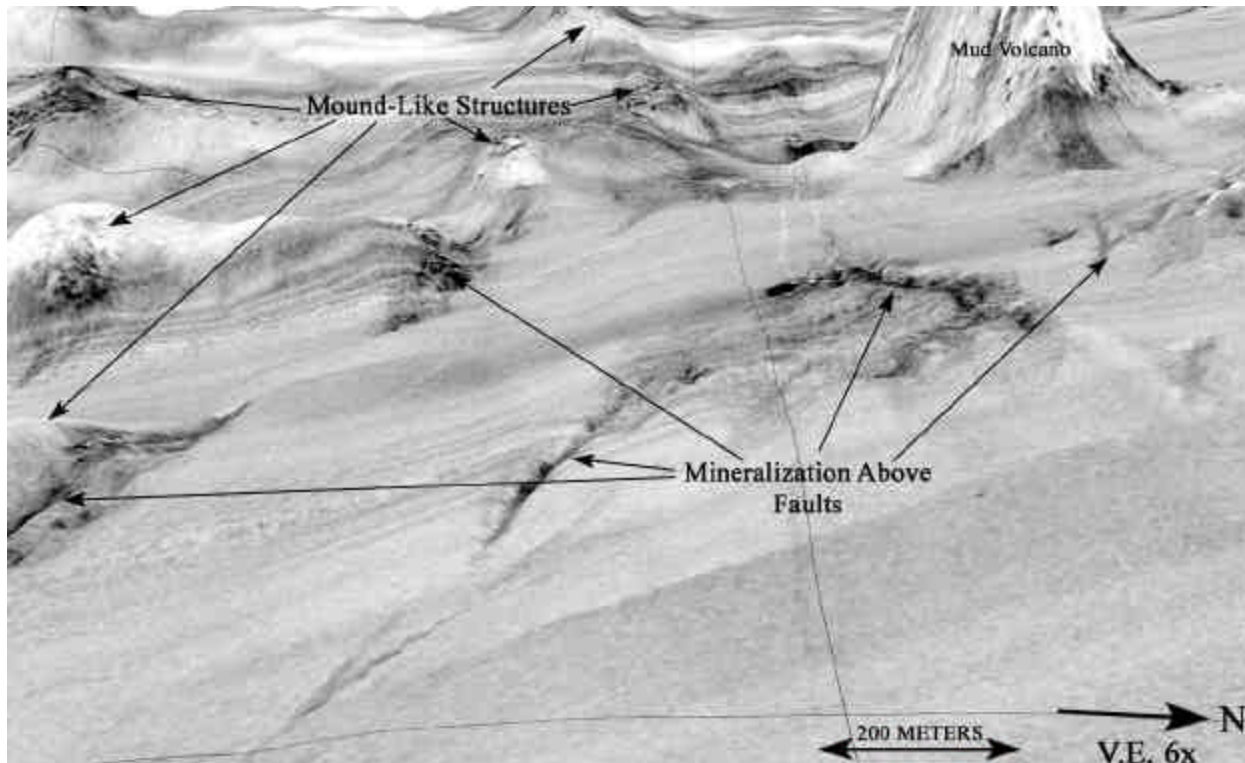


Figure 4.13 Digital terrain map of a draped side-scan sonar mosaic illustrating several areas of mineralization above faults, with mound-like structures and a mud volcano in the background. Note that the areas of mineralization above faults occur on the periphery, east of the mound-like structures.

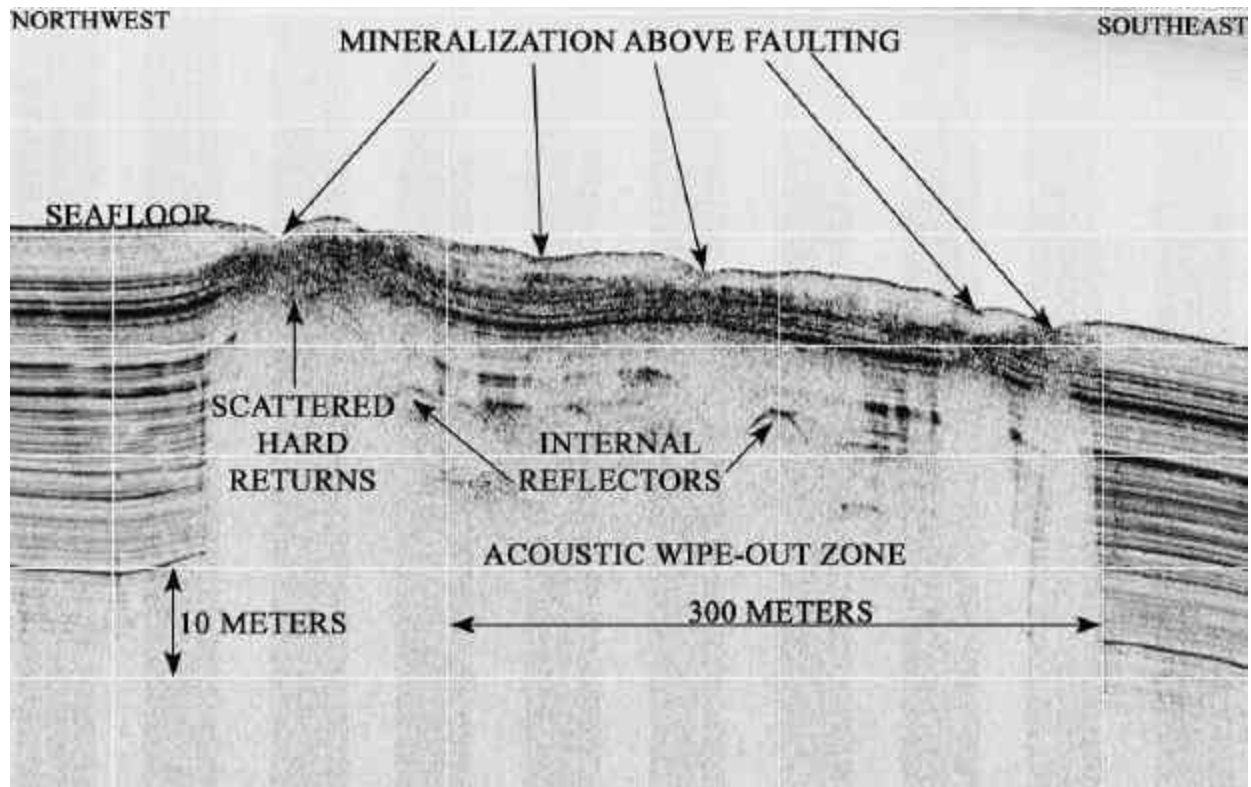


Figure 4.14 Subbottom profile record showing mineralization above faults in the study area. Note the scattered hard returns occurring below the seafloor within the acoustic wipe-out zone.

between 75 m to 275 m (250 ft and 900 ft) in length and are 0.5 m to 3 m (2 ft to 10 ft) deep. Authigenic carbonates found within the depression are generally thin, showing between 0.3 m and 1 m (1 ft and 3 ft) of thickness at the surface. Subbottom profiles in the study area show dark scattered hard returns below the seafloor within the acoustic wipe-out zone (Fig. 4.14). This may indicate that the formation of authigenic carbonate is taking place within the sediment. The mineralization above faults are generally not associated with large amounts of extrusive mud (mudflows). They are also situated some distance away from the massive fault system beyond the outer periphery of the mound-like structures. The absence of large amounts of extrusive mud, and the fact that these features are located some distance from the massive fault system, may indicate these features are too far away from the source to receive substantial geo-pressured

forces and therefore cannot entrain sediments. They are, therefore, interpreted as seeps that grow from the cementation of sediments and deposition of authigenic carbonates.

4.7 Mudflows

Mudflows are fine-grained fluidized sediments that have been extruded from a vent which frequently is a mound-like structure, mud volcano or mud vent (Fig. 4.7, 4.10, and 4.12). The size of mudflows is known to vary between large regional extrusions, which cascade down steep slopes for kilometers to small-localized extrusions, which occupy the flanks and lower area around mud prone extrusive sites. The mudflows in the study area are the latter, small-localized features measuring 30 to 245 m (100 to 800 ft) in length and 10 to 200 m (35 to 650 ft) in width, which typically exhibit concentric fan-like patterns originating from a central vent or set of vents.

The mudflows in the study area exhibit varied reflective characteristics. Those with lower reflectivities, showing less contrast in the images, are interpreted to be younger, while higher reflectivities, and thus more contrast in the images, are interpreted to be older (Fig. 4.7, 4.10, and 4.12). Recent mudflows are believed to be less dense and therefore show lower reflectivity on side-scan sonar records. This is because they have been extruded as fluidized, gas-charged, and hydrocarbon-rich mud. Older mudflows are believed to show higher reflectivity on side-scan sonar records because they have been subjected to bioturbation of the hydrocarbon-rich muddy sediments by lucinid/vesycomiid clams (Sassen et al., 2003). These chemosynthetic organisms are epibenthic, living below the seafloor within the sediment of the mudflow with the aid of a breathing tube, and process the hydrocarbon-rich muds for food. When the muds are depleted of hydrocarbons, the organisms die littering the top of the mudflows with their disarticulated shells. The disarticulated shells become partially cemented with the

sediments creating a rugose surface at the seafloor. This rugose seafloor shows high backscatter reflectivity on side-scan sonar records.

Figure 4.15 is a subbottom profile example of one of the larger mudflows in the study area. Mudflows are generally too thin to be imaged on subbottom profiles, however, the high-resolution quality of the AUV data occasionally makes mudflow imaging possible. The mudflow in Figure 4.15 was transported to the northwest away from its extrusive source (mound-like structure) and now covers 241 m. Interestingly, this figure demonstrates that the viscosity of the mudflow is low enough for the fluidized mud to travel down the flank of the mound-like structure and up a portion of the flank of the next feature, where it is able to retain its position.

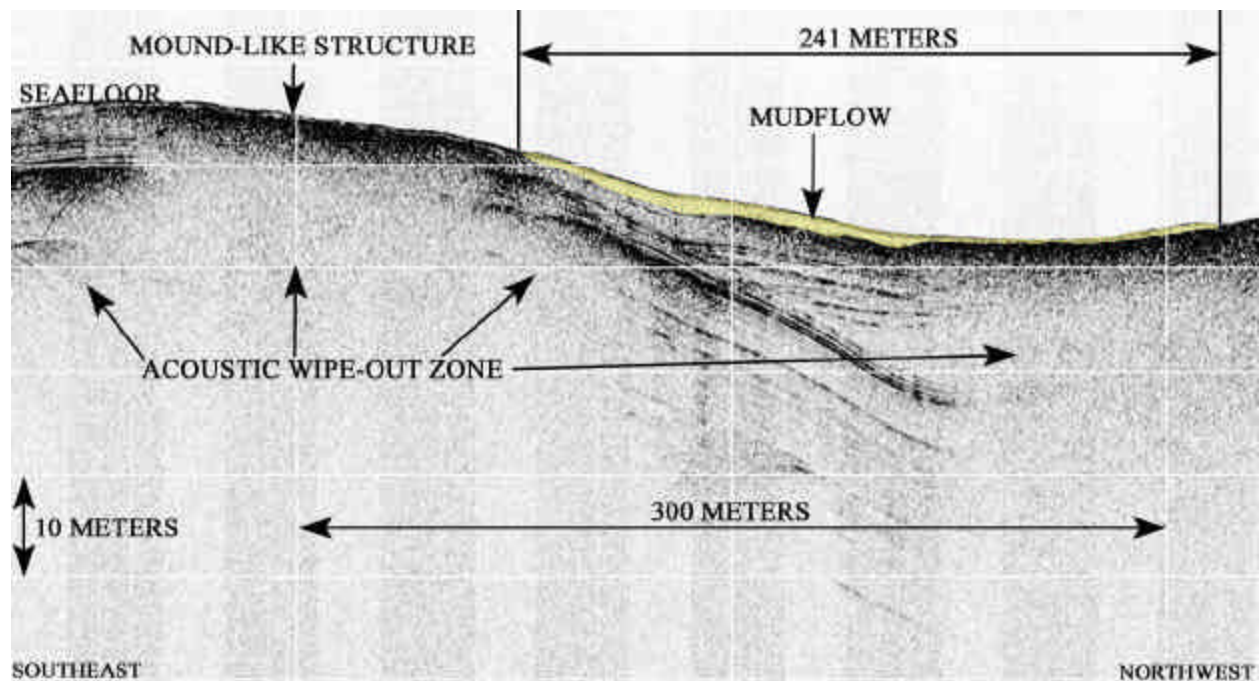


Figure 4.15 Subbottom profile record of a mudflow on the flank of a mound-like structure in the study area.

4.8 Slope Instability Features

Disturbed sediments due to slumping activity are seen throughout the survey area (Appendix A, Sheet 3). Slumps are sediment failures that often occur due to the oversteepening of a slope resulting from rapid sediment deposition or, as in this case, uplift (Roberts, 2001). While several episodes of localized episodic slumping have taken place, an episode of regional slumping appears to occur just below the third dark reflector at an approximate depth of 12 m (40 ft) below the seafloor over the entire study area (Fig. 4.16, Blue Slump). There is no record of slumping below this ~12 m seafloor interval. A large regional slump, trending northwest to southeast, is recorded paralleling the uplifted wedge on the up-thrown side of the massive fault system (Appendix A, Sheet 3). The direction of the slumping along this feature is toward the southwest, away from the uplift. The culmination of all these facts suggests that the slumping recorded just below the third dark reflector (~12 m below the seafloor) may indicate the onset of uplift and faulting within the survey area.

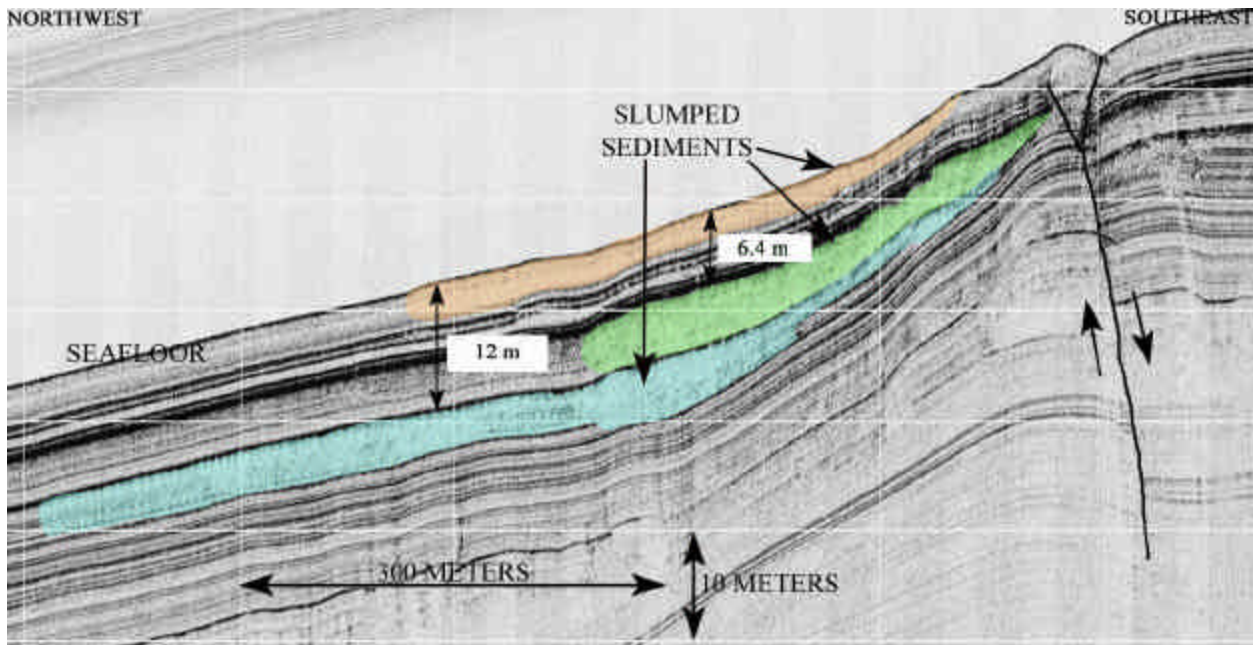


Figure 4.16 Subbottom profile illustrating three generations of slumping. The blue slump is believed to be a part of a regional slumping episode instigated by initial uplift.

4.9 Erosional Gullies

Erosional gullies were recorded in the central eastern, southern central western portions of the study area (Fig. 4.1). Gullies are distinct, short, narrow channels that often occur semi-parallel or contiguous to each other at the extremes of an uplifted formation (Fig. 4.17). The gullies are believed to be eroded by bottom currents, that travel along the ocean floor. The gullies in the study area vary in length between 250 m and 1,830 m (800 ft and 6,000 ft), in width between 30 m and 90 m (100 ft and 300 ft), and in depth between 0.3 m and 1.8 m (1 ft and 6 ft). They tend to be long and moderately wide but not very deep.

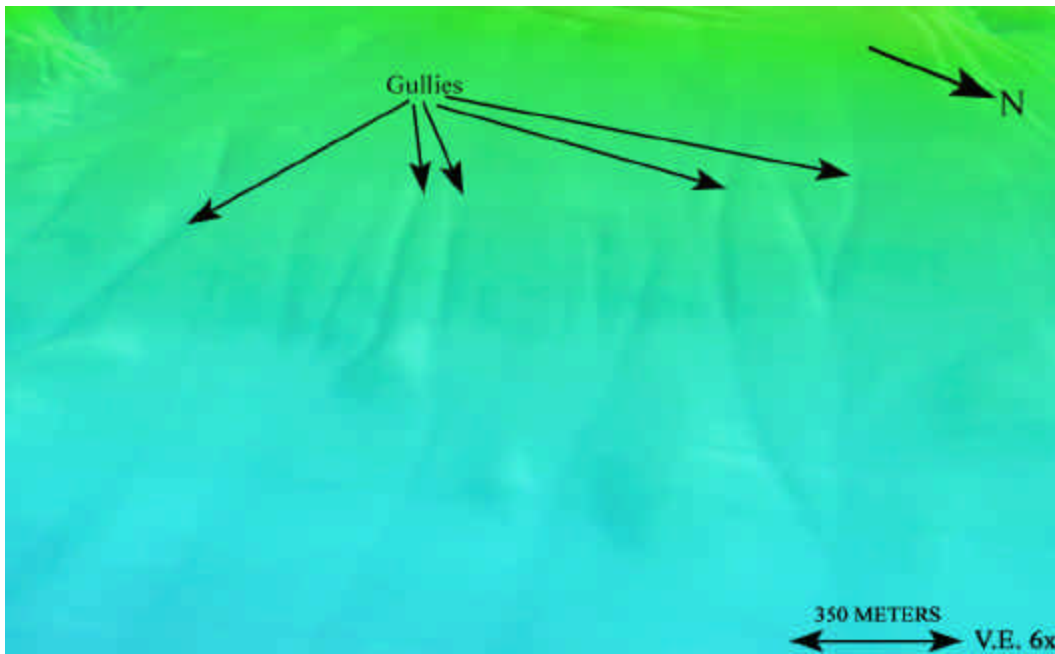


Figure 4.17 A DTM of multibeam data illustrating gullies on the slope in the central eastern portion of the study area.

The gullies in the study area seem to congregate at the outer extremes of the uplifted formation (Fig. 4.1; Appendix A, Sheet 1). Measurements indicate that at the outer extremes of the study area the seafloor transitions from an average 0.8° to 1.2° gradient to local gradients between 1.3° and 2.5° creating a lip or outer rim to the uplift (Fig. 4.18). The gullies appear to end where the rim transitions into a basin and resumes a gradient of less than 1.3° .

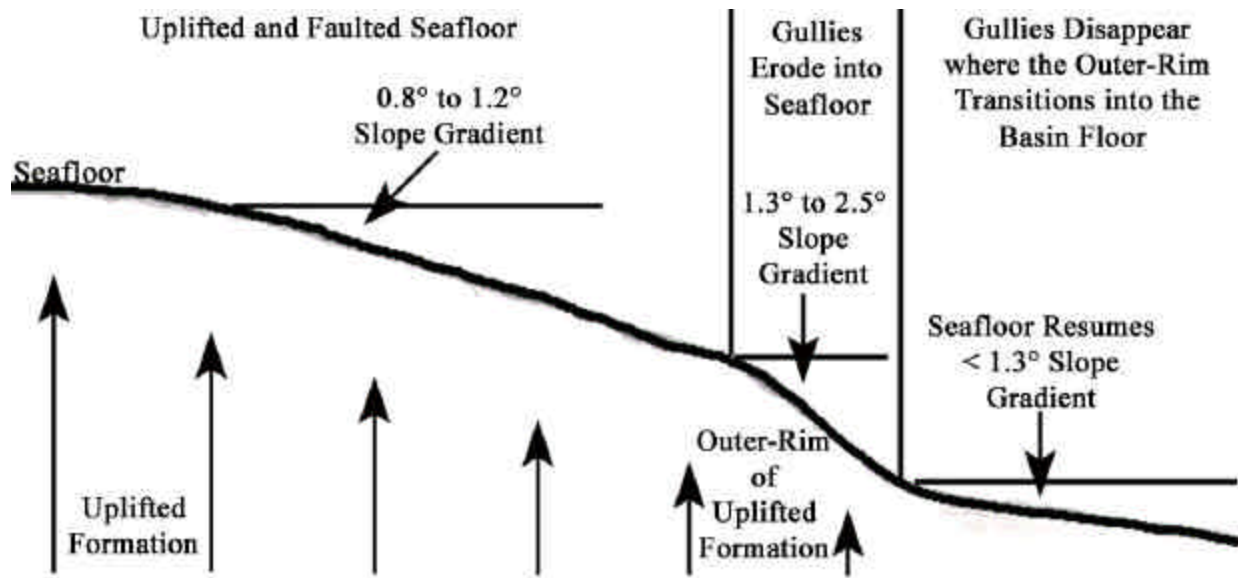


Figure 4.18 Schematic diagram illustrating the outer-rim location and gradient change where gullies erode into the seafloor in the study area.

Subbottom profiles across gullies in the study area show what appears to be a subsurface phenomenon occurring below gully features. Figure 4.19 exhibits that these phenomena occur directly below the gullies close to the seafloor and become offset toward the center of the figure as depth increases. Two interpretations are suggested for the formation of this phenomenon.

The first is that the subsurface phenomenon may be induced by the repeated expulsion of near seafloor biogenic gas. The expulsion may disturb and weaken the seafloor at the site of the expulsion-allowing bottom flowing currents to preferentially erode this sediment. The phenomenon below the seafloor is believed to be relict gullies preserved in the sedimentary record as the section accumulates over time (Roberts, Bouma, and Wrenn, personal communication, 2004).

While the interpretation above is likely and may indeed be happening, it does not take into account why the preferential expulsion of gas was occurring along the longitudinal distance exhibited by gullies in the first place. Additionally, the phenomena below the seafloor do not show the expected gully depression shape. Instead, the sediment below the seafloor appears to

be deformed and somewhat chaotic. Hypothetically bottom currents, according to the first interpretation, should have preferentially removed these deformed sediments. Interestingly, the bulk of the presumed chaotic sediments occur at and below the same ~12 m interval (reflector) at which the majority of slumping was interpreted in the section above (4.8 Slope Instability Features). An obvious transition in the character of phenomena occurs above the ~12 m interval.

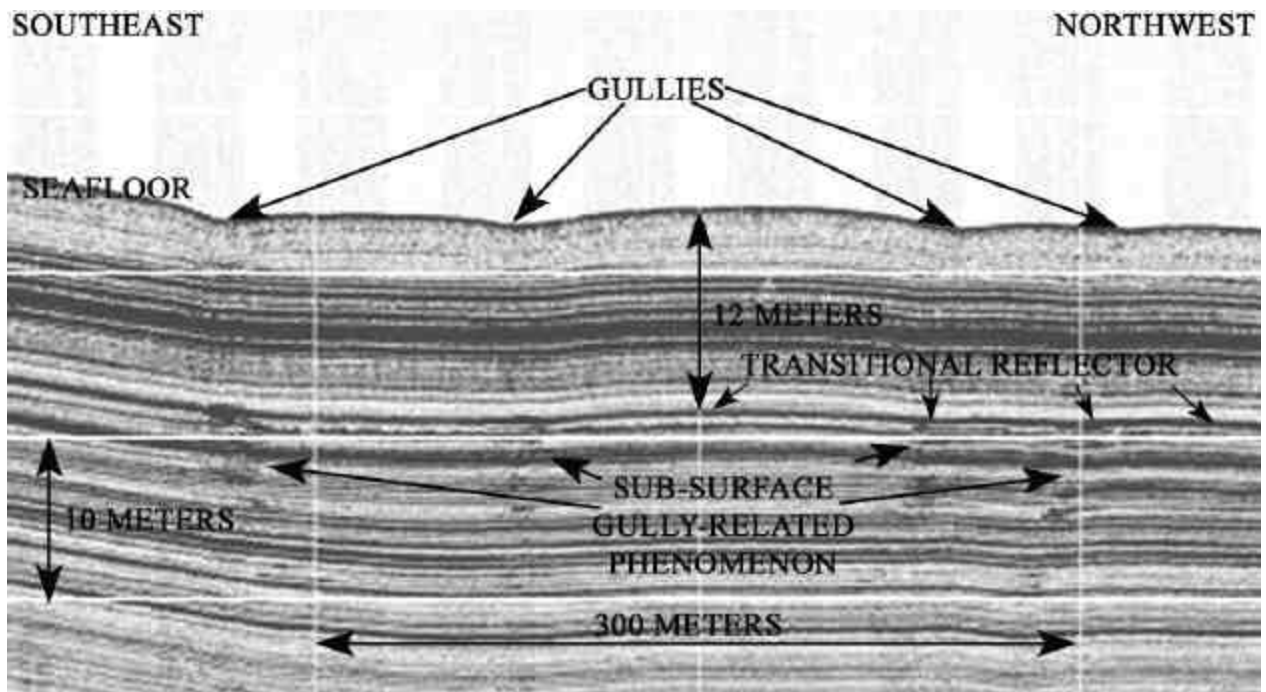


Figure 4.19 Subbottom profile record illustrating a sub-surface phenomenon found below gullies on the slope in the central eastern portion of the study area.

The second interpretation (below) for the formation of the subsurface phenomenon below gullies is based on the presumed deformation occurring at and below the ~12 m interval (reflector). Below this reflector the deformation is reminiscent of the shape demonstrated by graben faulting (Fig. 4.19). While no offset of the strata is evident, a close examination indicates some plastic thinning and bending of strata seems to have taken place. This interpretation leads to a hypothesis that the soft sediment deformation seen below gullies may be caused by

concentric extension occurring at the base or rim of an uplifted formation (Vendeville et al., 2003). The concentric extension is interpreted to be large enough of a force to cause deformation within the near seafloor soft sediments, but not large enough to initiate faulting. This same extension may be transmitted to the soft sediments of the seafloor causing minor depressions, which are later eroded into gullies by bottom currents.

CHAPTER 5. DESCRIPTION AND INTERPRETATION OF 3D SEISMIC DATA SET

5.1 Map Discussion

The water bottom amplitude extraction map (Appendix B, Sheet 1), water bottom dip map (Appendix B, Sheet 2), and several 3D seismic profile images, were provided by ENI Petroleum and Western Geco of Houston, Texas, to facilitate the 3D seismic interpretation.

The water bottom amplitude extraction map (Appendix B, Sheet 1) shows that the higher positive amplitude areas (red and orange) are located at sites of the extrusive features (mud volcano, mud vents, mound-like structures, and areas of mineralization above faults). The median amplitudes (white to yellow) surround the hardground features, whose distribution is very similar to that of the mudflows mapped using side-scan sonar data on the overview interpretation map (Appendix A, Sheet 3). The median amplitudes are interpreted as mudflows. Figures 5.1 and 5.2 are annotated images that outline the same key seafloor features (mud volcano, mud vents, hardgrounds, and mud flows) discussed in Chapter 4. Seismic transect lines, in red, cross the same key features from Chapter 4 and indicate the positions of seismic profiles provided by ENI Petroleum.

A gray scale, provided on the water bottom dip map (Appendix B, Sheet 2), indicates the changes in slope across the study area. Higher slopes are indicated by progressively darker shades of gray on the map. The major faulting, mud volcano, mud vents, and slopes of mound-like structures exhibit the higher angle slopes in the surveyed area. Three seismic transect lines (in red), indicate the positions of seismic profiles provided by ENI Petroleum, which cross the gully features.

The acoustic amplitude scales provided for the seismic profiles (transects) in this chapter (A-A' through I-I') are different from those provided for the water bottom extraction map. The

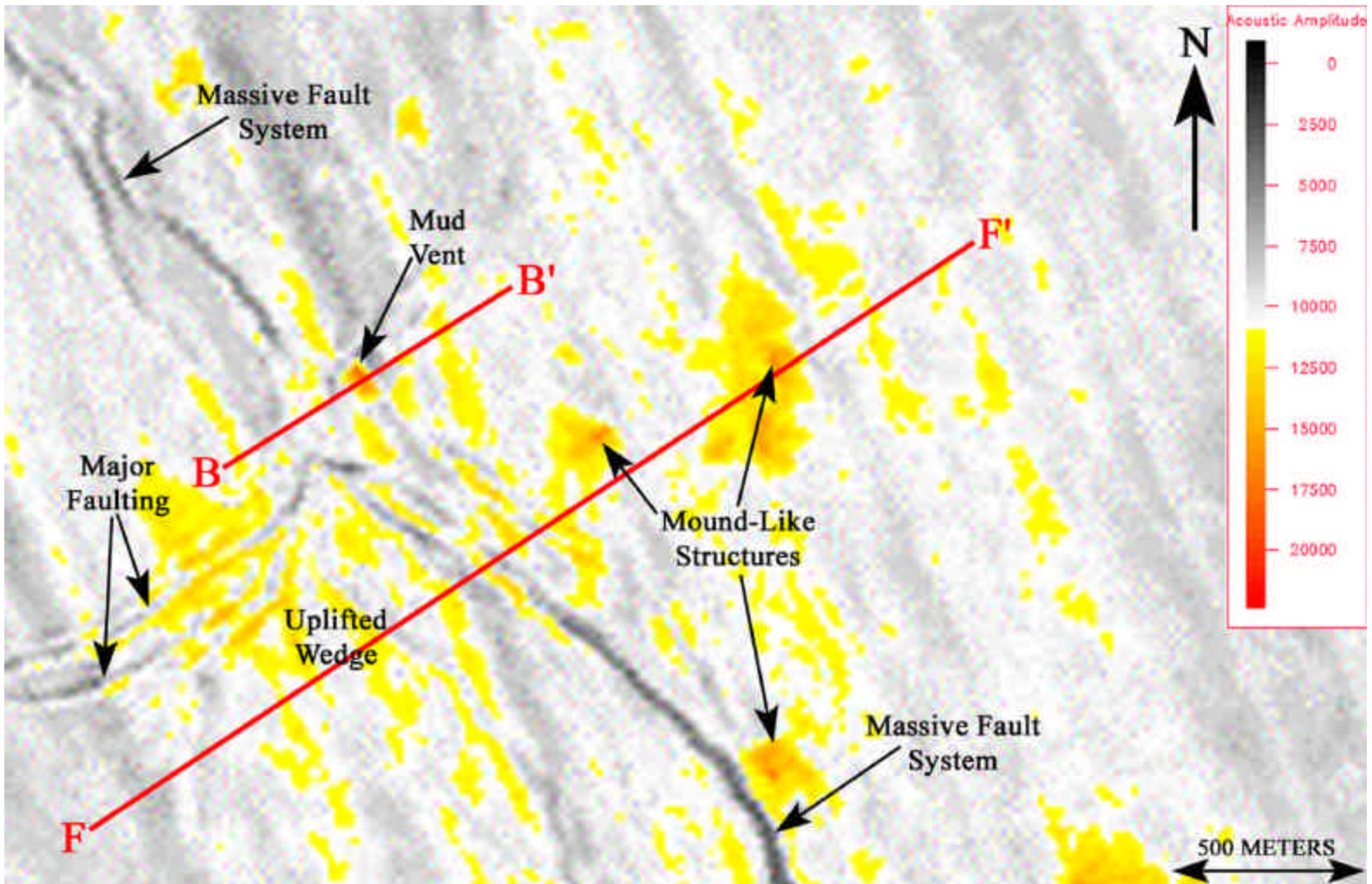


Figure 5.1 Water bottom amplitude extraction from the northern portion of the study area, illustrating the positions of 3D arbitrary seismic profiles (in red) across the uplifted wedge, mound-like structures, and a mud vent. Higher amplitudes (red) are evident in the locations of the mound-like structures and the mud vent. Median amplitudes (yellow) are indicative of mudflows surrounding the higher amplitude features. Redrafted from a water bottom amplitude extraction map provided by ENI Petroleum (Appendix B, Sheet 1).

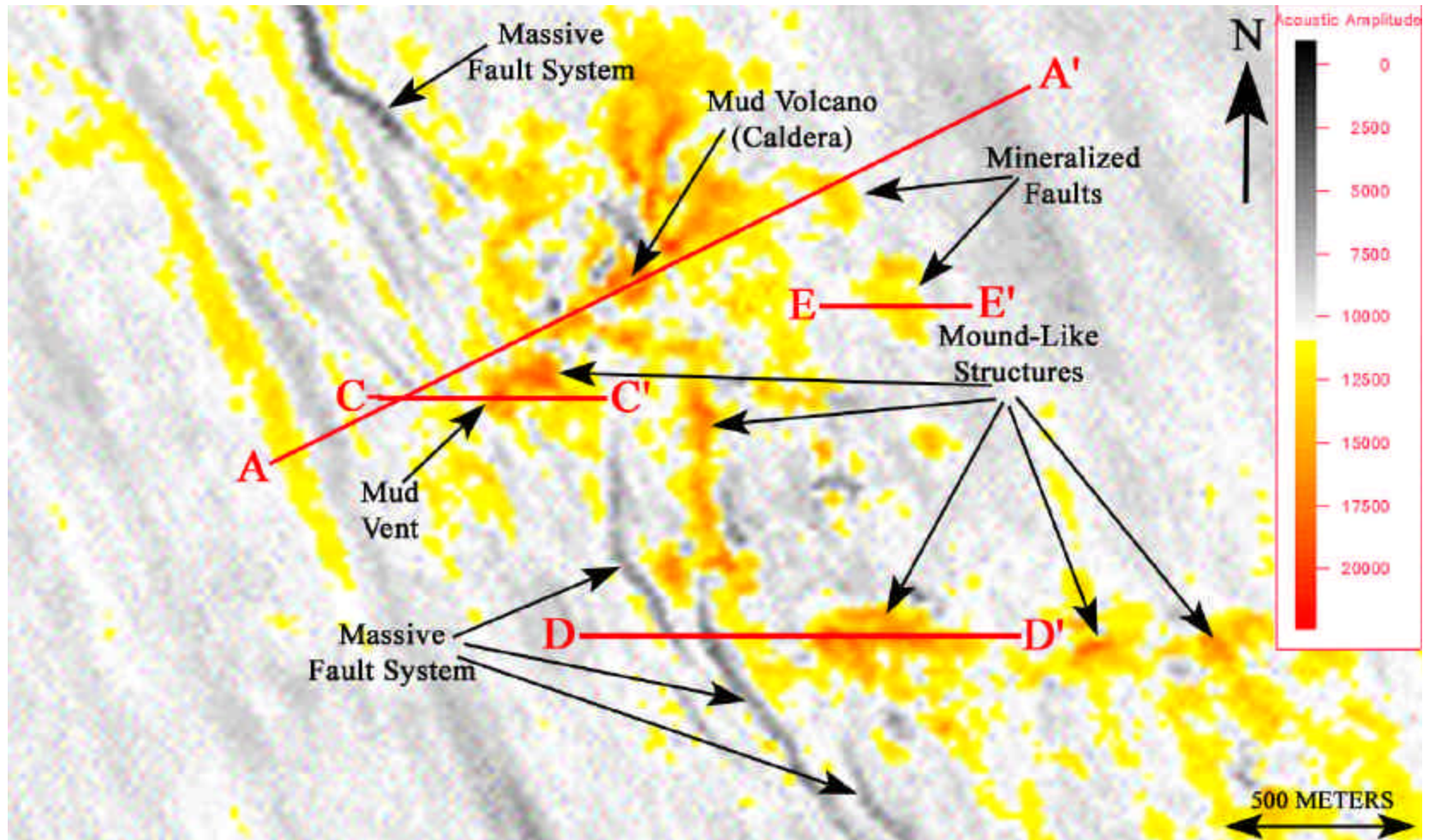


Figure 5.2 Water bottom amplitude extraction from the central portion of the study area, illustrating the positions of 3D arbitrary seismic profiles (in red) across the mud volcano, a mound-like structure, a mud vent, mineralization above a fault, and the mud vent. Median amplitudes (yellow) are indicative of mudflows surrounding the higher amplitude features. Redrafted from a water bottom amplitude extraction map provided by ENI Petroleum (Appendix B, Sheet 1).

acoustic amplitude scales, provided for the seismic profiles, shows both negative and positive amplitude values (Fig. 5.3), while the water bottom extraction map acoustic amplitude scale only shows positive amplitude values (Figs. 5.1 and 5.2). Additionally, the seismic profile acoustic amplitude scales show higher negative values (troughs) in red, orange, and yellow, median negative and positive values in white, light gray, and dark gray, and higher positive values (peaks) in black. Using this scheme, denser features, such as hardgrounds, are not distinguishable from the peak seafloor return at the sediment water interface (dark black reflector at seafloor horizon; Fig. 5.3). Gas and fluid-rich sediments with lower densities, such as extruded mud, appear in red or yellow just below the seafloor horizon.

5.2 Mud Volcano

The mud volcano in the central portion of the downthrown block of the study area appears as a yellow circular interior surrounded by red on the water bottom amplitude extraction map (Fig. 5.2). The circular median positive amplitude (yellow) interior is interpreted as the crater. The surrounding high positive amplitude (red) is interpreted as the flanks of the mud volcano. The median positive amplitudes (yellow) indicate the sediments in the crater are less dense than those on the flanks of the feature, which suggests the material filling the crater of the mud volcano is perhaps still active with gas-charged sediments in the volcano throat. Higher amplitudes (red) are also evident on the periphery of the mud volcano and conform to the same seafloor locations of the authigenic carbonates, gas vents, and expulsion sites interpreted from side-scan sonar in Figure 4.7. Median positive (yellow) amplitudes surround the interpreted expulsion features showing very similar patterns to those of the interpreted mudflows in Figure 4.7.

Figure 5.3, a 3D seismic profile (A-A'), shows that a graben-faulted area and disturbed sediment occurs below the mud volcano. The graben faulting is apparent below the mud volcano but was not imaged by the high-resolution AUV data, however, its presence was implied by the morphology of the feature and thus interpreted (Section 4.4 Mud Volcano). The higher negative amplitude reflectors below the mud volcano may cause a slight velocity “pull down” effect, however, the clear faulting below and around the feature indicate a graben is in evidence. A velocity “pull down” effect is caused by a decrease in velocity of the seismic signal as it enters a gas-rich area. A high negative amplitude reflector (red) just below the seafloor, suggesting the presence of less dense gas and fluid-rich sediments, is evident starting at the crater and continuing down the eastern flank of the mud volcano. The presence of the higher amplitude

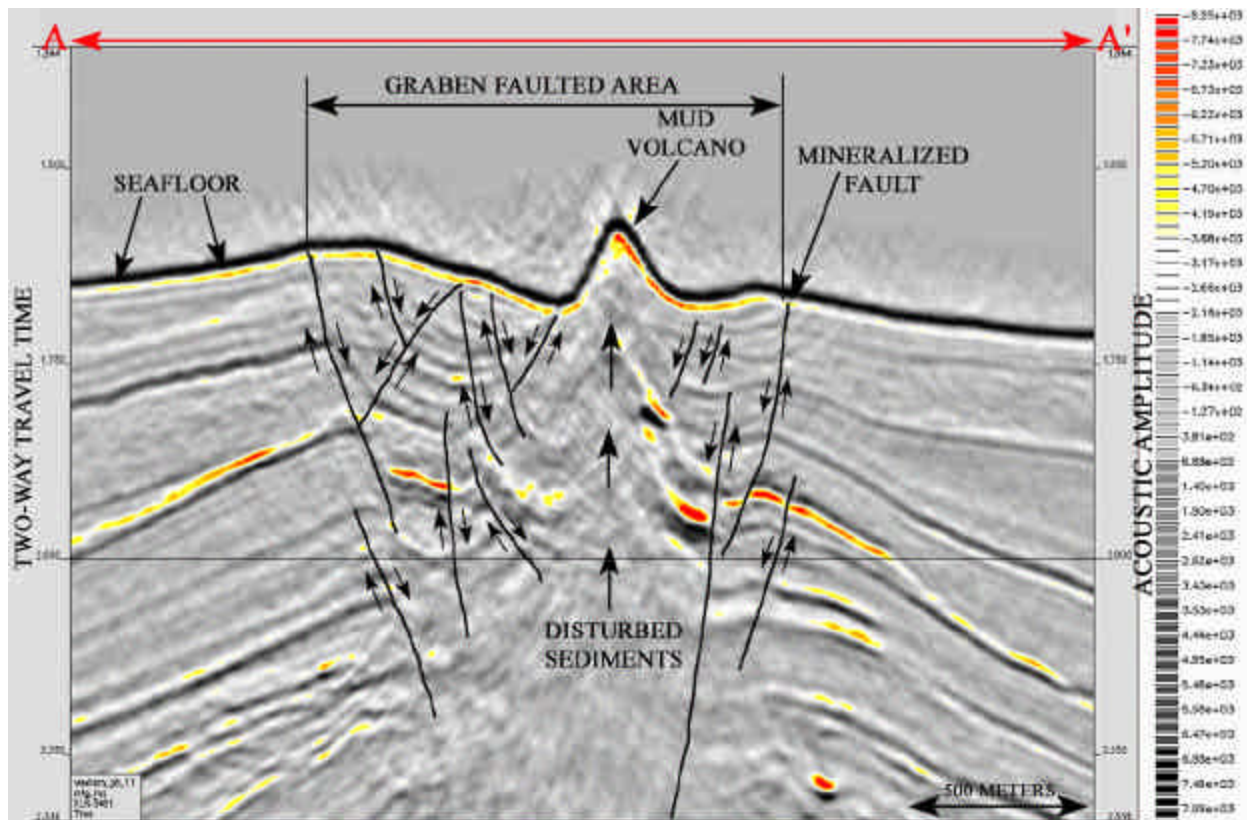


Figure 5.3 Three-dimensional seismic profile across the mud volcano in the study area. Note the graben faulting below the mud volcano. See Figure 5.2 for plan view position of seismic line (A to A'). Redrafted from an image provided by ENI Petroleum.

reflector correlates nicely with the more recent eroded gullies and mudflow extrusion interpreted on the eastern flank of the mud volcano in the high-resolution data (Fig. 4.7).

5.3 Mud Vents

Two features interpreted as mud vents in Chapter 4 (Figs. 4.9 and 4.10) occur along the massive fault system in the northern (Fig. 5.1) and central (Fig. 5.2) portions of the study area. Two seismic profiles, B to B' and C to C', transect these mud vent features and are presented in Figures 5.4 and 5.5.

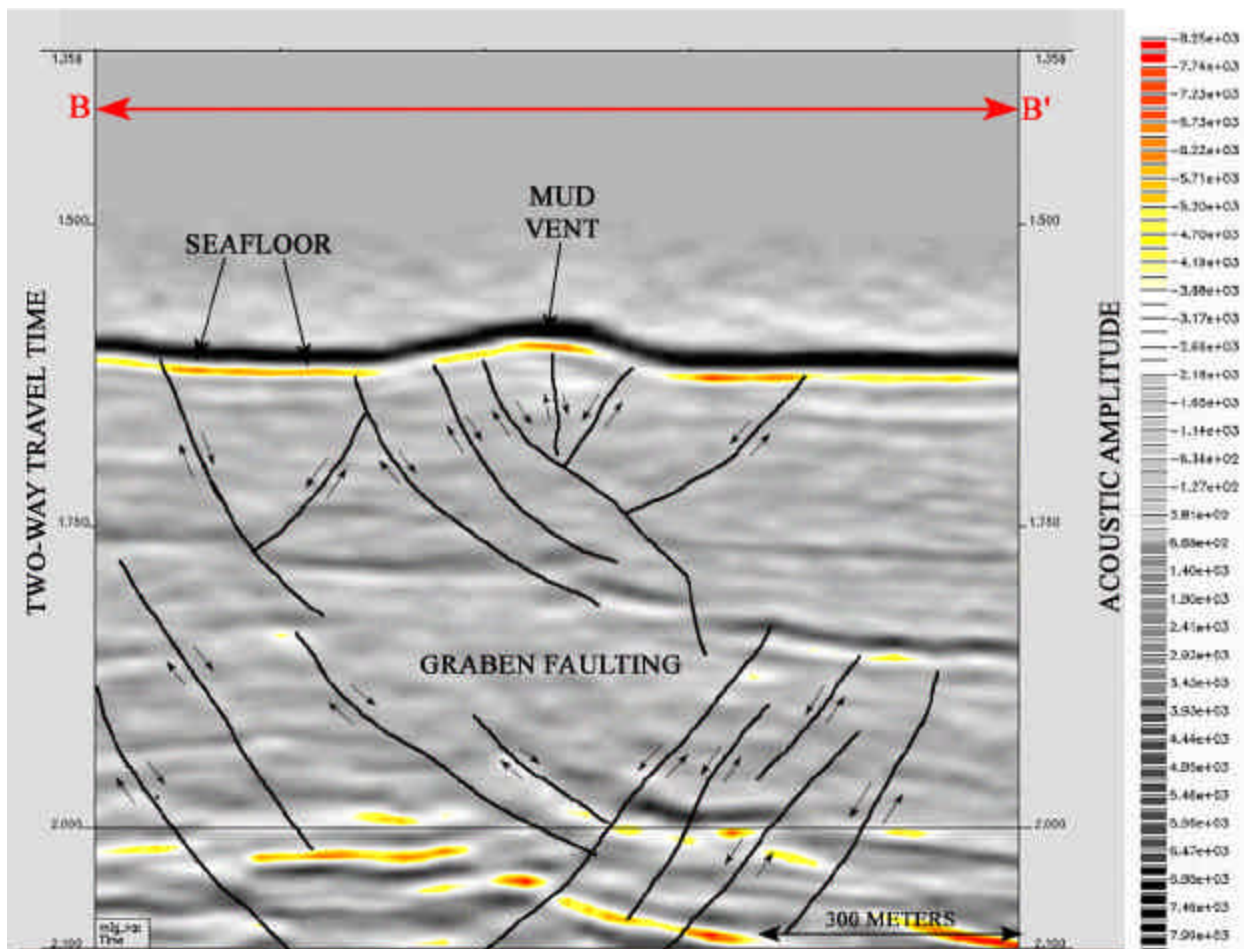


Figure 5.4 Three-dimensional seismic profile across the mud vent in the northern portion of the study area. Note the graben faulting below the mud vent that appears to be the conduit for expulsion. See Figure 5.1 for plan view position of seismic line (B to B'). Redrafted from an image provided by ENI Petroleum.

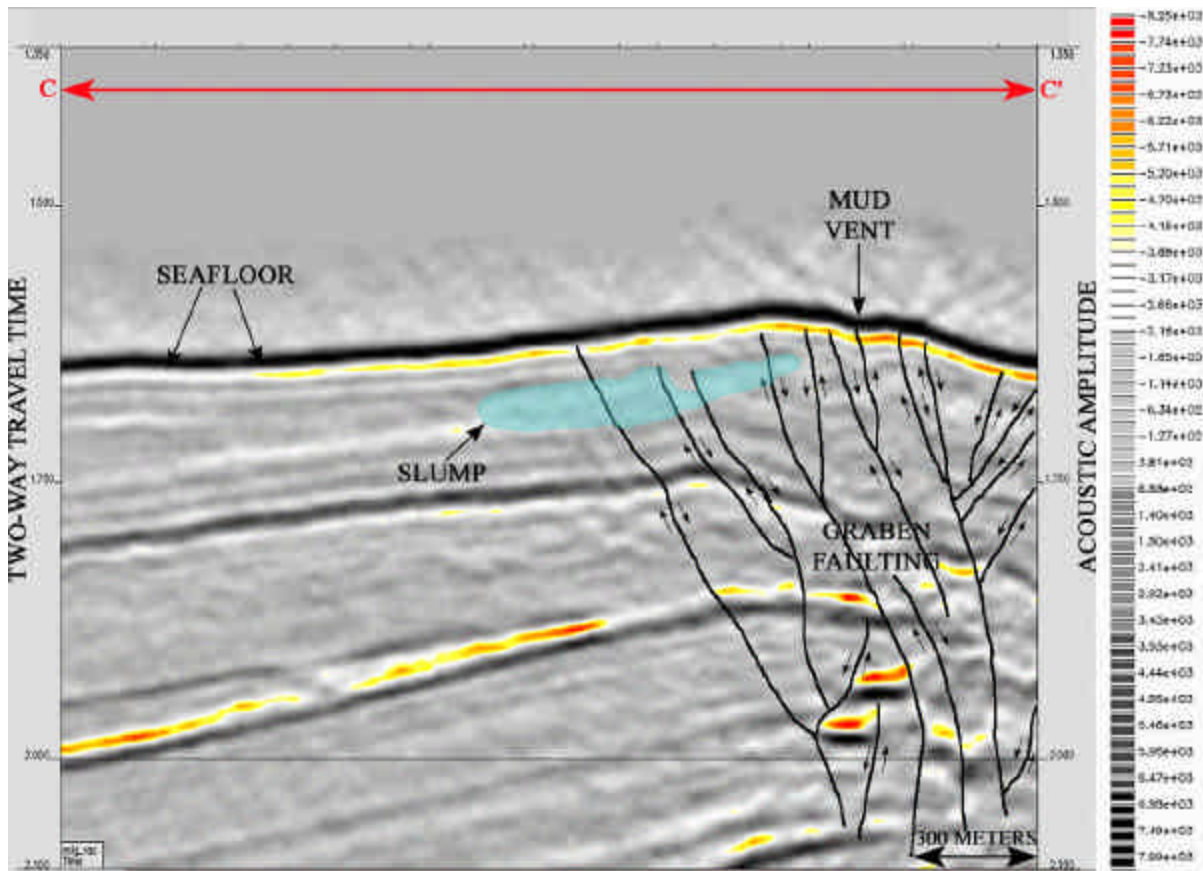


Figure 5.5 Three-dimensional seismic profile across the mud vent in the central portion of the study area. Note the graben faulting below the mud vent that appears to be the conduit for expulsion. A slump is also interpreted 12 m below the seafloor. See Figure 5.2 for plan view position of seismic line (C to C'). Redrafted from an image provided by ENI Petroleum.

In the plan view (Figs. 5.1 and 5.2) the mud vents both show higher positive amplitudes (red) in the central interpreted crater and cone area, suggesting that lithified sediments or a collection of shells are present. The presence of this interpreted hardground surface suggests these features are probably largely dormant or episodically active. Median positive amplitudes (yellow), interpreted as mud flows, appear to the northwest and southeast of the mud vent in the central portion of the study area (Fig 5.2). The patterns of these mudflows precisely emulate the patterns of mudflows interpreted from the same vent in Figure 4.10.

In the seismic profiles (Figs. 5.4 and 5.5) graben faulting is evident below each of the mud vents, implying these faults act as the conduit for expulsion. A high negative amplitude reflector (red) is evident just below the seafloor. The presence of the higher negative amplitudes below the mud vents indicates that potential gas and fluid-rich sediment occur just below the seafloor. If higher negative amplitudes were not evident below the mud vents, these features would be interpreted to be dormant. However, higher negative amplitudes do occur below the mud vent features suggesting they are episodically active rapid vent sites and/or sites of seepage. This interpretation is precisely the conclusion reached after examination of the high-resolution data in Chapter 4.

5.4 Hardground Features

Two types of hardgrounds, mound-like structures and mineralization along surface faults, are interpreted in Figures 4.12 and 4.13. These features occur in the central portion of survey area east of the massive fault system (Fig. 5.2). In the study area, the interpreted hard seafloor areas along faults are generally situated east of the mound-like structures. A seismic profile, D to D', that transects the mound-like structure imaged in Figure 4.12 is presented in Figure 5.6. A second seismic profile, E to E', that transects an area of mineralization above a fault imaged in Figure 4.13 is presented in Figure 5.7.

In the plan view (Fig. 5.2), the top of mound-like structure shows higher positive amplitudes (red), while the flanks of the mound show median to high positive amplitudes (white, yellow, and orange). The higher amplitudes evident on the top of the feature are interpreted as an array of rugose authigenic carbonate filled vents exhibited in Figure 4.12 (MacDonald et al., 1990). The median to high positive amplitudes, evident on the flank and at the base of the feature, show very similar patterns to the mudflows interpreted in Figure 4.12.

The plan view (Fig 5.2) at the location of the seafloor mineralization shows high to medium positive amplitudes (orange to yellow). The higher amplitudes (orange) appear centrally located at the locus of the faulting. The pattern exhibited by the amplitudes on the plan view appears identical to that of the mineralized seafloor feature shown in the foreground of Figure 4.13.

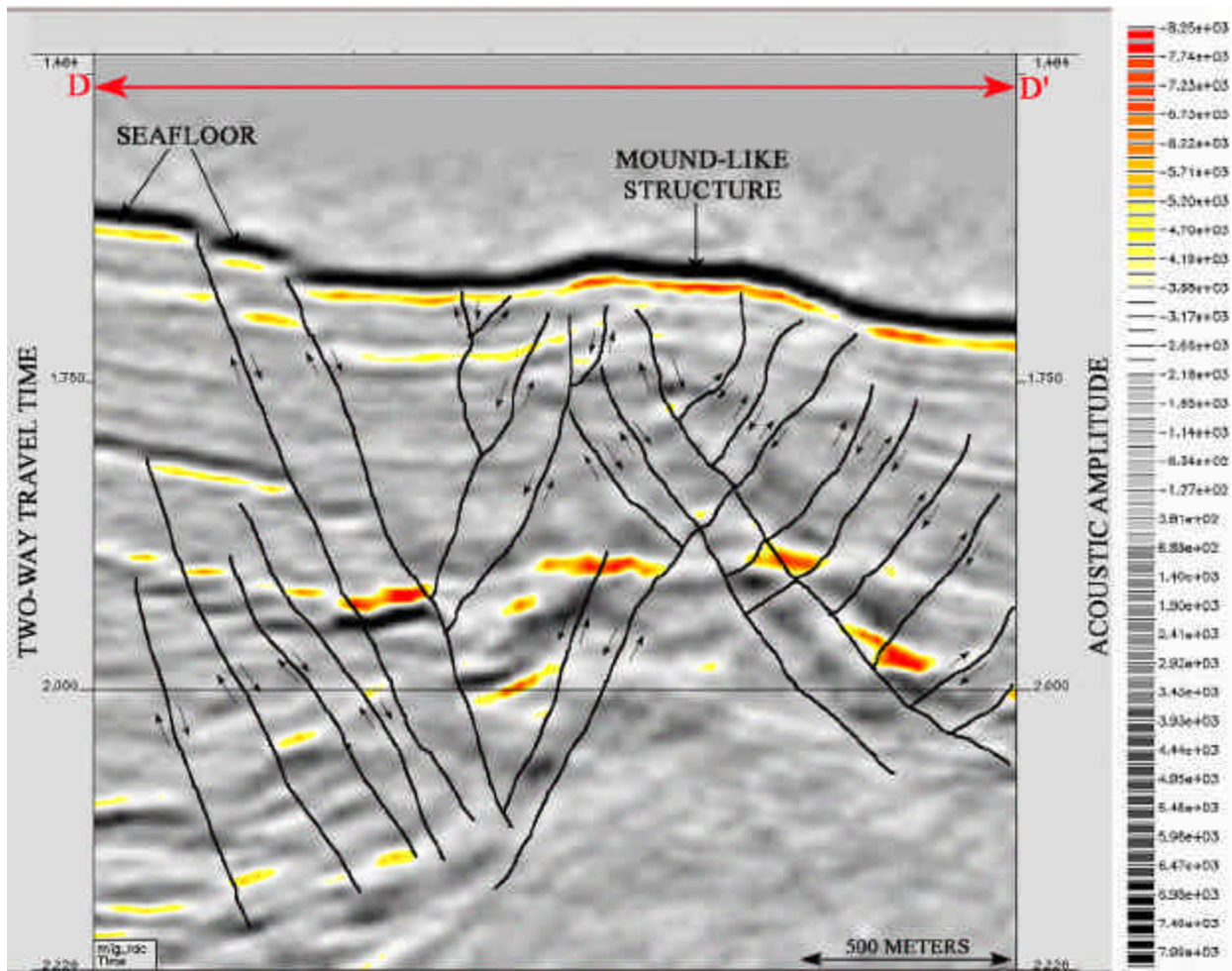


Figure 5.6 Three-dimensional seismic profile across a mound-like structure in the central portion of the study area. Note the graben faulting below mound that appears to be the conduit for seepage. See Figure 5.2 for plan view position of seismic line (D to D'). Redrafted from an image provided by ENI Petroleum.

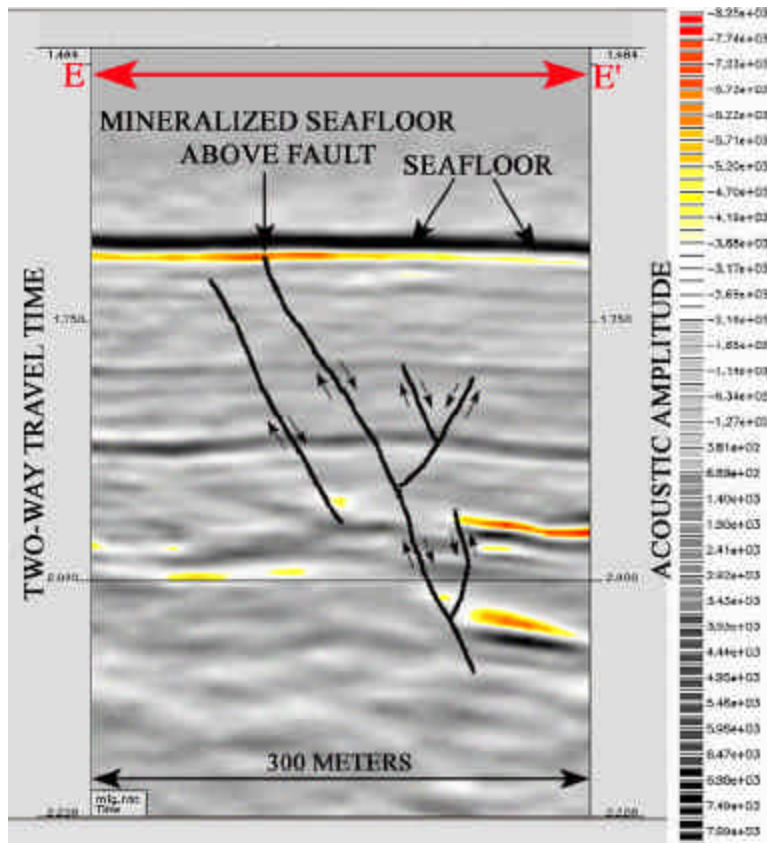


Figure 5.7 Three-dimensional seismic profile across a mineralized area of the seafloor above a fault in the central portion of the study area. Note the lack of the network of faults that are apparent below the mound-like structure in Figure 5.6. See Figure 5.2 for plan view position of seismic line (E to E'). Redrafted from an image provided by ENI Petroleum.

The seismic profiles that transect the mound-like structure and the seafloor mineralization (Figs. 5.6 and 5.7) both show high negative amplitudes (red) just below the seafloor, which indicate the presence of less bubble phase gas and perhaps fluid-rich sediments. However, a distinct difference is noticeable between the quantities of faults below each of the features. The mound-like structure (Fig. 5.6) exhibits a complex network of numerous normal faults which act as conduits to the seafloor, while the seafloor mineralization (Fig. 5.7) only appears to have one major fault that acts as a conduit. The difference in the quantities of faults below these features adds credence to the interpretation from Chapter 4 that the areas of seafloor mineralization lie on

the outskirts of the uplifted feature some distance away from the massive fault system and therefore receive substantially less gas and fluid-rich sediments.

5.5 Mudflows

Owing to the lower resolution (14 m to 17 m tuning thickness) of 3D seismic data, the mudflows in the study area cannot be resolved in profile; however, they can be readily mapped on the water bottom amplitude extraction map, as has been suggested earlier in this chapter. The varied amplitudes interpreted surrounding extrusive features suggest mudflows of varied ages and densities exist within the study area. These same varied amplitudes are also seen as variable density mudflows in the high-resolution data set (Chapter 4, 4.7 Mudflows). In Figure 5.8 the varied amplitudes displayed by the mudflows have been mapped.

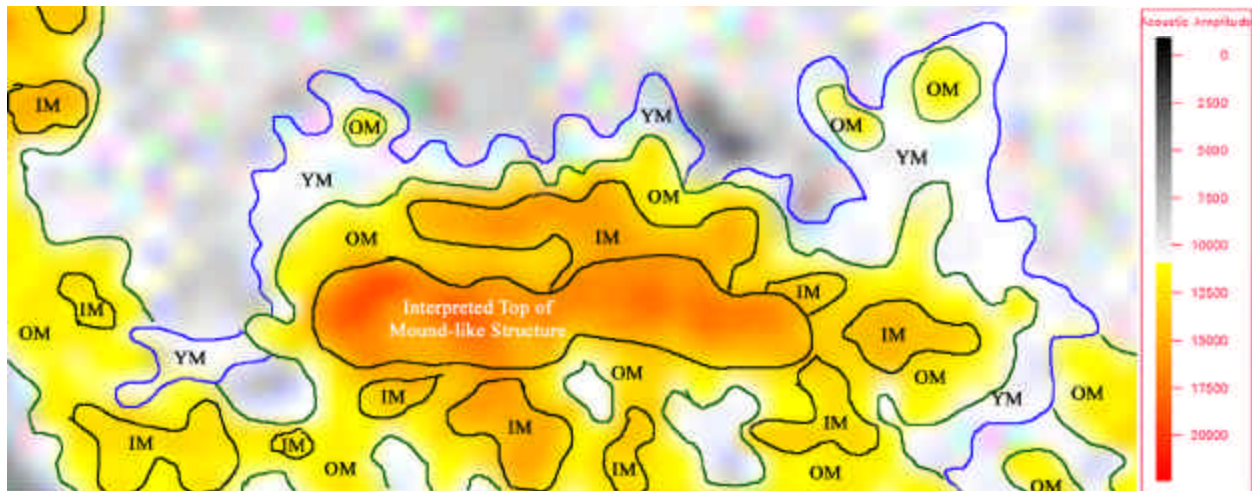


Figure 5.8 A zoomed in water bottom amplitude extraction, from the central portion of the study area, illustrating the mudflows surrounding a mound-like structure. Note that the varied amplitudes portrayed have been interpreted to indicate age and induration of the extruded sediment: IM for indurated mudflow (orange), OM for older mudflow (yellow), and YM for younger mudflow (white). Redrafted from a water bottom amplitude extraction map provided by ENI Petroleum (Appendix B, Sheet 1).

In the figure above (Fig. 5.8), high positive amplitudes (orange) are interpreted as older indurated mudflows that are partially cemented and covered with disarticulated shells of lucinid/vesycomyid clams (IM) (MacDonald et al., 1990). The median positive (yellow) amplitude mudflows are interpreted as older mudflows that may be partially cemented but do not have the rough layer of disarticulated shells (OM). The median positive (white) amplitude mudflows are interpreted as the youngest mudflows that may be rich in both hydrocarbon fluid and gas (YM). In Figure 5.8, the interpreted younger mudflows lie on the outer periphery, showing no transport pathways across the older mudflows, this may be because the transport pathways of the younger mudflows may be below the resolving ability of the 3D seismic. The patterns exhibited by the mudflows (Fig. 5.8) on the northeast and north flanks of the mound-like structure correlate well with those interpreted surrounding the same mound-like structure on the high-resolution data set (Fig. 4.12). However, the water bottom amplitude extraction image (Fig. 5.8) shows several other mudflows occurring on the southeast, southwest, and northwest flanks of the mound-like structure that were not visible on the side-scan sonar mosaic. The presence of the mudflows seen on the 3D water bottom amplitude extraction that were not seen on side-scan sonar may indicate that 3D seismic is the better tool with which to discriminate mudflows on the seafloor.

5.6 Slope Instability Features

A 3D seismic profile (F to F'), which extends from the west-southwest to the east-northeast across the crest of the uplifted wedge in the northern portion of the study area (Figs. 5.1 and 5.9), is provided to determine if the slumping recorded in the high-resolution survey was interpretable on 3D seismic (Fig. 5.9). The 3D seismic profile shows two generations of slumps on the southwest flank of the uplifted wedge. The younger slump (blue) is recorded ~12 m (~40

ft) below the seafloor and is the same feature interpreted from subbottom profiles in the high-resolution data set (Appendix A, Sheet 3). The older slump (green) is recorded at ~79 m (258 ft) below the seafloor, which was beyond the recording depth of the high-resolution AUV's subbottom profiler. The older slump is significant because it may indicate the initial uplift and onset of faulting in the study area. The presence of the older slump also negates the high-resolution data interpretation, which suggested that the initial onset of slumping may have

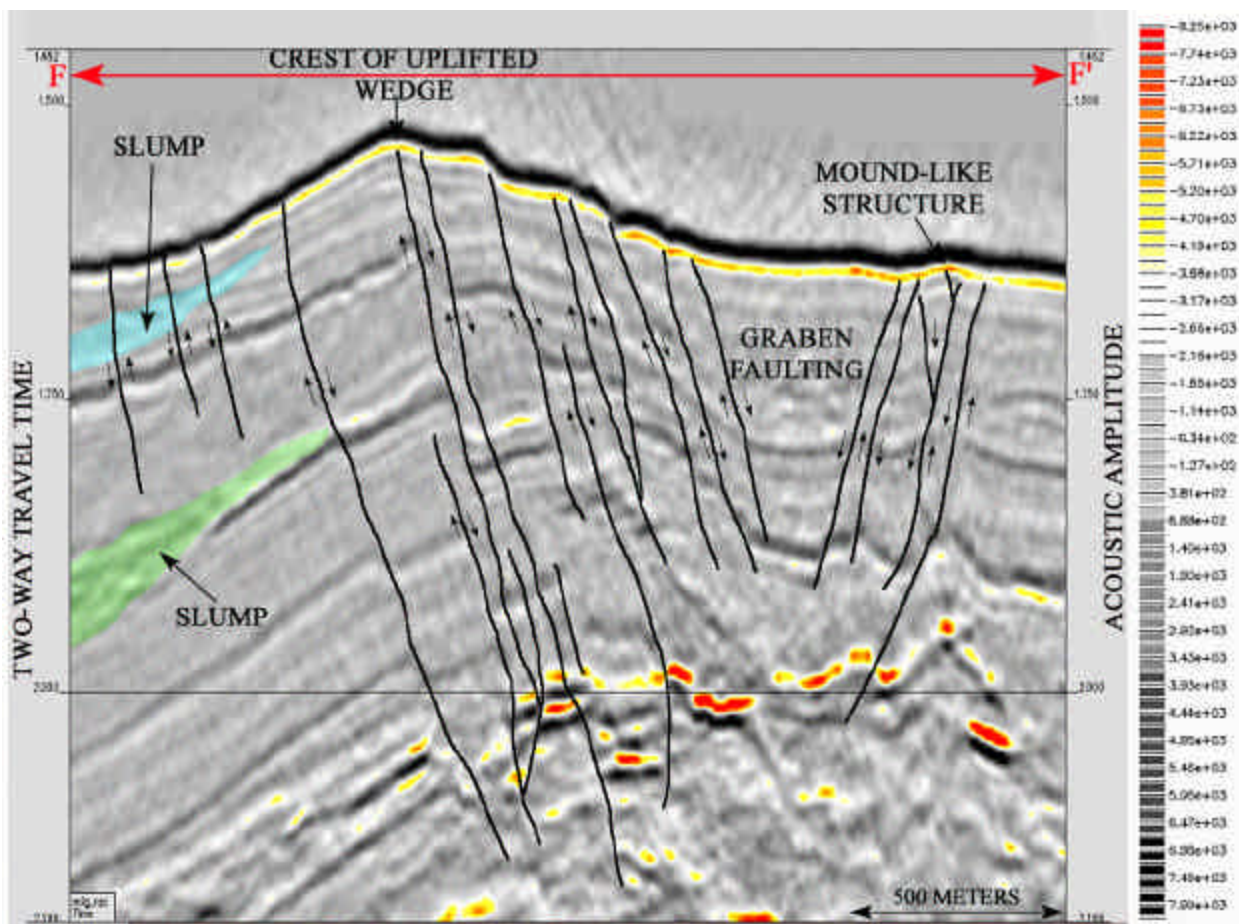


Figure 5.9 Three-dimensional seismic profile across the crest of the uplifted wedge in the northern portion of the study area illustrating two generations of slumping occurring on the upthrown block of the massive fault system. See Figure 5.1 for plan view position of seismic line (F to F'). Redrafted from an image provided by ENI Petroleum.

occurred at the ~12 m (40 ft) depth. The revised interpretation is that two episodic uplifts occurred, which upset unstable sediments on the southwest slope of the uplifted wedge initiating two generations of slumping.

5.7 Gullies

A plan view of the water bottom dip map (Fig. 5.10) and three seismic profiles (Figs. 5.11, 5.12, 5.13) are provided for 3D interpretation of the gullies in the central eastern and central western portions of the study area. The water bottom dip map (Appendix B, Sheet 2) and Figure 5.10 show the locations of the three seismic profiles (G-G', H-H', and I-I'). Figure 5.10 shows the location of the interpreted outer rim or lip of the uplift along the transect H to H'. However, the resolution of the 3D seismic was not high enough to record the gullies on the water bottom dip map, therefore the locations of the gullies are denoted by arrows in Figure 5.10.

The seismic profile in Figure 5.11 crosses the study area from southwest to northeast and shows the bounds of the deformation and faulting generated by uplift between the uplifted wedge crest and the interpreted outer rim or lip of the formation. The significance of this figure is that the eastern-most fault in the deformation occurs directly below the interpreted rim of the formation where the gullies occur. The fact that this fault does not reach the seafloor may indicate the sediments above this fault may still be experiencing stress. These facts add credence to the high-resolution data interpretation, which suggested that the outer rim feature was the eastern most limit of the deformation caused by the uplift.

The seismic profile H to H' in Figure 5.12 crosses the study area from northwest to southeast along the interpreted eastern outer rim, crossing the west to east trending gullies (Fig 5.10). At the seafloor very slight undulations mark the positions of the gullies. Higher negative

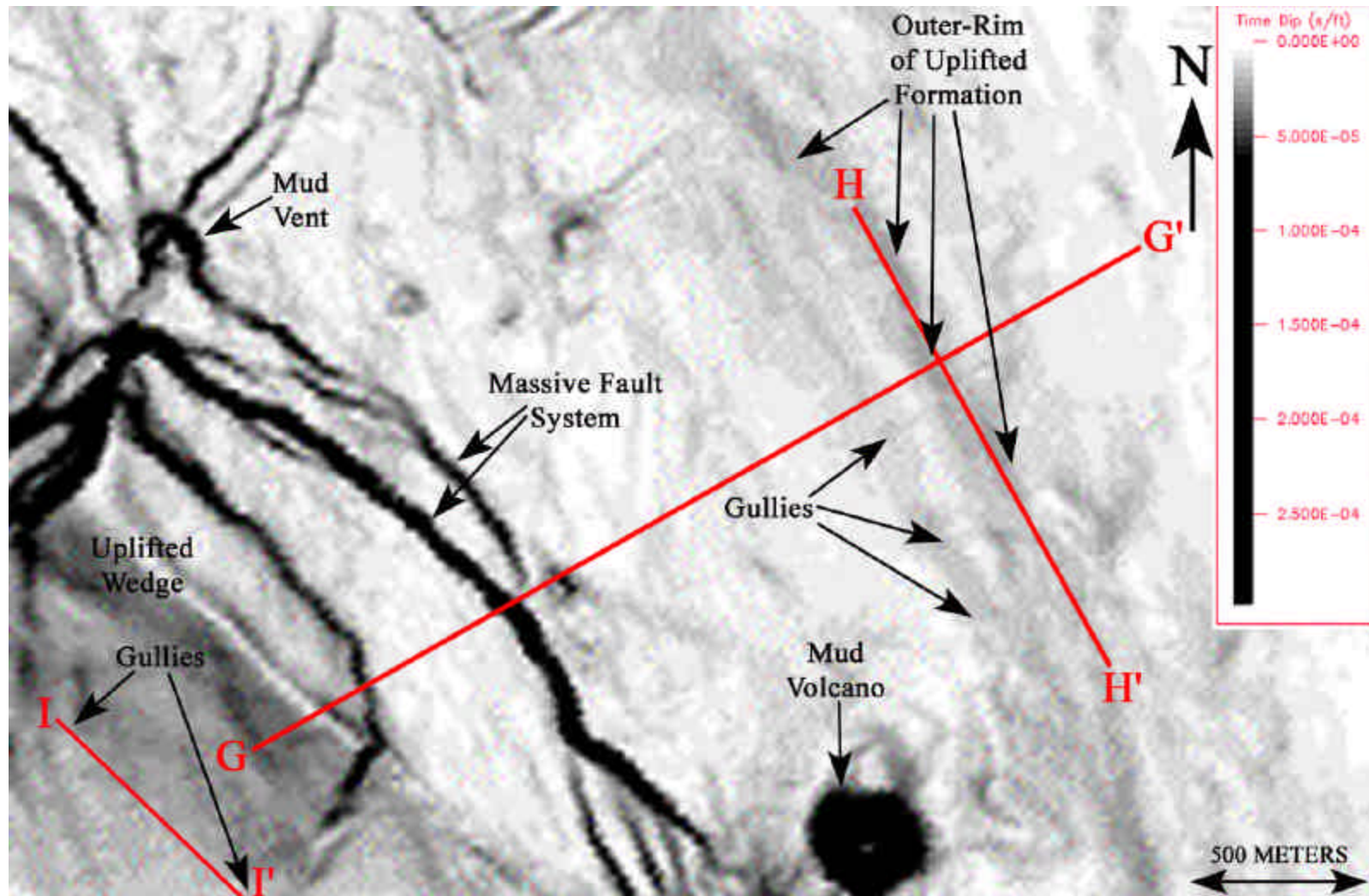


Figure 5.10 Water bottom dip map from the northern portion of the study area, illustrating the positions of three 3D arbitrary seismic profiles (in red) crossing the uplifted wedge and outer rim of the formation (G to G'), and the gullies (H to H'; I to I'). Higher dip angles appear black. Redrafted from a water bottom dip map provided by ENI Petroleum (Appendix B, Sheet 2).

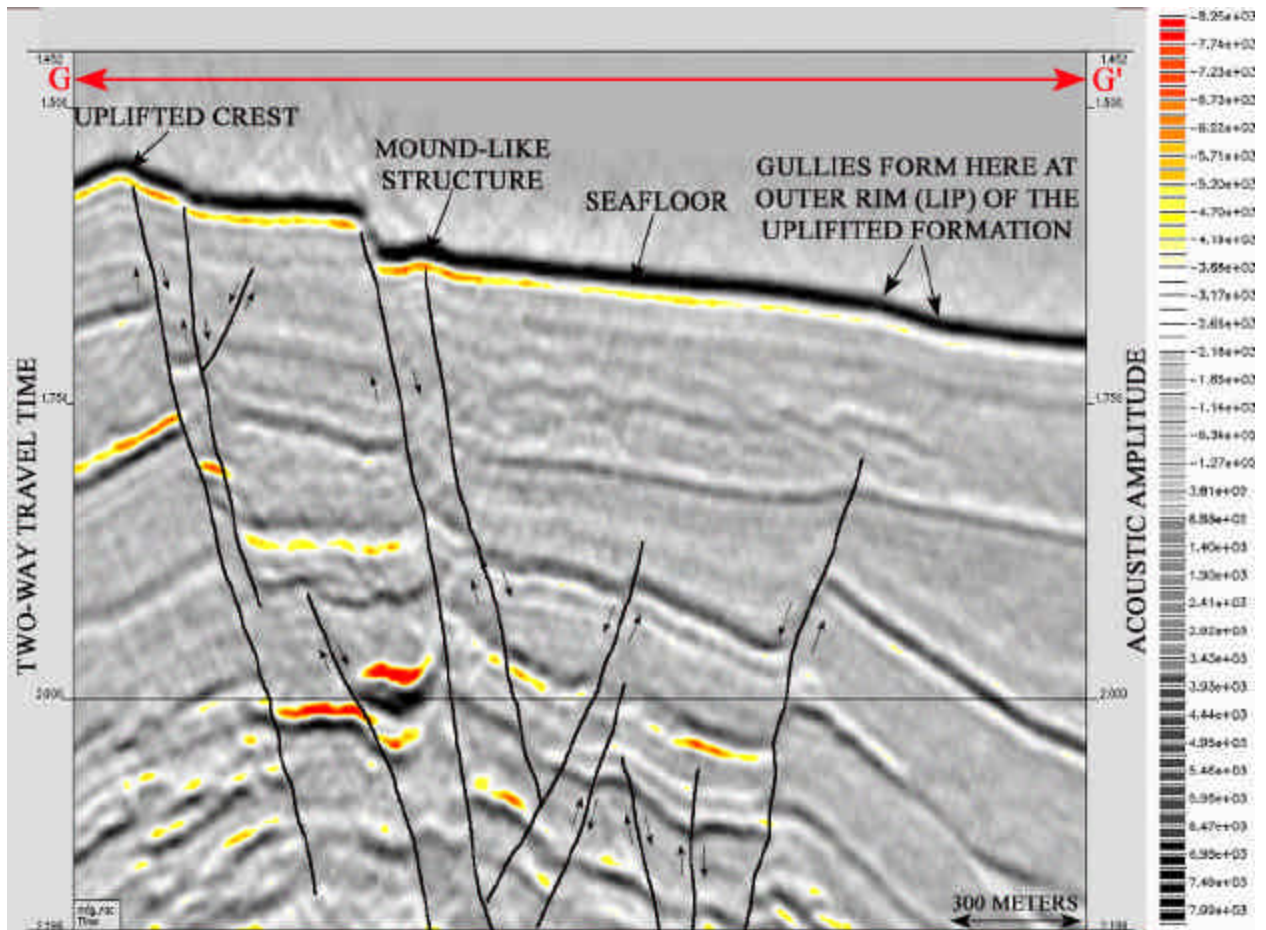


Figure 5.11 Three-dimensional seismic profile across the northern portion of the study area illustrating the bounds of the deformation due to uplift (uplifted crest to the outer rim). Note the change in slope angle at the outer rim of the deformation. See Figure 5.9 for plan view position of seismic line (G to G'). Redrafted from an image provided by ENI Petroleum.

amplitudes (yellow) occur just below the gullies on the seafloor, which may indicate the presence of biogenic gas. Deep below the seafloor, three purely vertical faults are identified. The vertical faults are caused by concentric extension due to the salt uplift in the central portion of the study area (Vendeville et al., 2003). The salt uplift creates thinning and concentric extension in overlying sediments, which trend away from the central locus of the uplift (Chapter 4, Section 4.3 Faulting). The presence of the vertical faults support the interpretation based on

the high-resolution data that suggests the gully features on the seafloor may be caused by concentric extension occurring at the rim of the uplifted formation.

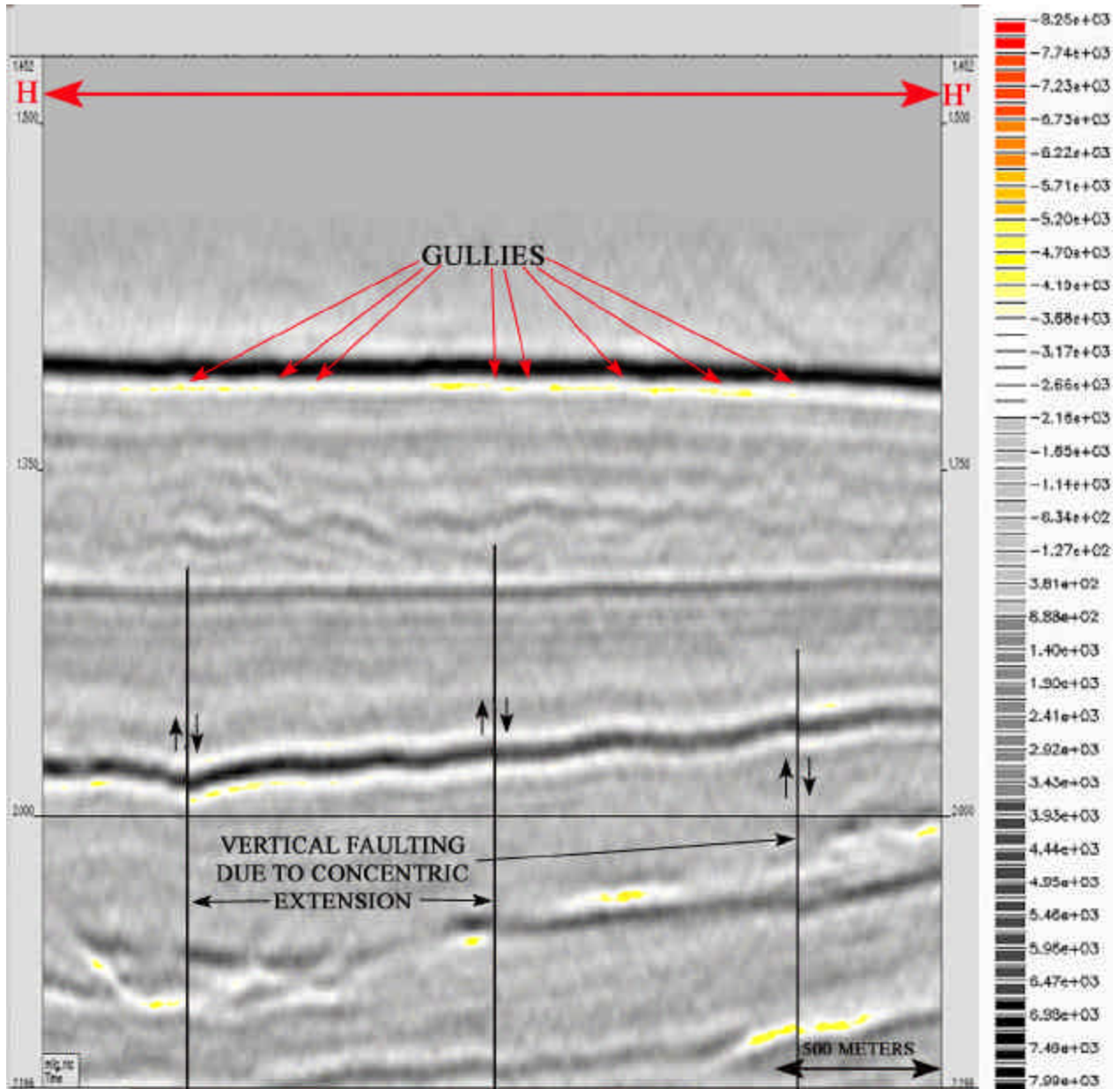


Figure 5.12 Three-dimensional seismic profile across the gullies in the northeastern portion of the study area. Note the three vertical faults occurring below gullies, which are interpreted as faulting due to concentric extension. See Figure 5.9 for plan view position of seismic line (H to H'). Redrafted from an image provided by ENI Petroleum.

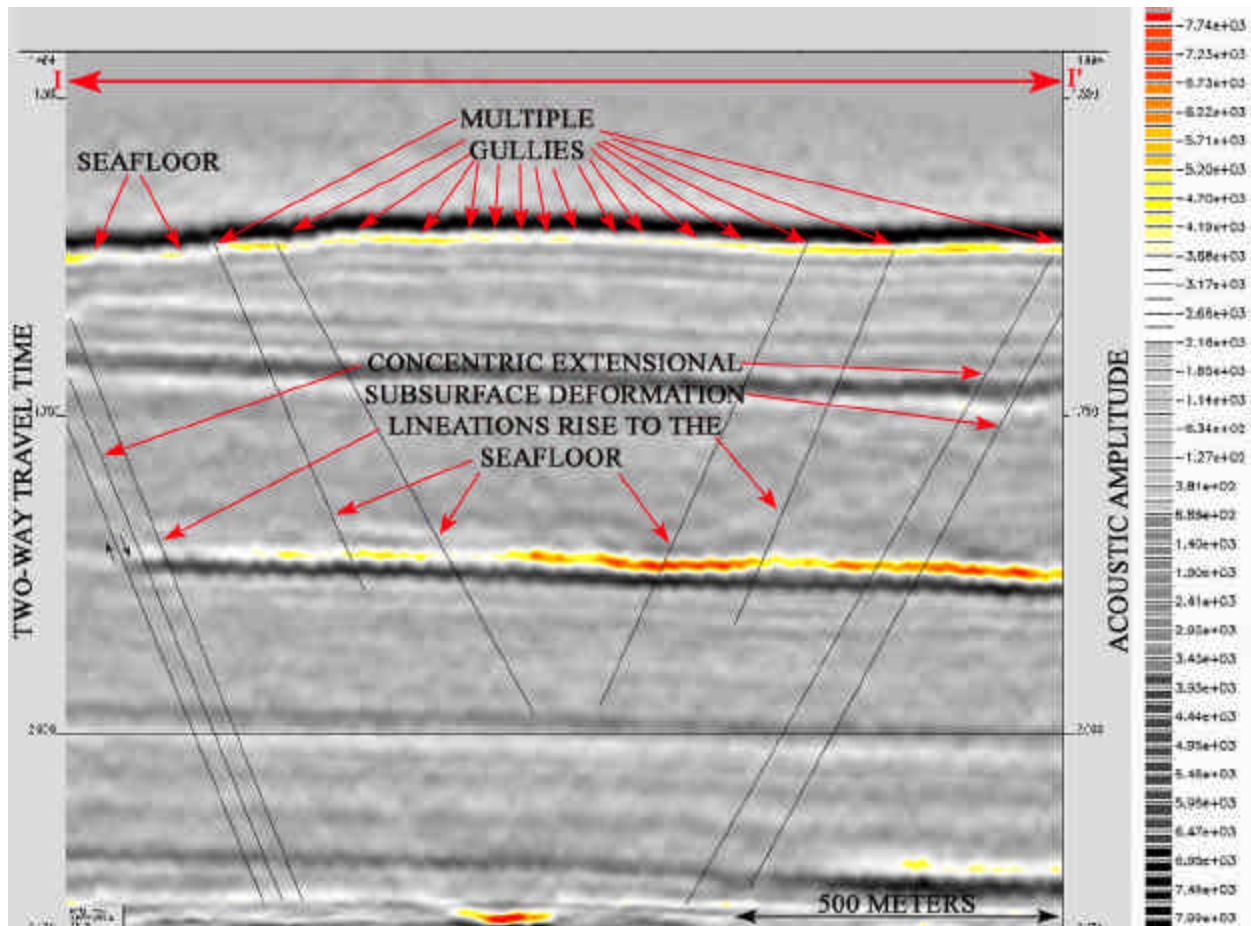


Figure 5.13 Three-dimensional seismic profile across the gullies in the northwestern portion of the study area. Note the multiple lineations, which are projected to the seafloor, interpreted as concentric extensional subsurface deformation. See Figure 5.9 for plan view position of seismic line (I to I'). Redrafted from an image provided by ENI Petroleum.

The seismic profile I to I' in Figure 5.13 transects the study area from northwest to southeast along the interpreted western outer rim of uplift, crossing multiple east to west trending gullies (Fig 5.10). At the seafloor numerous undulations in the seafloor strata mark the positions of the gullies. Higher negative amplitudes (yellow and red) occur just below some of the gullies suggesting the presence of biogenic gas. Multiple lineations appear to rise from depth to the seafloor, showing minor deformation as they cross-dense (darker) strata. The presence of these lineations also adds credence to the high-resolution interpretation that the gullies are caused by

concentric extensional forces as shown to exist in association with salt diapirs by Vendeville et al. (2003).

CHAPTER 6. GROUND-TRUTHING

6.1 Cores

Four cores were collected to provide ground-truth for the high-resolution AUV survey data (Appendix A, Sheet 4). The core locations are shown in Figures 6.1 and 6.2 and the core logs are provided in Appendix C. Core 14 was collected at the site of an interpreted mudflow southeast of a large mound-like structure. Cores 15, 16, and 17 were collected from three interpreted mound-like structures.

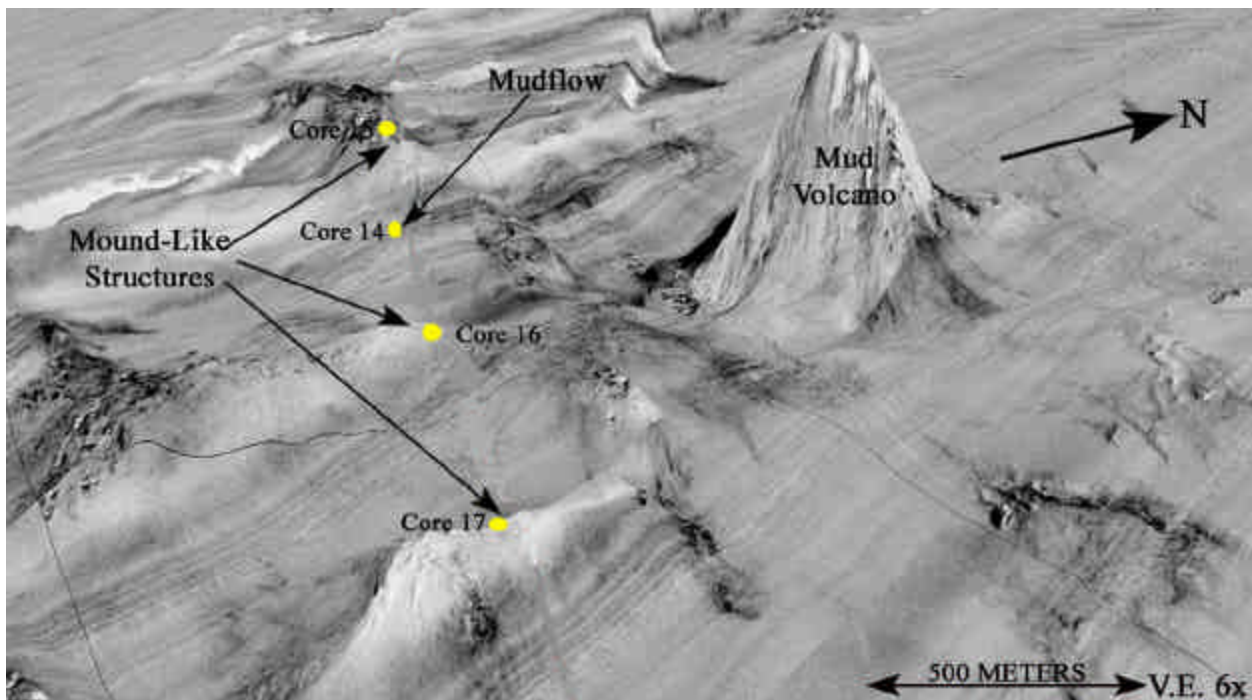


Figure 6.1 Digital terrain map of a draped side-scan sonar mosaic in the central portion of the study area illustrating the locations at which Cores 14 – 17 were collected.

Core 14 penetrated 3.7 m (12 ft) and yielded 0.6 m (2 ft) of very soft brown to olive gray clay with fine sand intermixed above 3.1 m (10 ft) of olive gray clay. The 0.6 m layer of brown to olive gray clay is interpreted as the mudflow sediments and the 3.1 m of olive gray clay is interpreted as hemipelagic drape. Cores 15, 16, and 17 penetrated between 1.4 m and 4.5 m (4.5 ft to 14.9 ft) yielding very soft greasy olive gray clay with shards and nodules of authigenic

carbonate and oil streaks. All of the cores released copious amounts of gas when they reached the surface.

The presence of greasy mud with oil and gas content and authigenic carbonate suggest that Cores 15-17 were indeed collected in mound-like structures. The presence of the 0.6 m thick brown sandy clay lying above the hemipelagic clay suggests that Core 14 penetrated through a mudflow.

6.2 ROV Investigation

A Remote Operated Vehicle (ROV) investigation was conducted over a small portion of the downthrown block in the central survey area. Dr. Harry Roberts of the Coastal Studies Institute at Louisiana State University interpreted the video from the ROV dive. The interpretation of the seafloor features cataloged 25 sites of interest. The locations of these sites are labeled A through Y and are shown in Figures 6.2 and 6.3 below and on the overview side-scan sonar mosaic map (Appendix A, Sheet 4). The interpretation, provided by Dr. Roberts, is presented in Appendix C.

The ROV investigation sites A, J, K, S, T, and U are located on interpreted hardground features. These sites exhibited a wide range of seep related features such as mounded bottom topography, local lithified highs, local zones of lithification, large rock “slabs” and boulders, nodular masses, and dark reducing sediments. A small tubeworm community is recorded at the T site living between cracks in lithified blocks. *Beggiatoa* bacterial mats are recorded at most of the seeps. Lucinid/vesycomiid clams are recorded surrounding most of the seep sites. The descriptions of the mounds, local lithified blocks (slabs) and boulders, and the types of fauna are those expected to be found at sites of seepage such as mound-like structures and mineralized seafloor areas over faults.

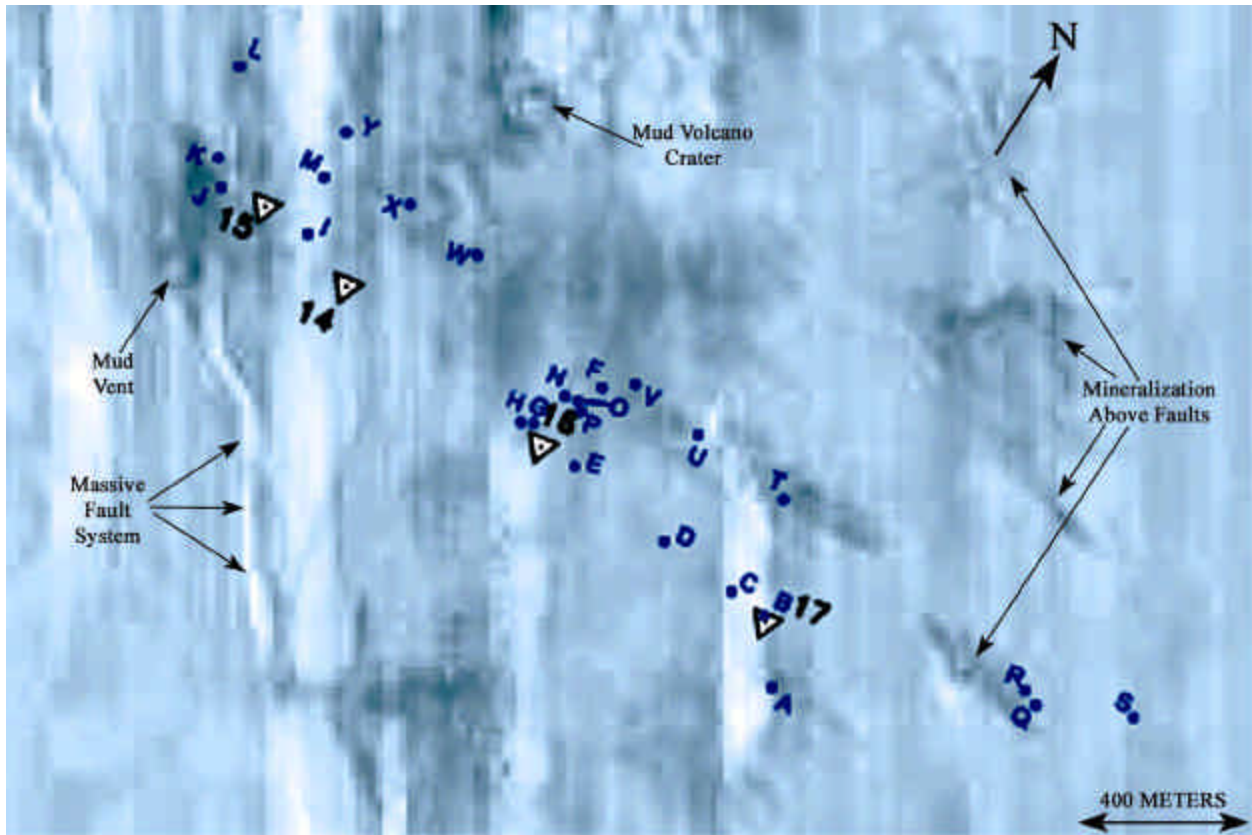


Figure 6.2 Side-scan sonar mosaic illustrating the core and ROV investigation locations in the central portion of the study area.

The ROV investigation sites B-I, L-R, and V-Y are located in areas interpreted as mudflows. These sites exhibited areas of lithified and partially lithified seafloor; small lithified nodular masses, burrowed sediments, and small pockmark features. Abundant disarticulated lucinid/vesycomiid clam shells, *Beggiatoa* bacterial mats, and non-chemosynthetic gastropods are the fauna recorded at these sites. The descriptions of the lithified and partially lithified seafloor and the presence of the abundant lucinid/vesycomiid clam shells and non-chemosynthetic gastropods suggest these investigation sites are mudflows.

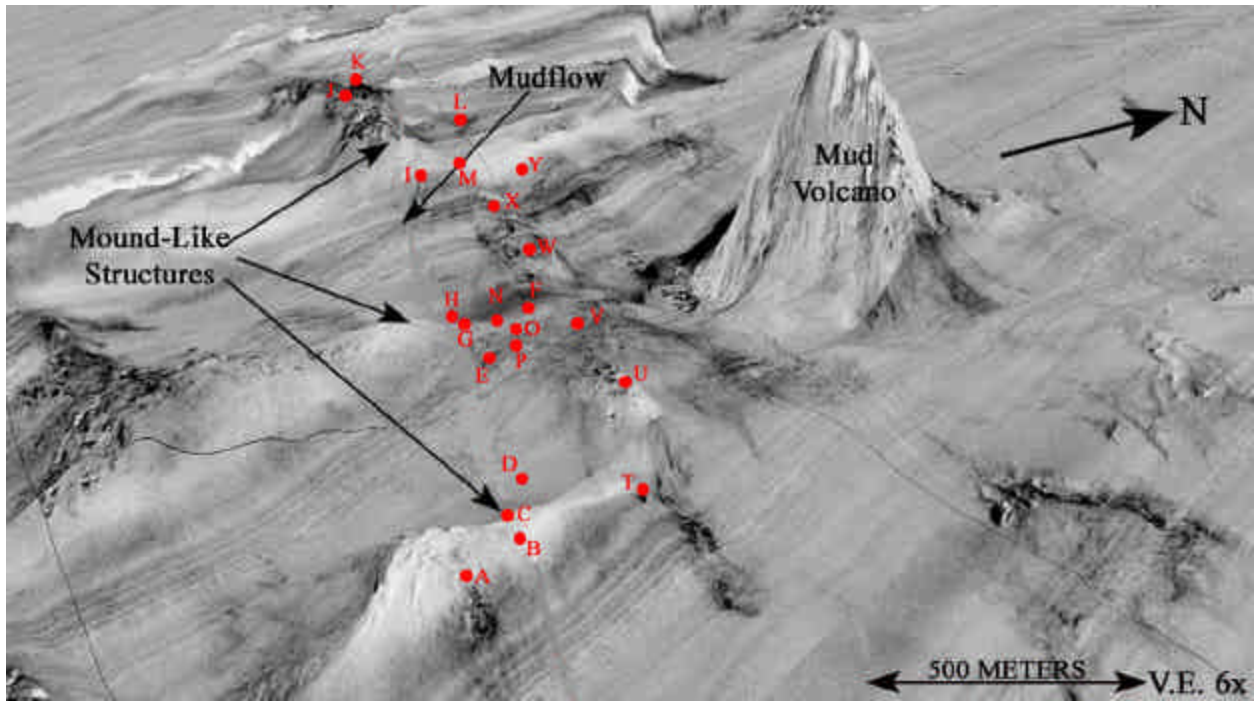


Figure 6.3 Digital terrain map of a draped side-scan sonar mosaic in the central portion of the study area illustrating the majority of the ROV investigation site locations.

CHAPTER 7. CONCLUSIONS

7.1 Overview Summary of Resolution

The high-resolution Autonomous Underwater Vehicle (AUV) data set and the standard 3D seismic data set are both capable of supplying high quality plan view maps of large areas that can be extremely valuable for geohazard interpretations. However, the resolution of the 3D seismic is limited and it cannot image the smaller features on the seafloor such as small faults, gullies, small vents, or pockmarks. A comparison of the digital terrain map side-scan sonar mosaic and the water bottom amplitude extraction indicates that the side-scan sonar shows multiple features in a varied array of backscatter for which the amplitude extraction will only show a single large colored area. The plan view bin size (foot print) of the side-scan sonar (0.5 m x 0.5 m) is much smaller than the bin size of 3D seismic (20 m x 12 m) and this allows the side-scan sonar to resolve much smaller features than 3D seismic.

Below the seafloor, a comparison of the subbottom profiles and the 3D seismic cross-sections reveals that the resolution of 3D seismic is also limited. The 3D seismic data contain acoustic impedance differences that reflect stratigraphy and the presence of bubble phase gas. However, the precise locations of extrusive sites often cannot be determined because of the coarseness of the low frequency data as compared to the AUV-acquired high frequency subbottom profiler data. The 3D seismic does not image the small faults with lesser displacement that are readily interpreted from subbottom profile records. This lack of resolution is because the profile tuning thickness (resolution) of the subbottom profiler (10 cm) is much smaller than that of the 3D seismic (14 m to 17 m).

7.2 Advantages and Disadvantages

- In several cases the water bottom amplitude map showed interpretable mudflows that the DTM side-scan sonar mosaic did not. The side-scan sonar may not image some of these mudflows because in some regions the side-scan sonar's beam is attenuated due to substantial topography such as in faulted areas. In these situations an attenuated or erroneous low gain return or acoustic shadow may corrupt the data causing a misinterpretation of the feature. Due this problem with the side-scan sonar 3D seismic may be a better tool for low resolution mapping of the bounds exhibited by seafloor features.
- The water bottom amplitude extraction and dip maps are not capable of showing smaller seafloor features such as minor faults, gullies, vents, or pockmarks, which are readily interpreted with side-scan sonar.
- The 3D seismic cross-sections can image stratigraphy below seafloor features suggesting the location and presence of gas and fluid-rich sediments that often cannot be determined with the subbottom profiler due to acoustic turbidity and limited penetration.
- The locations of smaller faults with lesser vertical displacement, that act as conduits to extrusive sites, often cannot be seen on 3D seismic cross-sections but can be on subbottom profiles.
- The 3D seismic cross-sections image far deeper below the seafloor than the subbottom profiler, which can only record the upper 75 m of sediments. This deeper penetration allows a regional assessment of the subsurface environment, which is not available with subbottom profiles.

- The high-resolution data is much better at ascertaining detailed relationships, such as the interpretation of processes that are reflected in the near seafloor geology.
- The 3D seismic can provide a long-term subsurface record of sediment stability, while the high-resolution cannot.
- Surface amplitude data from 3D seismic can distinguish hard vs. soft bottom and the presence of gas-charged sediments.
- The 3D seismic profiles show “phase reversals” at the seafloor that delineate and identify gas-charged sediments.
- The patterns exhibited by the larger faults can be better imaged by 3D seismic in most cases.

7.3 Conclusive Remarks

The comparison of high-resolution and standard 3D seismic data suggests that both techniques are useful tools in well site investigations and geohazards assessments. Both techniques have the capability to accurately define both seafloor and subsurface features.

The principal shortcoming of 3D seismic for these studies is its poor resolving capability of smaller seafloor and subsurface features. This indicates 3D seismic should primarily be utilized for well site investigation and geohazard assessments only in areas that do not have significant faulting and/or seafloor perturbations.

The principle disadvantage of high-resolution data is its inability to image deep below the seafloor. This limits the interpretation of the environment, which can lead to erroneous and potentially dangerous inferences of what may or may not occur in the deeper subsurface.

The most advantageous use of both techniques would be to use 3D seismic to identify and delineate potential problem areas and then conduct a high-resolution survey in these areas.

The most precise and in-depth understanding of the geology pertaining to well site investigation and geohazards would result.

REFERENCES

- Bone, M.R., B.F. Giles, and E.R. Tegland. 1976. 3-D high resolution data collection, processing and display: Houston, Texas, presented at 46th Annual SEG Meeting.
- Bouma, A.H. and Bryant, W.R., 1994. Physiographic features on the northern Gulf of Mexico continental slope. *Geo-Marine Letters* 14: 252-263.
- Brown, A.R., 1999. History and Ideas. In N.F. Hurley, and L.R. Lines, eds. (Fifth Edition). Interpretation of three-dimensional seismic data. AAPG Memoir 42 and SEG investigations in geophysics 9: 1-25.
- Carney, R.S. 1994. Consideration of the oasis analogy for chemosynthetic communities at Gulf of Mexico hydrocarbon vents. *Geo-Marine Letters* 14:149-159.
- Coleman, J.M., Prior, D.B., and Lindsey, J., 1983, Deltaic influences on shelf edge stability processes. In D.J. Stanley, and G.T. Moore, eds. *The Shelf Break: Critical Interface on Continental Margins*. Society of Economic Paleontologists and Mineralogists Special Publication 33, pp. 121-137.
- Coleman, J.M., Roberts, H.H., and Bryant, W.R., 1991, Late Quaternary sedimentation, in Salvador, A., *The Gulf of Mexico Basin: Boulder, Colorado*, Geological Society of America, *The Geology of North America*, v. J, pp. 325-352.
- Hamilton, P., 1990, Deep currents of the Gulf of Mexico. *Journal of Geophysical Research*, v.20, pp. 1087-1104.
- Hedberg, H.H., 1974, Relation of methane generation to under compacted shales, shale diapirs, and mud volcanoes. *American Association of Petroleum Geologists Bulletin*. 58:661-673.
- Hill, A.W., 1996. The use of exploration 3D data in geohazard assessment: where does the future lie? *Proceedings 28th Offshore Technology Conference*, Houston, Texas, OTC 7966, pp. 113-117.
- Hovland, M. and A.G. Judd. 1988. Seabed pockmarks and seepages: Impact on geology, biology and the marine environment. Graham Trotman. London. 293 pp.
- Jackson, J.A. 1997. Remote sensing, In Jackson, J.A. ed., *Glossary of Geology-Fourth Edition*: Alexandria, Virginia, American Geological Institute, pp. 541.
- Kleiner, A.A., and J.G. Northcutt. 2004. AUV sea trials and tribulations. *Hydro International* v. 8, No. 1: 7-9.
- Lee, G.H., Bryant, W.R., and Watkins, J.S., 1989. Salt structures and sedimentary basins in the Keathley Canyon area, northwestern Gulf of Mexico: their development and tectonic

implications, *in* Gulf of Mexico salt tectonics, associated processes and exploration potential: SEPM Gulf Coast Section, 10th Annual Research Conference Program and Abstracts, p. 90-93.

MacDonald, I.R., N.L. Guinasso, J.F. Reilly, J.M. Brooks, W.R. Callender, and S.G. Gabrielle, 1990. Gulf of Mexico hydrocarbon seep communities: VI. Patterns in community structure and habitat. *Geo-Marine Letters* 10:244-252.

MacDonald, I.R., N.L. Guinasso, R. Sassen, J.M. Brooks, L. Lee, and K.T. Scott, 1994. Gas hydrates that breach the sea floor on the continental slope of the Gulf of Mexico. *Geology* 22:699-702.

McBride, B.C., P. Weimer, and M.G. Rowan. 1998. The effect of allochthonous salt on the petroleum systems of northern Green Canyon and Ewing Bank (Offshore Louisiana), northern Gulf of Mexico. *American Association of Petroleum Geologists Bulletin*. 82:1083-1112.

Mann, R.G., 1987. Seismic stratigraphy and salt tectonics of the northern Green Canyon area, Gulf of Mexico: Ph.D. dissertation, Texas A&M University, College Station, Texas, 212 p.

Neurauter, T.W. and H.H. Roberts. 1994. Three generations of mud volcanoes on the Louisiana continental slope. *Geo-marine Letters* 14:120-125.

Neurauter, T.W. and H.H. Roberts. 1992. Seismic and visual observation of seepage-related structures on the continental slope, northern Gulf of Mexico. *Proceedings 24th Offshore Technology Conference*, Houston, Texas, OTC 6850, pp. 355-362.

Neurauter, T.W. and W.R. Bryant. 1990. Seismic expression of sedimentary volcanism on the continental slope, northern Gulf of Mexico. *Geo-Marine Letters* 10:255-231.

Northcutt, J.G., A.A. Kleiner, and T.S. Chance. 2000. A high-resolution survey AUV. *Proceedings 2000 Offshore Technology Conference*, Houston, Texas, OTC 12004, pp. 1-5.

Paull, C.K., J.P. Chanton, A.C. Neumann, J.A. Coston, C.S. Martens, and W. Showers. 1992. Indicators of methane-derived carbonates and chemosynthetic organic carbon deposits: Examples from the Florida Escarpment. *Palaios* 7:361-375.

Ranganathan, V. and J.S. Hanor. 1989. Perched brine plumes above salt domes and dewatering of geopressed sediments. *Journal of Hydrology* 110:63-86.

Ritger, S., B. Carson, and E. Suess. 1987. Methane-derived authigenic carbonates formed by subduction-induced pore-water expulsion along the Oregon/Washington margin. *Geological Society of America Bulletin* 98:147-156.

Roberts, H.H. 2001. Improved geohazards and benthic habitat evaluations: digital acoustic data with ground truth calibrations. OCS Study MMS 2001-050. U.S. Dept. of the Interior, Minerals Mgmt. Service, Gulf of Mexico OCS Region, New Orleans, La. 116 pp + appendices.

Roberts, H.H., 1998, Evidence of Episodic Delivery of Fluids and Gases to the Seafloor and Impacts of Delivery on Surficial Geology (Gulf of Mexico), 1998 AAPG Annual Convention Abstract, pp. 1-6.

Roberts, H.H. and P. Aharon. 1994. Hydrocarbon-derived carbonate buildups of the northern Gulf of Mexico continental slope: A review of submersible investigations. *Geo-Marine Letters* 14:135-148.

Roberts, H.H., P. Aharon, and M.M. Walsh. 1992b. Cold-seep carbonates of the Louisiana continental slope-to basin floor, pp. 95-104. In Rezak, R. and D. Lavoie, eds. *Carbonate Microfabrics*. Springer-Verlag, Berlin.

Roberts, H.H., P. Aharon, R. Carney, J. Larkin, and R. Sassen. 1990. Responses to hydrocarbon seeps, Louisiana continental slope. *Geo-Marine Letters* 10:232-243.

Roberts, S.J. and J.A. Nunn. 1995. Episodic fluid expulsion from geopressed sediments. *Marine and Petroleum Geology* 12:195-204.

Sassen, R., P.J. Post, D.A. DeFreitas, and S.T. Sweet. 2003. Geochemistry of an oil seep and gas hydrate, central Gulf of Mexico: Significance to paleogeography and possible source rocks. *Gulf Coast Association of Geological Societies/Gulf Coast Section SEPM Transactions* 53:741-754.

Sassen, R., S. Joye, S.T. Sweet, D.A. DeFreitas, A.V. Milkov, and I.R. MacDonald. 1999. Thermogenic gas hydrates and hydrocarbon gases in complex chemosynthetic communities, Gulf of Mexico continental slope. *Organic Geochemistry* 30:485-497.

Sassen, R., I.R. MacDonald, A.C. Reguejo, N.L. Guinasso, Jr., M.C. Dennicutt II, S.T. Sweet, and J.M. Brooks, 1994. Organic geochemistry of sediments from chemosynthetic communities, Gulf of Mexico slope. *Geo-Marine Letters* 14:110-119.

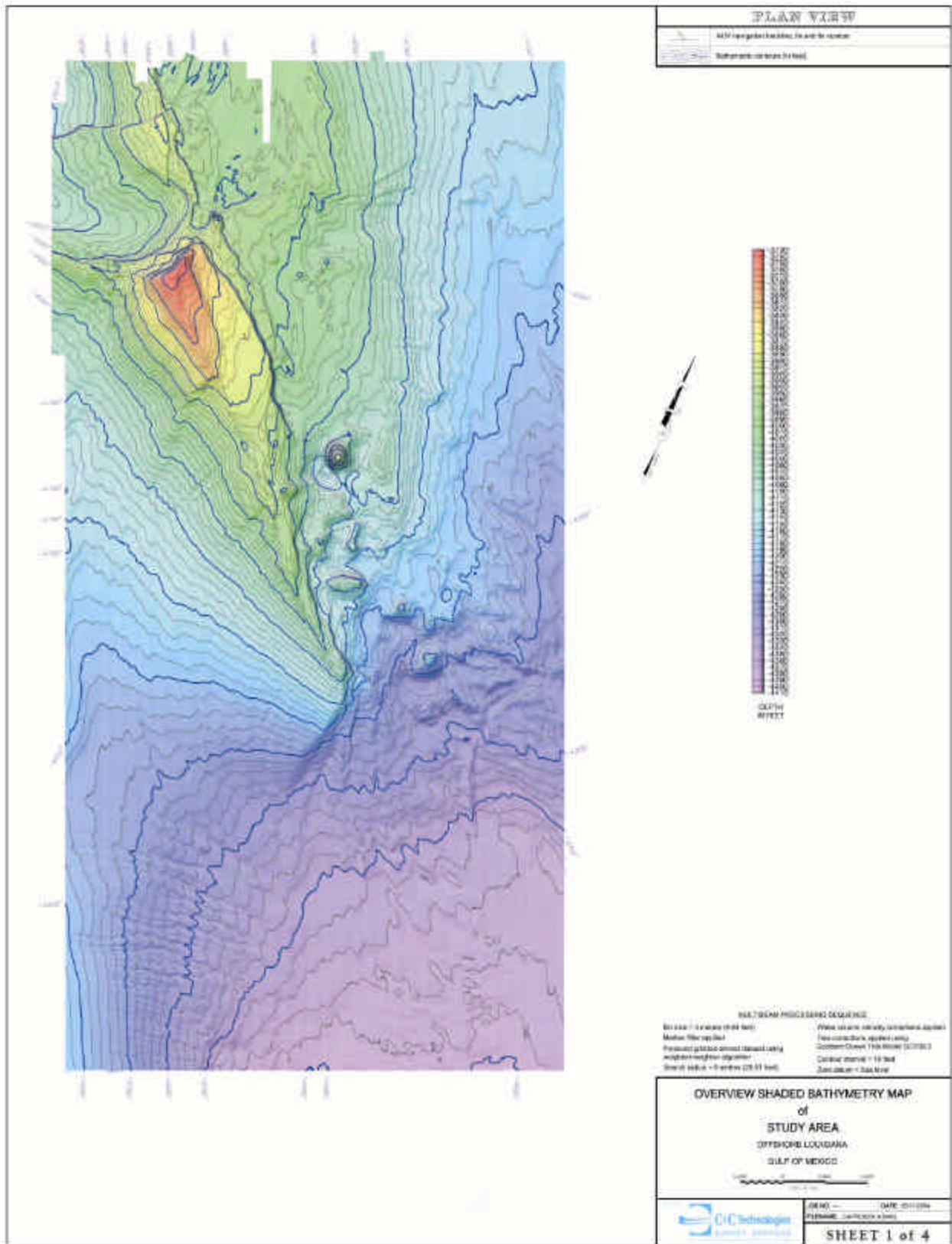
Trabant, P.K. 1984. Applied high-resolution geophysical methods. In Trabant, P.K. ed. *Offshore Geoengineering Hazards Short Course Technical Manual*. International Human Resources Development Corporation, Boston, 59 pp + appendices.

Vendeville, B.C., K. Fouad, and P.R. Knox. 2003. Radial faulting above salt-diapir overhangs: Natural example, and physical and kinematic models. *Gulf Coast Association of Geological Societies/Gulf Coast Section SEPM Transactions*. 53:824-831.

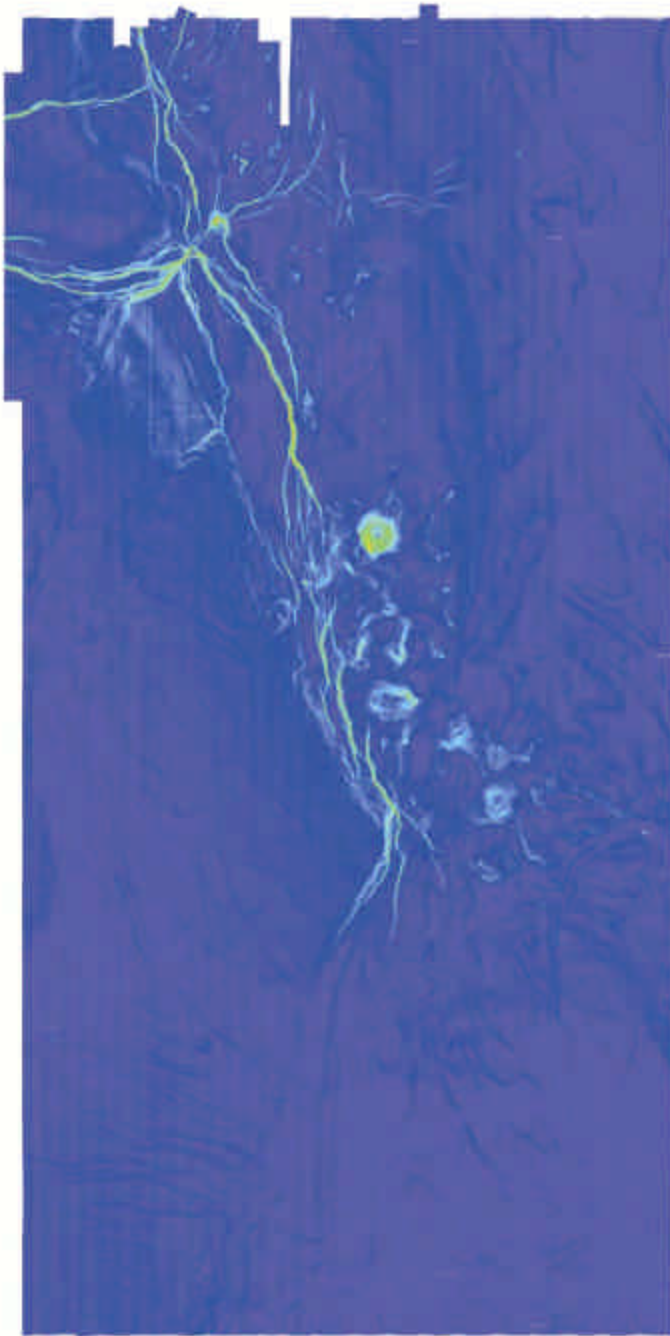
Walton, G.G., 1972. Three-dimensional seismic method. *Geophysics* 37: 417-430.

Woodbury, H.O., I.B. Murray, Jr., P.J. Pickford, and W.H. Akers. 1973. Pliocene and Pleistocene depocenters, outer continental shelf, Louisiana and Texas. *American Association of Petroleum Geologists Bulletin*. 57:2428-3439.

APPENDIX A. HIGH-RESOLUTION DATA MAPS



PLAN VIEW



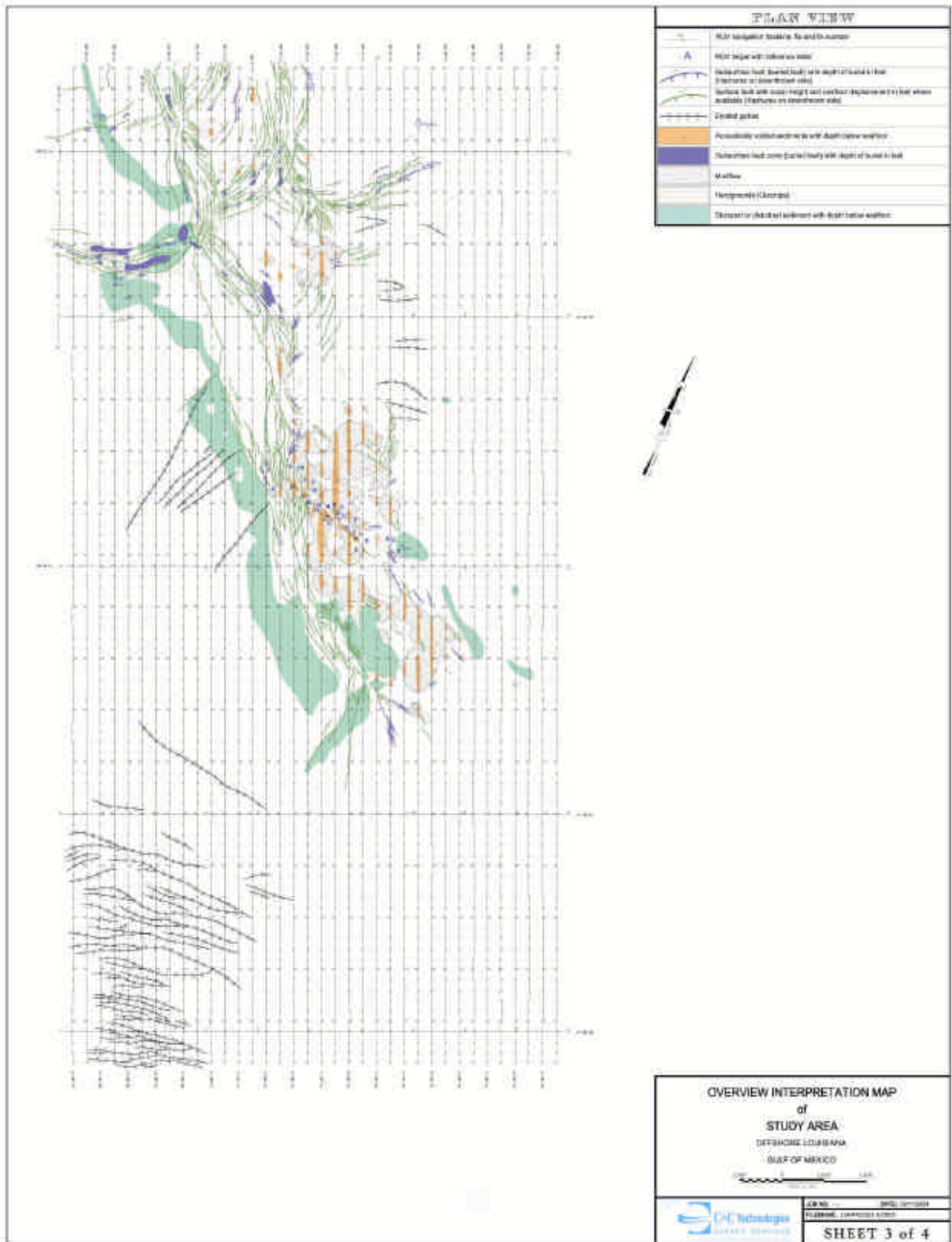
OVERVIEW GRADIENT MAP
of
STUDY AREA
OFFSHORE COLOMBIA
GULF OF MEXICO

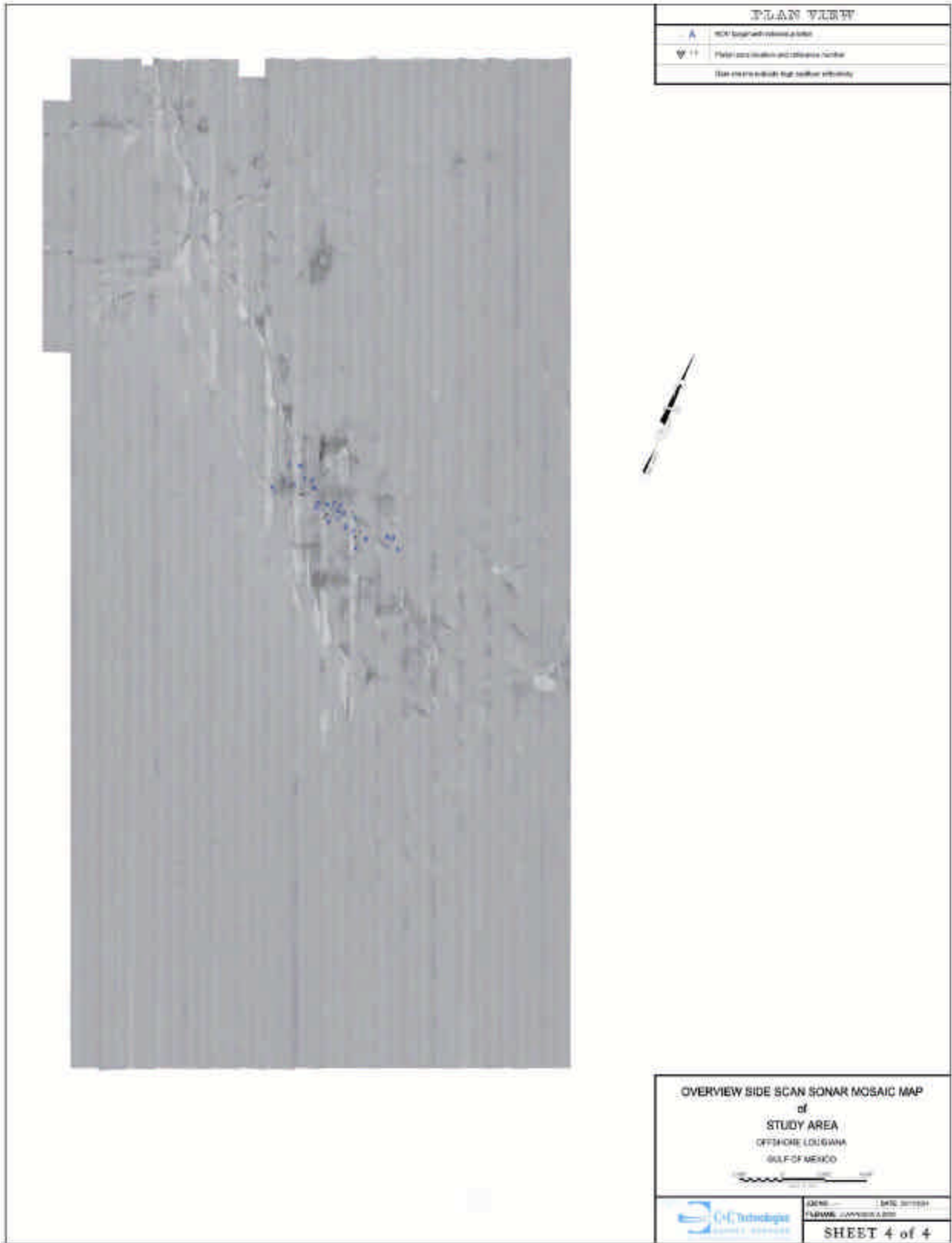


DATE: 01/20/2014

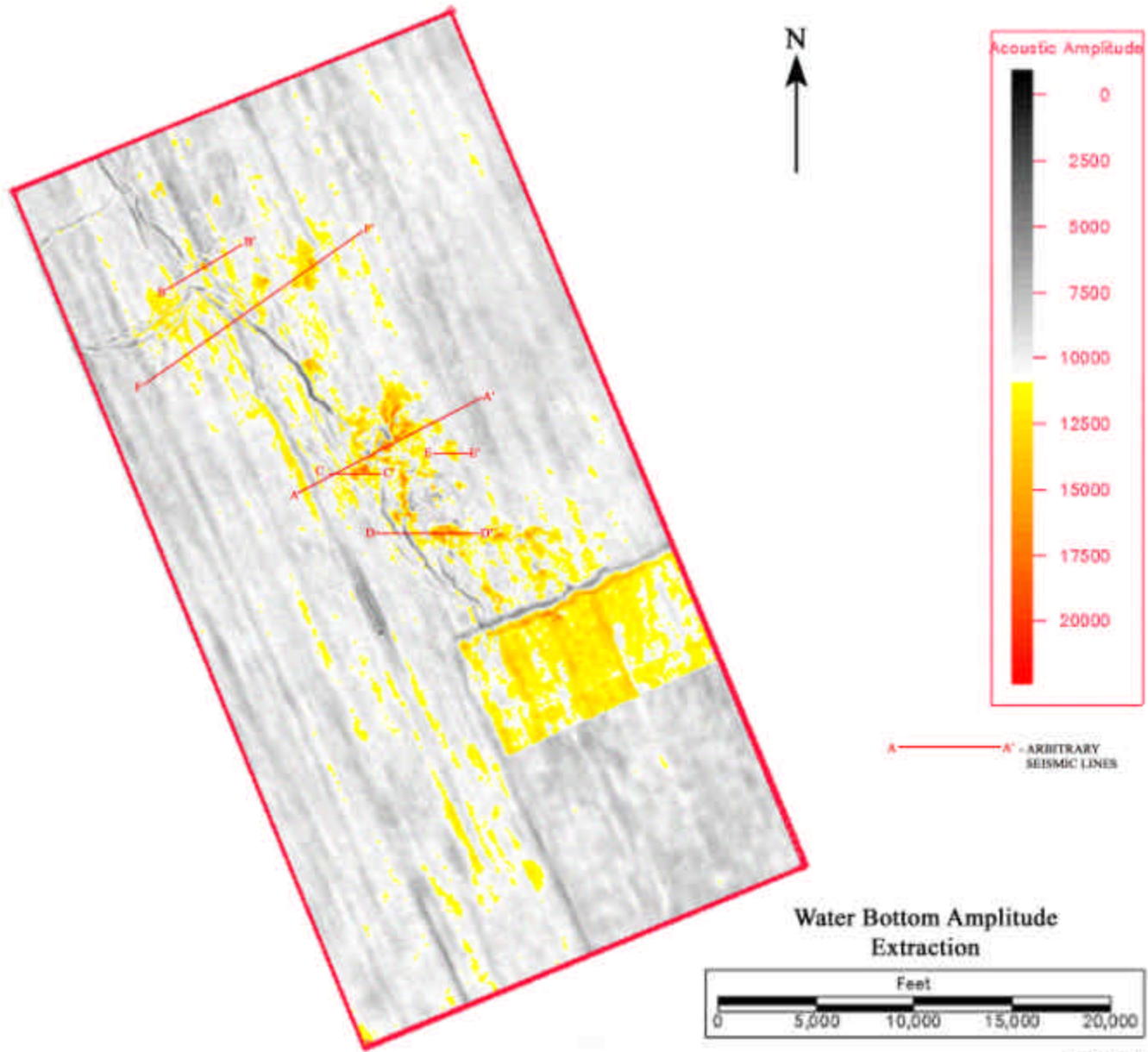
PROJECT: COLOMBIA GULF

SHEET 2 of 4

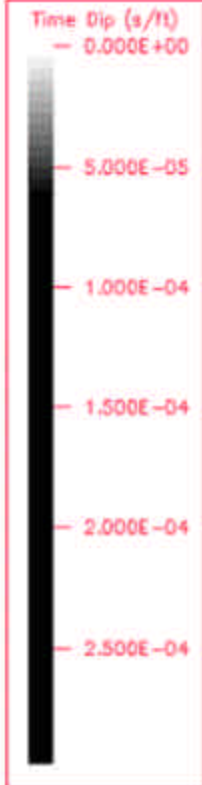
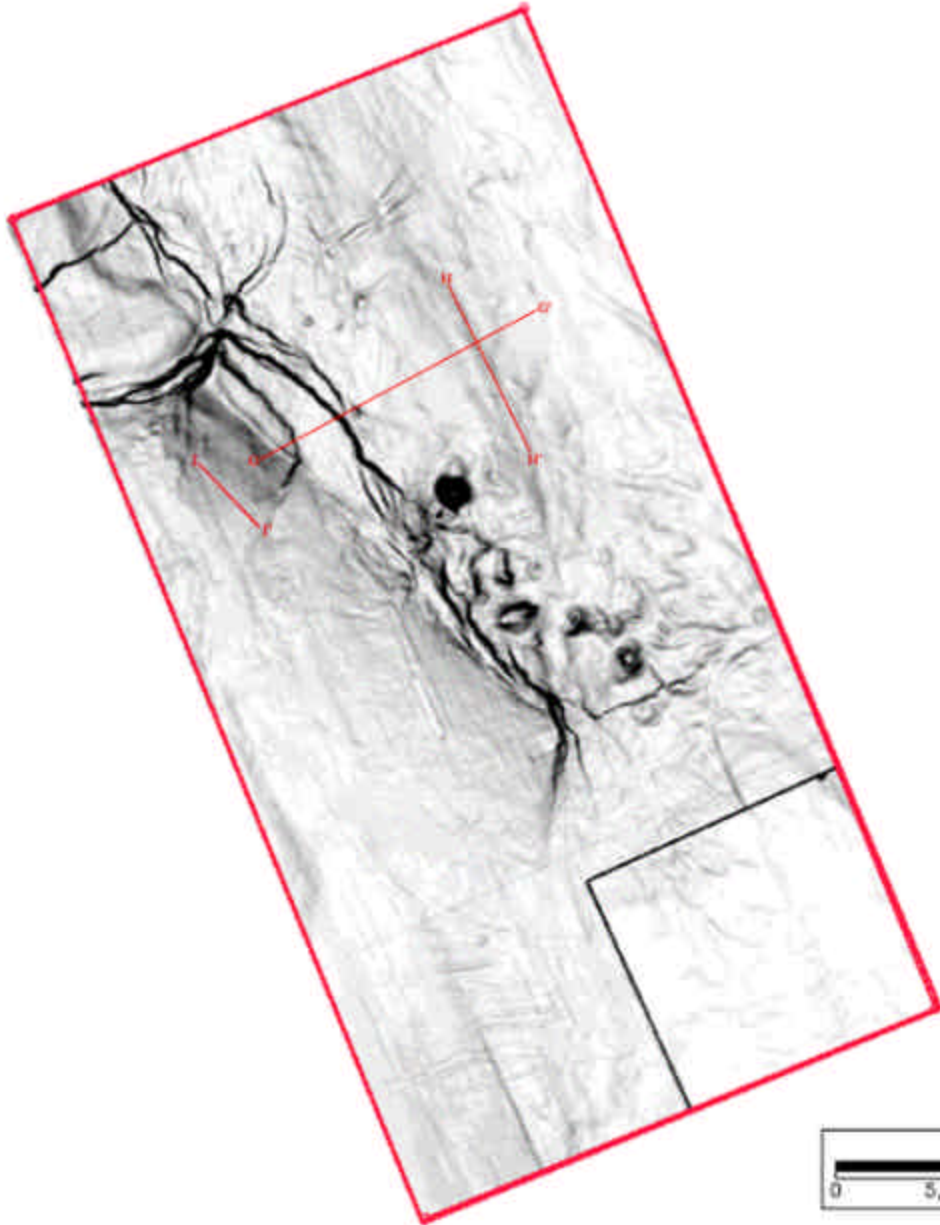




APPENDIX B. 3D SEISMIC DATA MAPS

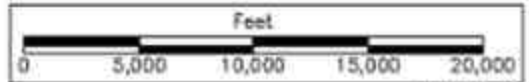


SHEET 1 OF 2



○—○ - ARBITRARY SEISMIC LINES

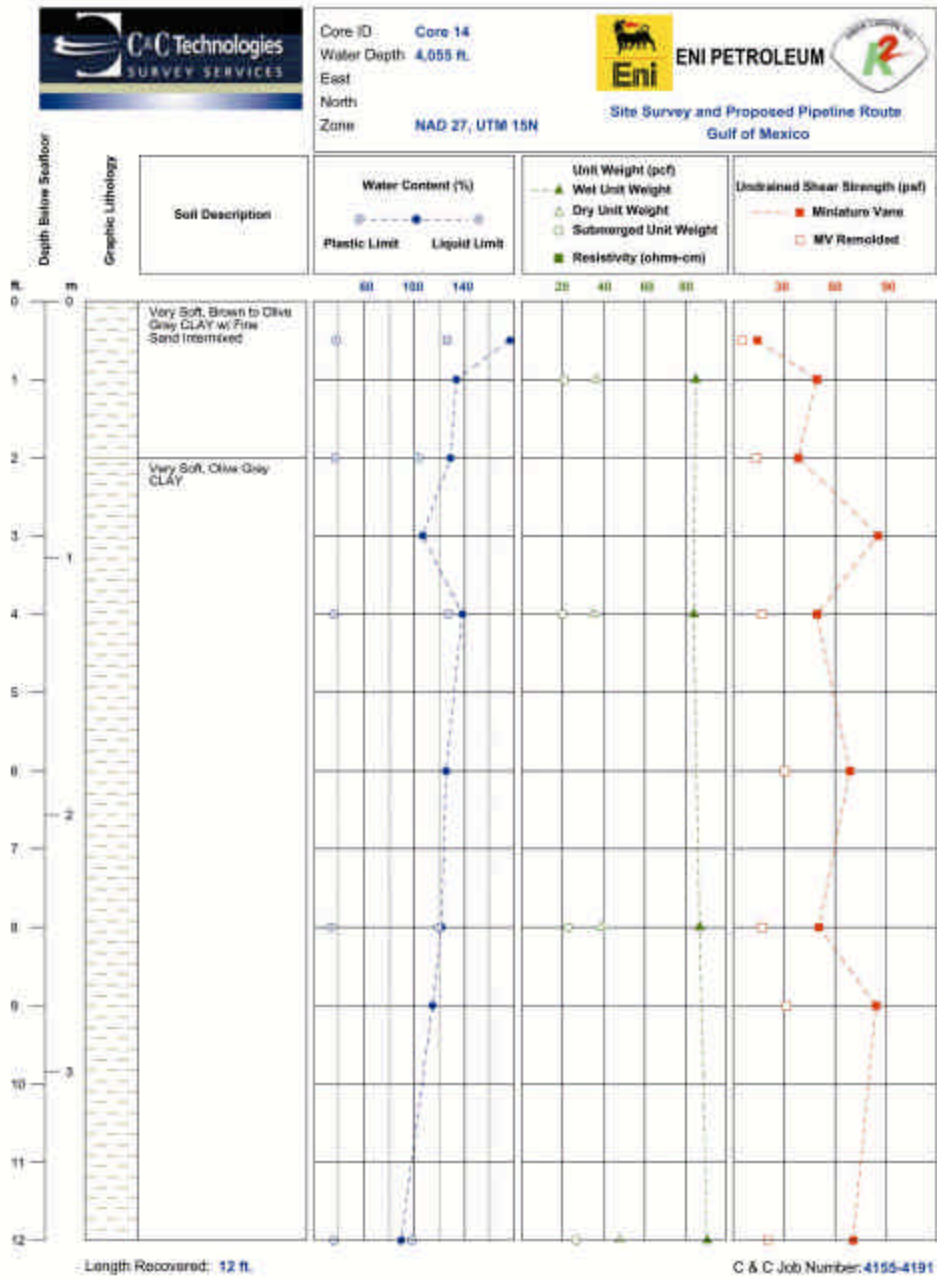
Water Bottom Dip Map



SHEET 2 OF 2

APPENDIX C. GROUND-TRUTHING DATA

Core Logs 14 - 17:



18815 SHADOW WOOD DRIVE, SUITE 100 HOUSTON, TX 77063, USA Phone: 1-713-954-2051 Fax: 1-713-485-1115



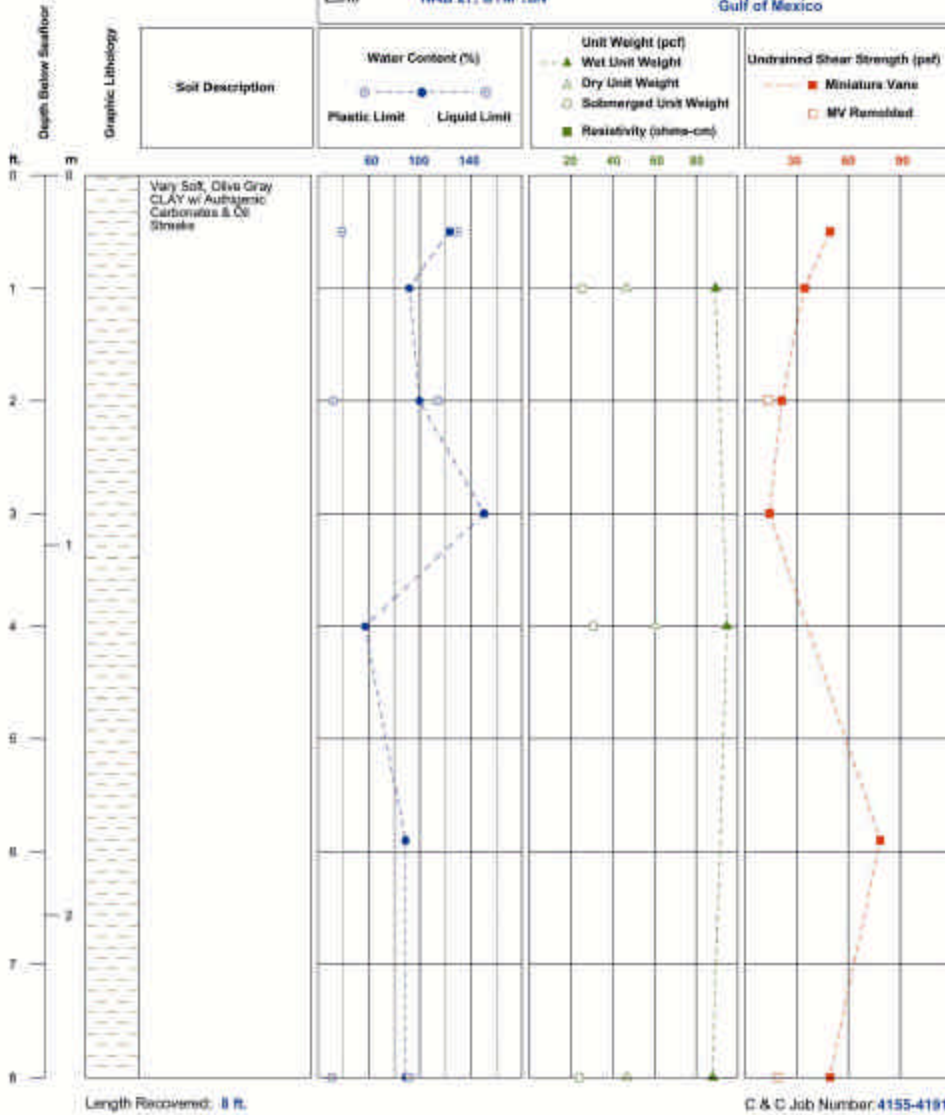
Core ID: Core 15
 Water Depth: 3,986 ft.
 East
 North
 Zone: NAD 27, UTM 15N



ENI PETROLEUM



Site Survey and Proposed Pipeline Route
 Gulf of Mexico





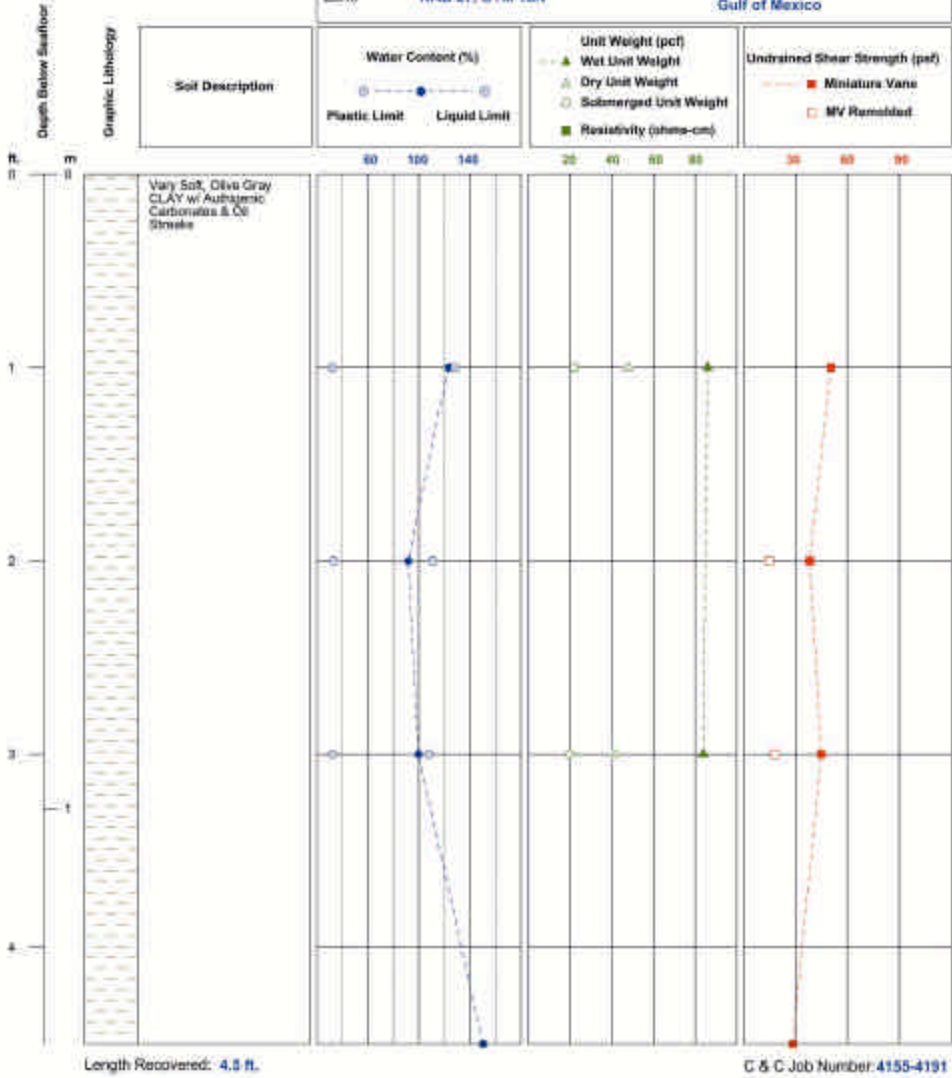
Core ID: Core 16
 Water Depth: 4,052 ft.
 East
 North
 Zone: NAD 27, UTM 15N



ENI PETROLEUM



Site Survey and Proposed Pipeline Route
 Gulf of Mexico





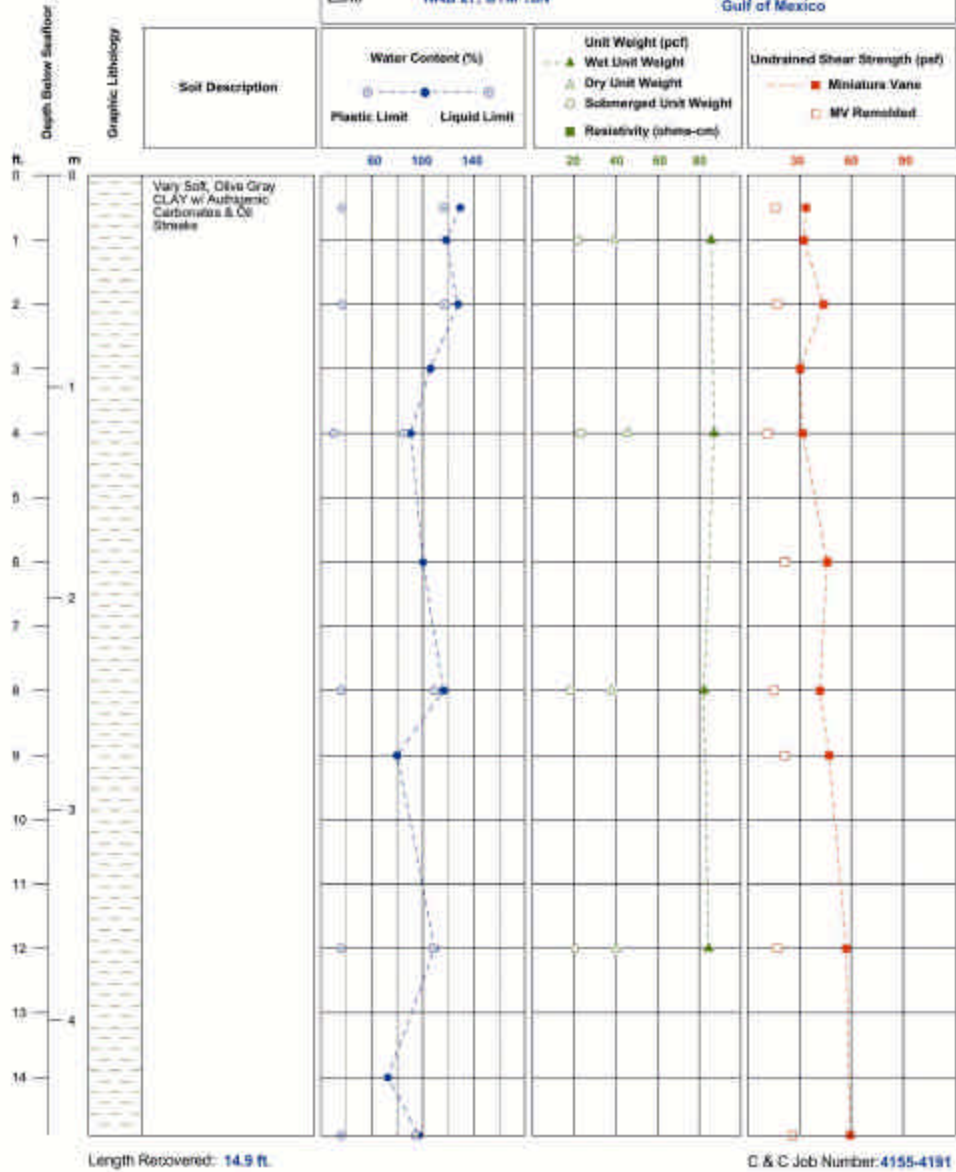
Core ID Core 17
 Water Depth 4,101 ft.
 East
 North
 Zone NAD 27, UTM 15N



ENI PETROLEUM



Site Survey and Proposed Pipeline Route
 Gulf of Mexico



ROV INVESTIGATION	
LOCATION	TARGET
A	T1 – Area showing seep-related features (scattered Lucinid-Vesycomiid clams, <i>Beggiatoa</i> bacterial mats, and local zones of lithification). Burrowed hemipelagic sediments with no seep indicators from T1 to end of tape.
B	T1 – Small area of <i>Beggiatoa</i> bacteria mats around burrows and the mouths of burrows, but no large areas of mat coverage.
C	T2 – Small area of white <i>Beggiatoa</i> bacteria mats
D	T1 – Small area of white bacterial (<i>Beggiatoa</i>) mats plus small lithified modular masses
E	T2 – Small white bacterial mats.
F	T3 – Lithified seafloor with an attached anemone. Part of a zone of lithification, but no large mound-like buildups.
G	T4 – Lithified seafloor with scattered Lucinid-Vesycomiid clams. Large rock outcrops with anemones attached. ROV tries to take a sample of rock.
H	T5 – Bacterial mats with dark, reducing sediment beneath the mats as revealed by the ROV arm.
I	T6 – Bacterial mats and small areas of seafloor lithification transition into a seabed depression with a lithified “lip” and clam shells and bacterial mats in the center as well as local seafloor lithification.
J	T7 – Mounded bottom topography with abundant Lucinid-Vesycomiid clam shells (no apparent living clam community). Large rock “slabs” and boulders with clam shells incorporated in the slabs and scattered on seabed are common with small tube worms in cracks between lithified areas. Quit a lot of relief.
K	T1 – Start of line, scattered Lucinid-Vesycomiid clams and a few small lithified nodular masses
L	T1 – From the beginning of L3 to this point only thoroughly burrowed hemipelagic sediments were encountered. There is no indication of leakage of fluids or gases up the faults crossed. However, obvious relief changes were observed. T1 starts with scattered white <i>Beggiatoa</i> bacterial mats around small burrow openings and continues with a few scattered Lucinid-Vesycomiid clams.
M	T2 – Lucinid-Vesycomiid clams increasing in number from the beginning of this zone, but still scattered at start of T1 and beyond. T2 is probably an extension of the T1 zone.
N	T3 – Lithified seafloor with attached nonchemosynthetic fauna (anemones). Small gastropods among the lithified pieces. This area of lithification was a small mound. No tube worms were observed.
O	T4 – Small area of white <i>Beggiatoa</i> mats, nonchemosynthetic gastropods, lithified seafloor, and a few scattered clam shells. This area seems to be a pockmark-type depression with a lithified lip and bacterial mats and clam shells in the central cavity. Several pockmark-like craters are passed in the video.

ROV INVESTIGATION	
LOCATION	TARGET
P	T1 – Small mound with a central depression. The lips of the crater are lithified and small rock outcrops are exposed in the crater interior on the crater walls. Small patches of white <i>Beggiatoa</i> bacterial mats are scattered over the flanks of the features. A few Lucinid-Vesycomiid clam shells are present. Small bacterial mats and scattered clam shells extend away from this feature, but in decreasing numbers.
Q	T1 – Small area of white <i>Beggiatoa</i> bacteria mats and scattered shells. Mats are primarily around burrows.
R	T2 – Small white <i>Beggiatoa</i> bacterial mats occur around burrows. Scattered Lucinid-Vesycomiid clam shells are also present. No tube worms. However, some nonchemosynthetic gastropods were present.
S	T3 – More small white bacterial mats on mounded topography. A few scattered clam shells and gastropod shells are present. Dark reducing sediment is present beneath the surface. This site may represent a possible near-surface gas hydrate area. There seems to be some lithification of surface sediments.
T	T4 – Large lithified mound with tube worms living in cracks between lithified blocks. However, these are sparse tube worm communities with no other chemosynthetic organisms visible in association with the lithified mound except a few Lucinid-Vesycomiid clam shells. The shells occur at the bottom of cracks in the mound, and at the mound base.
U	T1 – Small white bacterial mats, a few scattered clam shells, and localized seabed lithification are present at this site. Lithification occurs on local topographic highs.
V	T1 – There seems to be several crater-like features in this area, but they transition from one to the other. Macro communities of benthic organisms are not obvious. Fault scarps identified, but apparently not leaking fluids and gases. T2 – Area of white bacterial mats, localized over a nodular and perhaps partially cemented appearing seafloor. The seabed may be partially lithified with bacterial mats in the low areas and around burrows.
W	T3 – Lithified seafloor associated with local topography highs. White <i>Beggiatoa</i> bacterial mats are common as well as scattered Lucinid-Vesycomiid clam shells. A sample of rock was attempted by ROV, but not successful. Crust-like lithification apparent in this area.
X	T4 – Large area of seafloor lithification. White bacterial mats and a few clam shells are present, but no tube worms were observed. Lithification occurs on top of mounds and ridges.
Y	T5 – Area of (4059 ft. depth) covered with small white <i>Beggiatoa</i> bacterial mats and localized nodular masses of lithified seafloor.

Modified from a ROV interpretation accomplished by Dr. Harry Roberts in February 2004.

APPENDIX D. 3D SEISMIC SURVEY SPECIFICS

Ultra Surveys - Gulf of Mexico

Acquisition Parameters

Recording System	Digital 24-bit
Source Strength	100 bar-m (3-120 Hz)
Shot Interval	75.0 m per source 07.5 m alternating†
Record Length†	13 s
Offset Range*	8000 m
Nominal Fold*	63
Acquired Bin Size	12.5 x 40 m

Processing Parameters

Prestack signal processing
Targeted Radon multiple attenuation
3D DMO / stack
3D poststack trace interpolation
3D time migration
Final cell size: 12.5 x 20 m

†Atwater Valley Phase 3 and Green Canyon Phase 13 acquired with 12 second records.

*Atwater Valley Phases 5 and 6 and Green Canyon Phases 7 and 11 acquired with 8000 m offsets, resulting in a nominal fold of 40.

Visit our web site at www.westerngeco.com
or e-mail us at multifan@westerngeco.com

© 2009 Western Geophysical, an ExxonMobil Company



VITA

The author of this thesis Bruce M. Samuel lives at 333 Montrose Street, Lafayette, Louisiana (70503), with his wife Lynn, son Joshua and dog Harley. Bruce was born on August 28th 1968 in Rhodesia, Africa (now Zimbabwe), and immigrated to the United States in 1980 with his extended family. He graduated Jenkintown High School (Jenkintown, Pennsylvania), in 1986 and entered the United States Air Force shortly thereafter. After 4 years with the Air Force Bruce accepted a Federal Civil Service position with the Louisiana Air National Guard in 1990. After 2 years, he resigned his Federal Civil Service position to attend college at Louisiana State University, Baton Rouge, Louisiana. In 1998 Bruce graduated from Louisiana State University with a Bachelor of Science degree in geology. In 1999 Bruce entered the master's program at Louisiana State University in pursuit of an advanced degree in geology. Bruce is currently working as a geologist employed by C & C Technologies, Inc., a survey company in Lafayette, Louisiana. He is also an officer in the Louisiana Air National Guard stationed at Alvin Challender Field, Bellechasse, Louisiana.